SOLID STATE STUDIES:

RAMAN SPECTROSCOPY AND THE LATTICE VIBRATIONS OF $CdCl_2$ AND $CdBr_2$

A thesis presented for the
degree of Doctor of Philosophy in Physics
in the University of Canterbury,
Christchurch, New Zealand.

by

D.J. Lockwood

1969

To My Parents,

God Bless Them.

A B S T R A C T

The fundamental lattice vibrations of the trigonal $CdCl_2$ structure (D_{3d}^5) have been analyzed group theoretically, and symmetry coordinates have been constructed. The primitive cell has nine normal modes of vibration. All six optical modes are either infrared or Raman active, so a complete vibrational analysis is possible. Results of far-infrared measurements on a Fourier-transform spectrometer together with Raman spectra recorded by argon laser excitation are presented for both $CdCl_2$ and $CdBr_2$. Symmetry assignments of the observed frequencies are made on the basis of the shift in frequency in going from chloride to bromide and the polarization behaviour. Peaks in the second-order axial infrared absorption spectra are assigned to allowed fundamental combinations. The lattice frequencies of $CdCl_2$ are consistent with those of the isomorphic crystals of $CoCl_2$ and $MnCl_2$, which have also been investigated by infrared absorption. An unsuccessful attempt was made to measure the electronic Raman spectra of Fe^{2+} and Co^{2+} ions in $CdCl_2$ and $CdBr_2$.

The Raman spectra were measured on a Raman system comprising a 5 watt argon laser and a double monochromator, with photoelectric detection. The construction of the Raman spectrometer, and the associated signal processing electronics, is described in detail. Special emphasis has been placed on the use of on-line computer techniques in processing the Raman signal. A signal averaging system has been developed that is superior to both photon counting and lock-in amplification when measuring very weak signals.

PREFACE

This thesis is the result of an interest in Raman spectroscopy that began during my M.Sc. year, when it became apparent to me that the use of laser light sources was about to revolutionise this difficult form of spectroscopy. The major part of the thesis is concerned with the development of a Raman spectrometer suitable for solid state studies. The spectrometer is described in detail, with emphasis on the application of on-line computer techniques. The remainder of the thesis is devoted to a study of the lattice vibrations of crystals with the cadmium chloride structure using Raman and infrared spectroscopy.

The development of the Raman spectroscopy facility has involved at some time or another all the Departmental workshop facilities and technical staff, and most of the academic staff. I am particularly grateful to my supervisor, Professor A.G. McLellan, for his continued help and support in encouraging this project, and to Professor B.G. Wybourne for his interest and financial support through the U.S. Air Force Grant. I wish to acknowledge useful discussions with Dr G.D. Jones and Dr R.G.T. Bennett, and I thank R.W. Tyree for his considerable help in setting up the argon laser and

double monochromator. Thanks are due to A.W. Black and I. Norrish for constructing computer electronics, to R. Ritchie for growing the crystals, to L.E. Hunter for the photographic services, and to J.H. Christie for assistance with the IBM 360/44 computing.

This research was supported by an equipment grant from the N.Z. University Grants Committee under URG Grant No. 66-241 and, in part, by the U.S. Air Force Office of Scientific Research under AFOSR Grant No. 1275-67.

Some results reported herein were first presented at the International Conference on Light Scattering Spectra of Solids, New York University, New York, 3 - 6 September 1968 and at the Annual Meeting of the Optical Society of America, Pittsburgh, 9 - 11 October 1968.

David J. Lockwood

July 21st, 1969.

CONTENTS

P A R T I

RAMAN SPECTROSCOPY

C H A P T E R 1

THE RAMAN EFFECT

1.1 Introduction

The measurement of the Raman spectrum of a crystal is one of the main methods for obtaining information about its lattice frequencies. Raman spectra, in conjunction with the complementary infrared spectra, usually give sufficient information for the phonon dispersion curves to be plotted. Neutron scattering is now taking over this role for crystals of simple structure.

Besides this, however, Raman scattering is used for testing theories of lattice dynamics. Some of the more subtle effects in Raman scattering have only been explained in more recent years due to the increase in knowledge of the properties of lattice vibrations. Theory at present is limited to the simpler crystal structures, where interpretation of spectra in terms of the theory of lattice dynamics is much easier. Thus much experimental evidence, such as the polarization effects in second-order Raman spectra, has yet to be explained.

In the lattice Raman effect, monochromatic light incident on a crystal interacts with the crystal to create or destroy lattice vibration quanta (phonons). The energy gained or lost is compensated by a change in energy of the emitted light. Thus if ω_o is the frequency of the incident light, ω_s the frequency of the scattered light, and $\hbar\omega$ the energy change involved then $\omega_s = \omega_o \pm \omega$.

The Raman effect in crystals is not limited to lattice interactions. The advent of laser light sources has enabled the observation of Raman scattering by crystal excitations such as localised impurity modes, plasmons, magnons, polaritons, polarons, electron spin-flip and Landau levels, and by electronic transitions of ions in crystals.[1] Thus Raman scattering experiments are an important tool in the study of the fundamental properties of crystals. The observations serve a two-fold purpose. Firstly to obtain information on the energy and spatial properties of crystal excitations which will help in understanding their behaviour; and secondly to improve the basic theory of Raman scattering by discovering the mechanisms involved in the scattering process.

In this thesis we are mainly concerned with developing a sophisticated Raman spectrometer which is capable of investigating the crystal properties mentioned above. Part I reviews the pertinent Raman theory and describes the Raman spectrometer. In part II, the lattice vibrations of $CdCl_2$ and $CdBr_2$ are investigated by means of Raman and infrared spectroscopy.

1.2 General Raman Theory

In 1928 Sir C.V. Raman[2] announced the discovery of an effect that bears his name, and was to win him the Nobel Prize in Physics. During the course of a systematic investigation of the scattering of light in liquids and solids he had observed frequency shifts in the scattered light which were dependent on the sample used. Shortly afterwards, Landsberg and Mandelstam[3] published details of the Raman effect in quartz.

Raman's discovery had been theoretically predicted in 1923 by Smekal.[4] Kramers and Heisenberg[5] developed the old-style quantum theory of Smekal and derived a quantum theoretical scattering formula by means of the correspondence principle. They found

that the total intensity* of the frequency-shifted scattered radiation is given by

$$I_{mn} = \frac{64\pi^4}{3c^3} (\nu_o + \nu_{mn})^4 |P_{mn}|^2, \qquad (1.1)$$

where

$$P_{mn} = \frac{1}{h} \sum_r \left[\frac{M_{rn}(\underline{E}M_{mr})}{\nu_{rm}-\nu_o} + \frac{(\underline{E}M_{rn})M_{mr}}{\nu_{rn}+\nu_o} \right]. \qquad (1.2)$$

P_{mn} is the induced electric moment matrix element or induced transition moment associated with a transition between the initial state m and the final state n of the system; c is the velocity of light; ν_o is the frequency of the incident light with electric vector $\underline{E} \exp(-2\pi i \nu_o t)$; and h is Planck's constant. The scattered light has frequency $\nu_o+\nu_{mn}$ where $\nu_{mn} = \nu_m - \nu_n$, ν_{rn} and ν_{rm} are the frequencies corresponding to the differences between states denoted by the subscripts, and M_{rn} and M_{mr} are the corresponding transition moments. For Raman scattering, $\nu_o+\nu_{mn} > 0$, which means that the energy of the incident light must be greater than the actual transition energy. The transition moments are given by

---

*This discussion is limited to spontaneous Raman scattering.

$$M_{rn} = \int \psi_n^* M \psi_r \, d\tau, \qquad (1.3a)$$

where M is the electric moment operator and ψ_n, ψ_r are the time-independent wave functions of the states n, r. Equation (1.3a) may be written as

$$M_{rn} = \langle n | M | r \rangle \qquad (1.3b)$$

in Dirac's notation.[6]

The summation in equation (1.2) is taken over all stationary states r of the system. In general these will be vibronic states, a combination of electronic states and their associated vibrational levels.

In deriving this formula it is assumed that the wavelength of the incident light is large compared with atomic dimensions, which is true for the visible region of the spectrum, and that ν_o does not coincide with a resonance frequency of the system. Infinities in equation (1.2) in the neighbourhood of resonance can be avoided by including radiative damping effects.[7] The resonance case will not be discussed here.

The Kramers-Heisenberg dispersion formula (1.1) has also been derived by Dirac[8] using his quantum theory of radiation. Both of these theories are reviewed by

Placzek.[9] Equation (1.1) has not been superseded by modern theory, and forms the basis for all Raman scattering theory.

There is a tensor relation between the complex amplitude E of the incident radiation and the induced moment. If ρ and σ denote the cartesian occrdinates x,y,z then

$$(P_\rho)_{mn} = \sum_\sigma (\alpha_{\rho\sigma})_{mn} E_\sigma, \tag{1.4}$$

where

$$(\alpha_{\rho\sigma})_{mn} = \frac{1}{h} \sum_r \left[\frac{(M_\rho)_{rn}(M_\sigma)_{mr}}{\nu_{rm}-\nu_o} + \frac{(M_\sigma)_{rn}(M_\rho)_{mr}}{\nu_{rn}+\nu_o} \right]$$

$$= \langle n | \alpha_{\rho\sigma} | m \rangle . \tag{1.5}$$

$(\alpha_{\rho\sigma})_{mn}$ represents a complex and unsymmetric tensor. Using equations (1.1) and (1.4) we have

$$I_{mn} = \frac{2^7 \pi^5}{3c^4} (\nu_o+\nu_{mn})^4 I_o \sum_{\rho,\sigma} |(\alpha_{\rho\sigma})_{mn} e_\sigma|^2 \tag{1.6}$$

for the total intensity of the scattered light per unit time, where $I_o = \frac{c}{2\pi} |E|^2$ is the intensity of the incident light and e_σ is a unit vector describing the polarization of the incident light.

In the scattering equation the energy of the final state E_n may be larger or smaller than that of the initial state E_m. If $E_n > E_m$ then the scattered

light is of lower frequency than the incident light, and the process is called Stokes scattering. The second case gives rise to anti-Stokes scattering. If $E_n = E_m$ then the scattered light is not shifted in frequency. This is Rayleigh scattering, which is coherent with the incident radiation. All these processes are depicted in the energy level scheme of Fig. 1.1. The virtual transitions to states α, β in Fig. 1.1 are described in the scattering formula by the sum over all possible stationary states r of the system. This summation arises as a consequence of the mathematical treatment of the perturbation problem, in which a wave function of the perturbed system is expanded in terms of the complete set of unperturbed wave functions.

As ν_o is not equal to an absorption frequency of the system, no actual transition to any intermediate state r takes place. There is no restriction on states r, which may lie above, below or between the initial and final states. For example, states k, l, o and p in Fig. 1.1 must all be considered in calculating the scattering matrix element for mn transitions. Even though all intermediate states are considered, they may not all contribute to the scattering intensity. According to equation (1.5) the intensity and polarization of the scattered light are determined by the transition frequencies ν_{rn} and ν_{rm} and the transition

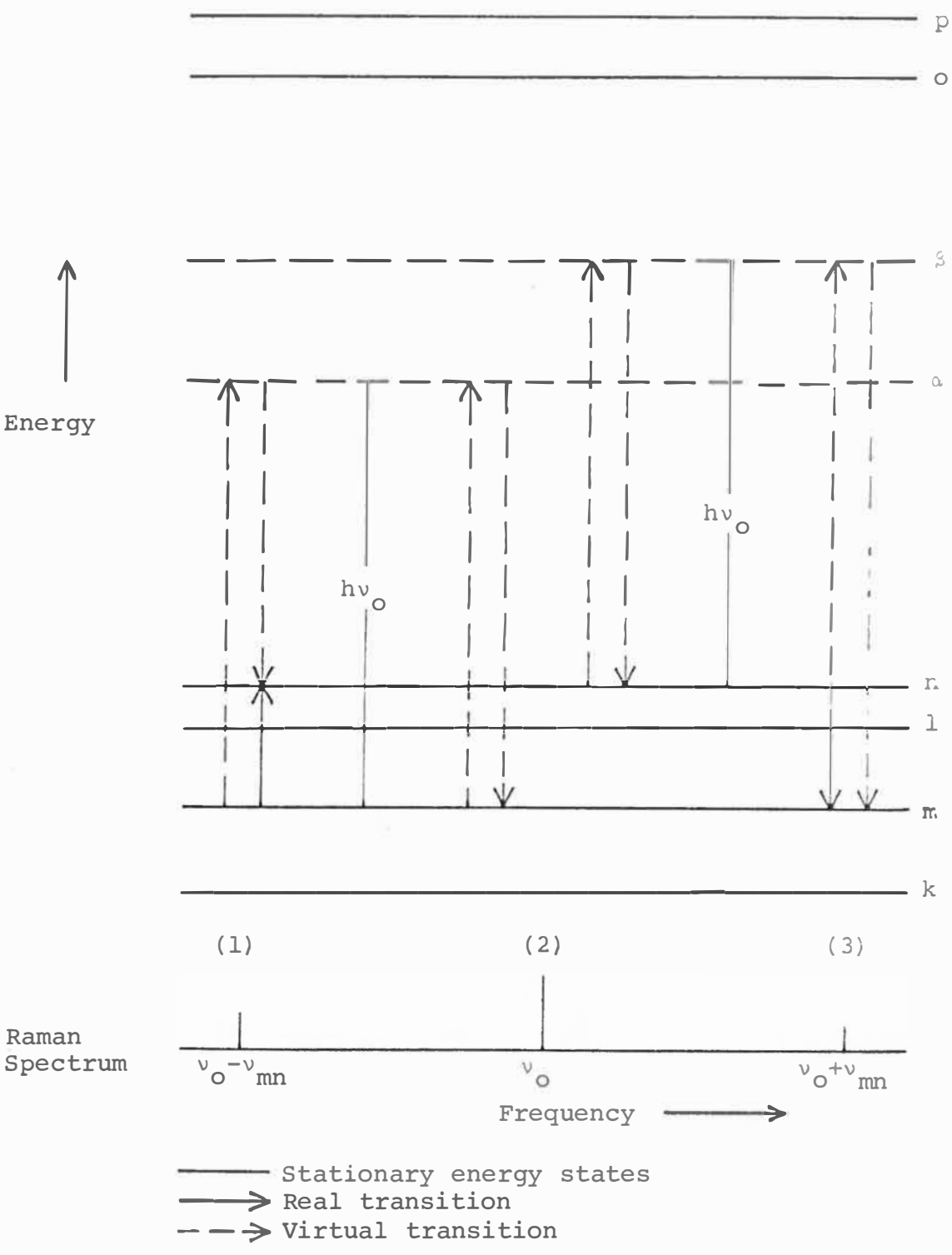

Fig. 1.1. Quantum mechanical energy level representation of (1) Raman Stokes, (2) Rayleigh and (3) Raman anti-Stokes scattering.

moments M_{rn} and M_{mr}. Products of transition moments are involved, and since these may be positive or negative it is possible for interference of the transition probabilities to take place. Thus terms that belong to different intermediate states can reinforce, weaken or cancel each other. If complete cancellation is obtained then the Raman transition is forbidden. Also, M_{rn} and M_{mr} must both be different from zero for state r to contribute.

The frequency dependence of the scattering intensity can be considered under three characteristic cases. (1) The incident frequency ν_o is small compared with the transition frequencies ν_{rn} and ν_{rm}. If the frequency dependence in the denominator of equation (1.5) is neglected, the intensity is proportional to $(\nu_o+\nu_{mn})^4$. (2) The incident frequency is close to an absorption band ν_{rm}, so that the effect of a single term in equation (1.5) predominates. Here the scattering intensity is proportional to $(\nu_o+\nu_{mn})^4/(\nu_{rm}-\nu_o)^2$. Resonance also occurs when ν_o is close to an emission frequency ν_{nr} of the final state. At the resonance frequency itself, the scattering becomes infinite according to equation (1.5). But, as mentioned earlier, damping effects have been

neglected in the derivation of equation (1.5) and so this expression no longer holds. It has been established experimentally that the scattering intensity does reach a maximum in the vicinity of an absorption band.[10] (3) The incident frequency is large compared with ν_{rm} and ν_{rn}. In this case the intensity of the Raman scattering approaches zero.[9]

1.3 Selection Rules

Selection rules in the Raman effect can be derived from symmetry considerations. Thus the transformation properties of the scattering equation need to be investigated. The scattering tensor $(\alpha_{\rho\sigma})_{mn}$ transforms like the matrix element of a tensor component $\int \psi_n^* \alpha_{\rho\sigma} \psi_m d\tau$.[9] Notice that this matrix element does not contain the intermediate states explicitly. The selection rules are determined by the properties of the initial and final states. This is most useful, as it is not generally possible to determine selection rules by evaluating equation (1.5).

According to the rules of group theory[11] the transition mn is Raman active if and only if the representation Γ of one or more of the tensor

components $\alpha_{\rho\sigma}$ occurs in the reduction of $\Gamma_n \times \Gamma_m^*$. Γ_n, Γ_m are symmetry representations of the wave vectors ψ_n, ψ_m. The transformation properties of $\alpha_{\rho\sigma}$ are listed in Heine[11] for a set of molecular point groups which includes the 32 crystal point groups.

The scattering tensor can be separated into three parts:

$$(\alpha_{\rho\sigma})_{mn} = (\alpha^i + \alpha^s_{\rho\sigma} + \alpha^a_{\rho\sigma})_{mn}.$$

The isotropic part

$$(\alpha^i)_{mn} = \frac{1}{3}(\alpha_{xx} + \alpha_{yy} + \alpha_{zz})_{mn}$$

$$= \frac{1}{3h} \sum_r \frac{\nu_{rm}+\nu_{rn}}{(\nu_{rm}-\nu_o)(\nu_{rn}+\nu_o)} \left[\sum_\sigma (M_\sigma)_{rn}(M_\sigma)_{mr}\right].$$

The symmetric part

$$(\alpha^s_{\rho\sigma})_{mn} = \tfrac{1}{2}(\alpha_{\rho\sigma} + \alpha_{\sigma\rho})_{mn} - (\alpha^i)_{mn}$$

$$= \frac{1}{2h} \sum_r \frac{\nu_{rm} + \nu_{rn}}{(\nu_{rm}-\nu_o)(\nu_{rn}+\nu_o)} \left[(M_\rho)_{rn}(M_\sigma)_{mr}\right.$$

$$\left. + (M_\sigma)_{rn}(M_\rho)_{mr}\right] - (\alpha^i)_{mn}.$$

The antisymmetric part

$$(\alpha^{a}_{\rho\sigma})_{mn} = \tfrac{1}{2}(\alpha_{\rho\sigma} - \alpha_{\sigma\rho})_{mn}$$

$$= \frac{2\nu_o+\nu_{mn}}{2h} \sum_r \frac{1}{(\nu_{rm}-\nu_o)(\nu_{rn}+\nu_o)} [(M_\rho)_{rn}(M_\sigma)_{mr}$$

$$- (M_\sigma)_{rn}(M_\rho)_{mr}].$$

The isotropic part is a scalar quantity and thus transforms as the identity representation. As the sum of the diagonal elements of a tensor is called its trace, $(\alpha^{i})_{mn}$ gives rise to "trace" scattering. The selection rules for $(\alpha^{s}_{\rho\sigma})_{mn}$, a symmetric tensor with zero trace, are identical with those of quadrupole radiation. Hence the $(\alpha^{s}_{\rho\sigma})_{mn}$ contribution is referred to as the "quadrupole" scattering. The antisymmetric part represents an axial vector, and gives rise to "magnetic dipole" scattering because of the similarity with magnetic dipole radiation. Magnetic dipole scattering has a different frequency dependence from that of trace and quadrupole scattering. For small frequencies it drops off much faster than the other two.

The scattering intensity is now proportional to

$$|(\alpha_{\rho\sigma})_{mn}|^2 = |(\alpha^{i})_{mn}+(\alpha^{s}_{\rho\sigma})_{mn}+(\alpha^{a}_{\rho\sigma})_{mn}|^2,$$

indicating that the amplitudes and not the intensities of the three components are added.

1.4 The Polarizability Theory

A direct application of the general scattering equation (1.6) is prohibitively difficult for all but the simplest atomic systems. The main difficulty is a lack of information about the intermediate states involved in the summation. However, Placzek[9] has shown that some simplifications are possible in the case of molecules.

First the adiabatic approximation is used to separate the wave function of the molecular system into two factors: one the wave function for the electrons moving in the field of the nuclei which are held fixed in an arbitrary configuration, and the other the wave function for the nuclei moving in some effective potential given by the eigenvalues of the electronic motion. In calculating the scattered radiation the molecules are first assumed to possess fixed nuclei; subsequently the scattering is modified by the nuclear motions. It is also assumed that the scattering intensity for any instantaneous positions of the moving nuclei is identical

with the value for stationary nuclei in the same positions.

At ordinary temperatures a molecular system is practically always in a state belonging to the lowest electronic level. Provided this level is non-degenerate, the scattering tensor can be shown to be

$$(\alpha_{\rho\sigma})_{o\upsilon,o\upsilon'} = (\alpha_{\rho\sigma})_{\upsilon,\upsilon'} = \int \chi^{*}_{o\upsilon'}(q)\,\alpha_{\rho\sigma}(q)\,\chi_{o\upsilon}(q)\,dq, \quad (1.7)$$

where $\chi_{n\upsilon}$ is the nuclear vibrational wave function, n the electronic quantum number, υ the nuclear vibration number and q refers to the nuclear coordinates. $\alpha_{\rho\sigma}$ represents the polarizability of the electronic ground state. In deriving this expression, the following approximations were necessary:

(1) Because of the relatively large nuclear mass, only the electronic polarizability need be considered.

(2) The Raman frequency shifts must be small compared with both the frequency of the incident light ν_o and the frequency difference $\nu_e - \nu_o$, where ν_e is the lowest electronic absorption frequency.

Under these conditions the polarizability tensor is symmetric, because the magnetic dipole scattering

vanishes. Near resonance the magnetic dipole term is significant and may allow new lines to appear in the Raman spectrum.

Calculation of the polarizability matrix element requires a knowledge of the vibrational wave functions and the ground state polarizability. The latter quantity is generally not known. If the wave function is written as a product of harmonic oscillator functions each depending on a suitable normal coordinate q_j describing the nuclear vibrations, then the polarizability can be expanded in terms of these normal coordinates.[9] The expansion is taken as a Taylor series around the equilibrium configuration of the ground state.

$$\alpha_{\rho\sigma}(q) = \alpha^{o}_{\rho\sigma} + \sum_j \left(\frac{\partial \alpha_{\rho\sigma}}{\partial q_j}\right)_o q_j + \tfrac{1}{2}\sum_{jk} \left(\frac{\partial^2 \alpha_{\rho\sigma}}{\partial q_j \partial q_k}\right)_o q_j q_k + \cdots \quad (1.8)$$

The first term in the expansion gives rise to Rayleigh scattering; the second gives rise to Raman shifts corresponding to fundamental vibrational energies; and the third term produces Raman scattering from combinations and overtones of two fundamentals. The higher terms will influence these processes, but only to a very small extent.

The result of all these approximations and simplifications is that the intensity and polarization of the Raman line now depends upon the nuclear-coordinate dependence of the ground-state polarizability which no longer involves the difficulty of the summation over intermediate states. The polarizability derivatives can be calculated by methods employing the variational technique.[15]

Placzek's polarizability theory has formed the basis for most theoretical work in the Raman effect. Particularly in the case of calculating Raman intensities for molecules. Recently Albrecht,[12] Ting[13] and Koningstein[14] have outlined other approximations which do not involve the expansion of $\alpha_{\rho\sigma}$ in terms of normal coordinates.

1.5 The Raman Effect in Crystals*

The first systematic account of Raman scattering by phonons was presented by Born and Bradburn.[16] Their theory is a straight-forward extension of Placzek's polarizability theory for molecules, and utilizes the

---

*This discussion is limited to Raman scattering by lattice vibrations.

Born theory of lattice dynamics.[17]

Following Born and Huang,[17] the Raman scattering intensity per unit time per unit solid angle is

$$I = \frac{(\omega_o+\omega_{vv'})^4}{2\pi c^3} \sum_{k=1,2} \sum_{\alpha\gamma\beta\lambda} n^k_\alpha n^k_\beta i_{\alpha\gamma,\beta\lambda} E^-_\gamma E^+_\lambda, \qquad (1.9)$$

where ω_o is the frequency of the exciting light and $\omega_{vv'}$ is the frequency of a vibrational transition from state v to another state v'. $\underline{n}^1$ and $\underline{n}^2$ are two mutually perpendicular unit vectors which describe the polarization of the scattered radiation. $i_{\alpha\gamma,\beta\lambda}$ denotes the product of matrix elements* of the electronic polarizability, and E^-_γ and E^+_λ describe the electric field of the incident light. The electric field is given by

$$\underline{E}(t) = \underline{E}^- e^{-i\omega_o t} + \underline{E}^+ e^{i\omega_o t}, \qquad (1.10)$$

---

*The matrix elements in Born and Huang are written in the reversed notation. If A is some real linear operator, then the matrix element connecting states m and n is written here as $A_{mn} = \langle n|A|m\rangle$. In Born and Huang this would be written as $A_{mn} = \langle m|A|n\rangle$. The relationship between the two matrix elements is $\langle n|A|m\rangle = [\langle m|A|n\rangle]^*$.[18]

where $\underline{E}^- = (\underline{E}^+)^*$ is an arbitrary constant vector. The factor

$$i_{\alpha\gamma,\beta\lambda} = \left[P^{vv'}_{\alpha\gamma}\right]^* P^{vv'}_{\beta\lambda}, \tag{1.11}$$

where the P's are the matrix elements of the polarizability.

$$\left[P^{vv'}_{\alpha\gamma}\right]^* = \langle v | P^*_{\alpha\gamma} | v' \rangle,$$

and $v \neq v'$ (1.12)

$$P^{vv'}_{\beta\lambda} = \langle v' | P_{\beta\lambda} | v \rangle.$$

In general, the matrix element

$$P^{mn}_{\alpha\beta} = \frac{1}{\hbar} \sum_r \left[\frac{\langle n | M_\alpha | r \rangle \langle r | M_\beta | m \rangle}{\omega_{rm} - \omega_o} + \frac{\langle n | M_\beta | r \rangle \langle r | M_\alpha | m \rangle}{\omega_{rn} + \omega_o} \right]$$

$$= \langle n | P_{\alpha\beta} | m \rangle \tag{1.13}$$

defines the $\alpha\beta$ component of the polarizability tensor for the transition from state m to state n. Equation (1.13) is a reformulation of equation (1.5). For the vibrational Raman effect, according to Placzek's theory, equation (1.13) becomes

$$P^{vv'}_{\alpha\beta} = \frac{1}{\hbar} \sum_{n'',v''} \left[\frac{\langle ov' | M_\alpha | n''v'' \rangle \langle n''v'' | M_\beta | ov \rangle}{\omega_{n''v'',ov} - \omega_o} + \frac{\langle ov' | M_\beta | n''v'' \rangle \langle n''v'' | M_\alpha | ov \rangle}{\omega_{n''v'',ov'} + \omega_o} \right]. \tag{1.14}$$

$P_{\alpha\beta}^{vv'}$ is a function of the frequency ω_o and the coordinates X of the crystal nuclei. The quantum numbers n and v characterise the vibrational wave function $\chi_{nv}(X)$ described earlier.

The ground-state polarizability is now expanded in terms of the complex normal coordinates of the crystal.

$$\delta P_{\alpha\beta} = \sqrt{N} \sum_j P_{\alpha\beta}\left(\begin{matrix}o\\j\end{matrix}\right) Q\left(\begin{matrix}o\\j\end{matrix}\right) + \tfrac{1}{2} \sum_{\underline{k}}^{N} \sum_{ij} P_{\alpha\beta}\left(\begin{matrix}\underline{k} & -\underline{k}\\ i & j\end{matrix}\right) Q\left(\begin{matrix}\underline{k}\\ i\end{matrix}\right) Q\left(\begin{matrix}-\underline{k}\\ j\end{matrix}\right) + \cdots \quad (1.15)$$

where $\delta P_{\alpha\beta} = P_{\alpha\beta}(\omega_o, X) - P_{\alpha\beta}(\omega_o, X^o)$ is the change in the polarizability due to displacements of the nuclei, normalised for N unit cells. $Q\left(\begin{matrix}\underline{k}\\ j\end{matrix}\right)$ is the jth normal coordinate of wave vector $\underline{k}$ with corresponding frequency $\omega\left(\begin{matrix}\underline{k}\\ j\end{matrix}\right)$; j = 1, 2, - - - , 3n where n is the number of atoms in the unit cell. The coefficients $P_{\alpha\beta}\left(\begin{matrix}o\\j\end{matrix}\right)$ and $P_{\alpha\beta}\left(\begin{matrix}\underline{k} & -\underline{k}\\ i & j\end{matrix}\right)$ are the derivatives of the polarizability with respect to the corresponding normal coordinates. These coefficients can be expressed in terms of the nuclear displacements, masses and vibrational eigenvectors.

As in the case of molecules, the first-order Raman transitions are due to the linear terms in the expansion. The selection rules on energy and

momentum (wave vector) give

$$\omega_o = \omega_s \pm \omega(\overset{o}{j}) \tag{1.16}$$

and

$$\underline{k}_o = \underline{k}_s \pm \underline{k}_j, \tag{1.17}$$

where o,s refer to the incident and scattered light respectively. $\underline{k}_j$ is the wave vector of the phonon of frequency $\omega(\overset{o}{j})$. The light scattering measurements are carried out at optical frequencies where there is little dispersion of the refractive index so that $k_o \approx k_s$, Equation (1.17) now becomes

$$k_j = 2k_o \sin \theta, \tag{1.18}$$

where 2θ is the angle between the directions of the incident and scattered light. For visible light equation (1.18) reduces to $k_j \approx 0$. In the case of light scattering by the optical modes of vibration $\underline{k}_j$ may be taken equal to zero as shown in the phonon frequency $\omega(\overset{o}{j})$. This approximation can not be made for acoustic modes (Brillouin scattering) and, strictly speaking, should not be applied to Raman scattering by infrared-active phonons. The latter case leads to Raman scattering by polaritons.[19]

The second-order terms in the expansion (1.15) produce the two-phonon Raman effect. Here the final

state of the crystal after the scattering process differs from the initial state by two vibrational quanta. The energy and wave vector conservation laws governing this process are

$$\omega_o = \omega_s \pm \omega\left(\frac{k}{i}\right) \pm \omega\left(\frac{-k}{j}\right) \qquad (1.19)$$

and $$\underline{k}_o = \underline{k}_s \pm \underline{k}_i \pm \underline{k}_j \pm N\underline{K}, \qquad (1.20)$$

where $\underline{K}$ is a reciprocal lattice vector and N = 0 or 1. The last term in equation (1.20) takes account of any wave vectors which may lie outside the reduced Brillouin zone. As $k_o \simeq k_s$, equation (1.20) can be written in the Bragg condition form:

$$|\pm \underline{k}_i \pm \underline{k}_j \pm N\underline{K}| = 2k_o \sin\theta. \qquad (1.21)$$

The vibrational modes involved may be either optical or acoustical, or a combination of both. Thus the distinction between Raman and Brillouin scattering can not be made for modes with wave vectors away from the zone centre. As in the case of one-phonon scattering, equation (1.21) may be taken equal to zero for visible light. This is a good approximation for phonons with wave vectors far away from $\underline{k} = 0$. If Umklapp processes are ignored equation (1.21) becomes

$$\pm \underline{k}_i = \mp \underline{k}_j = \pm k. \tag{1.22}$$

Thus second-order Raman scattering involves contributions from pairs of phonons with equal and opposite wave vector from throughout the reduced zone. Therefore features in two-phonon Raman spectra can be related to structure in the combined density of states of the pairs of vibration modes. Such structure is associated with critical points in the reduced zone.[20]

If the wave numbers $\underline{k}$ are divided into two groups by an arbitrary plane through the origin such that $\underline{k}$ and $-\underline{k}$ lie on opposite sides of the plane, then the complex normal coordinates can be expressed in terms of real normal coordinates q_1 and q_2 as follows:

$$\begin{aligned} Q\left(\frac{k}{j}\right) &= \frac{1}{\sqrt{2}}\left[q_1\left(\frac{k}{j}\right) + iq_2\left(\frac{k}{j}\right)\right] \\ Q\left(\frac{-k}{j}\right) &= Q^*\left(\frac{k}{j}\right) = \frac{1}{\sqrt{2}}\left[q_1\left(\frac{k}{j}\right) - iq_2\left(\frac{k}{j}\right)\right]. \end{aligned} \tag{1.23}$$

The second-order term in the expansion (1.15) can now be expressed in terms of these real normal coordinates.

$$\tfrac{1}{2}\sum_{\underline{k}}^{N}\sum_{ij} P_{\alpha\beta}\left(\begin{matrix}\underline{k} & -\underline{k}\\ i & j\end{matrix}\right)Q\left(\begin{matrix}\underline{k}\\ j\end{matrix}\right)Q\left(\begin{matrix}-\underline{k}\\ j\end{matrix}\right)$$

$$= \tfrac{1}{4}\sum_{\underline{k}}^{N/2}\sum_{ij}\left\{\left[P_{\alpha\beta}\left(\begin{matrix}\underline{k} & -\underline{k}\\ i & j\end{matrix}\right) + P_{\alpha\beta}\left(\begin{matrix}-\underline{k} & \underline{k}\\ i & j\end{matrix}\right)\right]\left[q_1\left(\begin{matrix}\underline{k}\\ i\end{matrix}\right)q_1\left(\begin{matrix}\underline{k}\\ j\end{matrix}\right) + q_2\left(\begin{matrix}\underline{k}\\ i\end{matrix}\right)q_2\left(\begin{matrix}\underline{k}\\ j\end{matrix}\right)\right]\right.$$

$$\left. - i\left[P_{\alpha\beta}\left(\begin{matrix}\underline{k} & -\underline{k}\\ i & j\end{matrix}\right) - P_{\alpha\beta}\left(\begin{matrix}-\underline{k} & \underline{k}\\ i & j\end{matrix}\right)\right]\left[q_1\left(\begin{matrix}\underline{k}\\ i\end{matrix}\right)q_2\left(\begin{matrix}\underline{k}\\ j\end{matrix}\right) - q_2\left(\begin{matrix}\underline{k}\\ i\end{matrix}\right)q_1\left(\begin{matrix}\underline{k}\\ j\end{matrix}\right)\right]\right\}; \quad (1.24)$$

remembering the symmetry relations

$$P_{\alpha\beta}\left(\begin{matrix}\underline{k} & -\underline{k}\\ i & j\end{matrix}\right) = P_{\alpha\beta}\left(\begin{matrix}-\underline{k} & \underline{k}\\ j & i\end{matrix}\right) = P^{*}_{\alpha\beta}\left(\begin{matrix}-\underline{k} & \underline{k}\\ i & j\end{matrix}\right).$$

The Raman scattering due to the six different types of transition are listed below together with the corresponding terms of equation (1.24).

Number	Type	Frequency	Terms Responsible
1,2	overtone	$\omega_o \mp 2\omega\left(\begin{matrix}\underline{k}\\ j\end{matrix}\right)$	$q_1^2\left(\begin{matrix}\underline{k}\\ j\end{matrix}\right)$, $q_2^2\left(\begin{matrix}\underline{k}\\ j\end{matrix}\right)$
3,4	summation	$\omega_o \mp\left[\omega\left(\begin{matrix}\underline{k}\\ i\end{matrix}\right)+\omega\left(\begin{matrix}\underline{k}\\ j\end{matrix}\right)\right]$	$q_1\left(\begin{matrix}\underline{k}\\ i\end{matrix}\right)q_1\left(\begin{matrix}\underline{k}\\ j\end{matrix}\right)$, $q_2\left(\begin{matrix}\underline{k}\\ i\end{matrix}\right)q_2\left(\begin{matrix}\underline{k}\\ j\end{matrix}\right)$
5,6	difference	$\omega_o \mp\left[\omega\left(\begin{matrix}\underline{k}\\ i\end{matrix}\right)-\omega\left(\begin{matrix}\underline{k}\\ j\end{matrix}\right)\right]$	$q_1\left(\begin{matrix}\underline{k}\\ i\end{matrix}\right)q_2\left(\begin{matrix}\underline{k}\\ j\end{matrix}\right)$, $q_2\left(\begin{matrix}\underline{k}\\ i\end{matrix}\right)q_1\left(\begin{matrix}\underline{k}\\ j\end{matrix}\right)$
		$\omega\left(\begin{matrix}\underline{k}\\ i\end{matrix}\right) > \omega\left(\begin{matrix}\underline{k}\\ j\end{matrix}\right)$	

The $\mp$ refers to Stokes or anti-Stokes scattering. The observed Raman spectrum is a superposition of the six different types of spectra, each of which is continuous.

Because of the continuous nature of second-order scattering it is convenient to reformulate equation (1.11) as a function of frequency:

$$i_{\alpha\gamma,\beta\lambda}(\omega) = \lim_{\Delta\omega\to 0} \sum_{v'}^{\omega<\omega_o+\omega_{vv'}<\omega+\Delta\omega} \langle v|P^*_{\alpha\gamma}|v'\rangle\langle v'|P_{\beta\lambda}|v\rangle \qquad (1.25)$$

$$= \sum_{v'} \langle v|P^*_{\alpha\gamma}|v'\rangle\langle v'|P_{\beta\lambda}|v\rangle\ \delta(\omega-\omega_o-\omega_{vv'}),$$

where the states v' cover a continuous energy spectrum. The intensity expression (1.9) is now

$$I(\omega)d\omega = \frac{(\omega_0+\omega_{vv'})^4}{2\pi c^3} \sum_{k=1,2} \sum_{\alpha\gamma\beta\lambda} n^k_\alpha n^k_\beta\, i_{\alpha\gamma,\beta\lambda}(\omega) E^-_\gamma E^+_\lambda d\omega. \qquad (1.26)$$

The function $i_{\alpha\gamma,\beta\lambda}(\omega)$ can be subdivided into six parts corresponding to the different types of scattering.

$$i_{\alpha\gamma,\beta\lambda}(\omega) = \sum_{i\geq j} \sum_{s=1}^{6} i^{(s)}_{\alpha\gamma,\beta\lambda}(\omega)_{ij}, \qquad (1.27)$$

such that $i_{\alpha\gamma,\beta\lambda}(\omega) = 0$ if $i \neq j$ for $s = 1,2$

$= 0$ if $i = j$ for $s = 3,4,5,6$.

1.6 Temperature Effects

So far the calculations have neglected thermal population of energy levels. To obtain the experimentally

observed intensities the theoretical formulae must be corrected for temperature effects. This involves forming the thermal average of all initial states v for a fixed transition frequency $\omega_{vv'}$ via the Boltzmann distribution function.

The thermal averages of the appropriate polarizability matrix elements are given in Born and Huang.[17] For the first-order Raman effect equation (1.11) becomes

$$i_{\alpha\gamma,\beta\lambda} = N P_{\alpha\gamma}(\overset{o}{j}) P_{\beta\lambda}(\overset{o}{j}) C(\overset{o}{j}) D(\overset{o}{j}); \qquad (1.28)$$

$$\text{where } C(\overset{o}{j}) = \frac{\hbar/2\omega(\overset{o}{j})}{1 - \exp(-\hbar\omega(\overset{o}{j})/kT)}, \qquad (1.29)$$

$$\text{and } D(\overset{o}{j}) = 1 \text{ for Stokes scattering}$$

$$= e^{-\hbar\omega(\overset{o}{j})/kT} \text{ for anti-Stokes scattering.}$$

As $P^{*}_{\alpha\beta}(\overset{k}{j}) = P_{\alpha\beta}(\overset{-k}{j})$, it follows that $P_{\alpha\gamma}(\overset{o}{j})$ and $P_{\beta\lambda}(\overset{o}{j})$ are real. The ratio of Stokes and anti-Stokes intensities is

$$\frac{I(\text{Stokes})}{I(\text{anti-Stokes})} = \frac{(\omega_o - \omega(\overset{o}{j}))^4}{(\omega_o + \omega(\overset{o}{j}))^4} e^{-\hbar\omega(\overset{o}{j})/kT}$$

for non-resonance conditions. For second-order Raman

scattering, the components of equation (1.27) become

$$\left.\begin{matrix} i^{(1)}_{\alpha\gamma,\beta\lambda}(\omega)_{jj}d\omega \\ i^{(2)}_{\alpha\gamma,\beta\lambda}(\omega)_{jj}d\omega \end{matrix}\right\} = V\int\int\int d\underline{k} P_{\alpha\gamma}\left(\begin{matrix}\underline{k} & -\underline{k} \\ j & j\end{matrix}\right) P_{\beta\lambda}\left(\begin{matrix}\underline{k} & -\underline{k} \\ j & j\end{matrix}\right) c^2\left(\frac{\underline{k}}{j}\right)$$

$$\times \begin{cases} \delta\left(\omega-\omega_o+2\omega\left(\frac{\underline{k}}{j}\right)\right) \\ e^{-2\beta\left(\frac{\underline{k}}{j}\right)}\,\delta\left(\omega-\omega_o-2\omega\left(\frac{\underline{k}}{j}\right)\right) \end{cases}$$

$$\left.\begin{matrix} i^{(3)}(\omega)_{ij}d\omega \\ i^{(4)}(\omega)_{ij}d\omega \end{matrix}\right\} = V\int\int\int d\underline{k}\left[P_{\alpha\gamma}\left(\begin{matrix}-\underline{k} & \underline{k} \\ i & j\end{matrix}\right) P_{\beta\lambda}\left(\begin{matrix}\underline{k} & -\underline{k} \\ i & j\end{matrix}\right)\right.$$

$$\left. + P_{\alpha\gamma}\left(\begin{matrix}\underline{k} & -\underline{k} \\ i & j\end{matrix}\right) P_{\beta\lambda}\left(\begin{matrix}-\underline{k} & \underline{k} \\ i & j\end{matrix}\right)\right]$$

$$\times c\left(\frac{\underline{k}}{i}\right) c\left(\frac{\underline{k}}{j}\right) \begin{cases} \delta\left(\omega-\omega_o+\left[\omega\left(\frac{\underline{k}}{i}\right)+\omega\left(\frac{\underline{k}}{j}\right)\right]\right) \\ e^{-\beta\left(\frac{\underline{k}}{i}\right)-\beta\left(\frac{\underline{k}}{j}\right)}\,\delta\left(\omega-\omega_o-\left[\omega\left(\frac{\underline{k}}{i}\right)+\omega\left(\frac{\underline{k}}{j}\right)\right]\right) \end{cases}$$

$$\left.\begin{matrix} i^{(5)}(\omega)_{ij}d\omega \\ i^{(6)}(\omega)_{ij}d\omega \end{matrix}\right\} = V\int\int\int d\underline{k}\left[P_{\alpha\gamma}\left(\begin{matrix}-\underline{k} & \underline{k} \\ i & j\end{matrix}\right) P_{\beta\lambda}\left(\begin{matrix}\underline{k} & -\underline{k} \\ i & j\end{matrix}\right) + P_{\alpha\gamma}\left(\begin{matrix}\underline{k} & -\underline{k} \\ i & j\end{matrix}\right)\right.$$

$$\left. \times P_{\beta\lambda}\left(\begin{matrix}-\underline{k} & \underline{k} \\ i & j\end{matrix}\right)\right]$$

$$\times c\left(\frac{\underline{k}}{i}\right) c\left(\frac{\underline{k}}{j}\right) \begin{cases} e^{-\beta\left(\frac{\underline{k}}{j}\right)}\,\delta\left(\omega-\omega_o+\left[\omega\left(\frac{\underline{k}}{i}\right)-\omega\left(\frac{\underline{k}}{j}\right)\right]\right) \\ e^{-\beta\left(\frac{\underline{k}}{i}\right)}\,\delta\left(\omega-\omega_o-\left[\omega\left(\frac{\underline{k}}{i}\right)-\omega\left(\frac{\underline{k}}{j}\right)\right]\right), \end{cases}$$

where $C\left(\frac{k}{j}\right)$ is defined by equation (1.29) and

$$\beta\left(\frac{k}{j}\right) = \hbar\omega\left(\frac{k}{j}\right)/kT.$$

The summation $\sum_{\underline{k}}^{N/2}$ in equation (1.24) has been replaced by $V\int\int\int d\underline{k}$, where V is the volume of the crystal.

These intensity formulae have been calculated on the assumption that the lattice vibrations are harmonic. The inclusion of anharmonic forces produces a finite line width, and results in the Raman shifts and linewidths being temperature dependent. In most cases there is a broadening of the Raman lines with increase in temperature accompanied by a shift of the Stokes lines to higher frequencies. The effect of anharmonic interactions can be accounted for by including a factor like

$$\frac{\Gamma}{(\omega_o - \omega\left(\frac{k}{j}\right) - \Delta - \omega_s)^2 + \Gamma^2}$$

in the scattering intensity formulae.[21,22] This factor represents a Lorentz distribution of half-width Γ about the frequency $\omega_o - \omega\left(\frac{k}{j}\right) - \Delta$. Δ is the temperature dependent part of the frequency shift of the Raman line. Quantum mechanical expressions for Δ and Γ are

obtained by considering three- and four-phonon interactions and the thermal expansion of the lattice.

1.7 Symmetry and Selection Rules

As mentioned earlier, the polarizability tensor is symmetric in Placzek's theory. Further symmetry restrictions are introduced by the requirement that the scattering tensor should be invariant under the operations contained in the crystal space group. Also, the symmetries of the normal coordinates describing the vibrations of atoms in the unit cell are characterized by irreducible representations of the space group of the crystal lattice. Consequently a phonon can participate in a first-order Raman transition if and only if its irreducible representation is the same as one of the irreducible representations which occur in the reduction of the representation of the polarizability tensor.

For long wavelength phonons the crystal factor group can be used in classifying the phonon symmetries. (This $\underline{k} = 0$ assumption is not valid for phonons which are simultaneously infrared and Raman active because of additional effects due to the long-range electric fields associated with polar vibrations.[22]) Ovander[23]

and Loudon[22] give the form of the Raman tensor for all representations of the 32 crystal point groups that correspond to Raman-active lattice vibrations. Ovander's list is more general in that anti-symmetric Raman tensors are also considered.

The selection rules for the second-order Raman effect are more complicated. Contributions from $\underline{k} = 0$ phonons are easily dealt with. For combination states, the Raman transition is allowed if the Kronecker product of the irreducible representations of the two phonons contains irreducible representations in common with the polarizability tensor. For overtone states, the symmetrized Kronecker square of the phonon irreducible representation must contain irreducible representations in common with the polarizability tensor. For non-zero wave vectors, it is necessary to form Kronecker products and symmetrized Kronecker squares of space-group irreducible representations corresponding to all wave vectors throughout the Brillouin zone. These calculations are more complex than those for $\underline{k} = 0$ phonons. Birman[24] has developed methods for carrying out this type of calculation.

1.8 Recent Theory

The Born-Bradburn theory has been applied extensively in explaining the Raman effect in crystals with reasonable success. A recent example is the calculation of the second-order Raman spectrum of NaI and KBr by Cowley.[25] The main features of the theory are (1) the use of semi-classical radiation theory in discussing the coupling of the light to the crystal via the electron polarizability, and (2) the expansion of the polarizability in terms of the normal coordinates to obtain the electron-lattice interaction.

The development of a better understanding of the interaction of radiation with a crystal has resulted in several new theories of Raman scattering.[26-30] The main features of these theories are (1) the use of second quantization in the treatment of the electron-radiation interaction, and (2) a more explicit and detailed examination of the electron-lattice interaction.

Strizhevskii[26] considers the quantization of the electromagnetic field in a crystal in conjunction with a phenomenological treatment of the medium using the dielectric constant tensor. The heterogeneities arising during the movement of particles of the medium (considered homogeneous on the average) lead to Raman

scattering of the electromagnetic waves. A general formula is obtained for the scattering tensor which can be applied to scattering by impurities and lattice defects as well as phonons. Because of this generality, it is difficult to gain much insight from this formula.

Ovander[27] treats the Hamiltonian of the crystal plus radiation plus interaction in the second quantization representation. The crystal is regarded as a collection of interacting molecules, and the Stokes scattering mechanism is taken to be the decay of one polariton into two. Incident radiation creates the first polariton, whose energy corresponds to a frequency in the region of crystal transparency. The other two polaritons correspond to a "red" shifted polariton in the region of transparency (the scattered radiation) and an almost purely mechanical oscillation (the phonon). The results of this theory are similar to that of Loudon.[28] Their differences, such as in the extreme case of resonance, are fully discussed in an excellent review article by Loudon.[22]

Loudon's theory[28] has become widely accepted, and will be briefly reviewed. The calculations are based on semi-conductor properties but can equally well be applied to insulators.

Loudon shows that the most important Raman interaction between the photons and phonons takes place through the intermediary of the electrons, and therefore the electronic band structure of the crystal must be taken into account. The first-order Raman scattering process is described as three virtual electronic transitions accompanied by the following photon and phonon transitions; (1) a photon ω_o is absorbed, (2) an optic phonon $\omega(\overset{o}{j})$ is created or destroyed, (3) a photon ω_s is emitted. The three transitions can occur in any time order. Transitions (1) and (3) occur through the electron-radiation interaction and (2) occurs through the electron-lattice interaction. Other higher order processes are possible but are assumed negligible as in most other theories. (Numerical estimates justify this assumption.) At the start and end of the scattering process the crystal is assumed to be in the electronic ground state with all valence bands full and all the conduction bands empty. The virtual intermediate states that occur in the theory are assumed to be free electron-hole pair states, with an electron in a conduction band and the hole in a valence band.

The three step scattering process outlined above is treated by third-order time-dependent perturbation theory to give for the Stokes scattering probability per unit time

$$W = \frac{2\pi}{\hbar^6} \sum_{\underline{k}_j, \underline{k}_s} \Big| \sum_{a,b} \frac{\langle n_o-1, n_s+1; n_j+1; 0 | H_I | a \rangle \langle a | H_I | b \rangle \langle b | H_I | n_o, n_s; n_j; 0 \rangle}{(\omega_a - \omega_o)(\omega_b - \omega_o)} \Big|^2$$

$$\times \delta(\omega_o - \omega(\underline{k}_j^o) - \omega_s), \qquad (1.30)$$

where the second-quantization formalism has been used for the radiative field. n_o, n_s and n_j are the numbers of incident photons, scattered photons and optic phonons present in the initial state. For spontaneous Raman scattering n_s can be taken to be zero. The final zero in the bra and ket denotes the electronic ground state. The summation indices a,b run over complete sets of intermediate states for the whole system, and the summation over $\underline{k}_s$ is restricted to lie within solid angle $d\Omega$.

The interaction Hamiltonian $H_I = H_{ER} + H_{EL}$, where the electron-radiation part H_{ER} contributes in the two outer matrix elements and the electron-lattice

part H_{EL} contributes in the third matrix element. H_{ER} and H_{EL} are defined in reference 28. The electron-lattice interaction is treated by the deformation potential approximation. An additional long-range electrical interaction is included in H_{EL} for Raman scattering by polar lattice vibrations. If the expressions for H_{ER} and H_{EL} are substituted into equation (1.30) the scattering probability becomes

$$W = \frac{4\pi^3 e^4}{\hbar^3 m^4 \eta^2 a^2 MN} \sum_{\underline{k}_j, \underline{k}_s} \frac{n_o(n_j+1)}{\omega_o \omega_s \omega(\overset{o}{j})}$$

$$\times \left| \xi^i_{j_{kj}} R^i_{os}(-\omega_o, \omega_s, \omega(\overset{o}{j})) \right|^2$$

$$\times \frac{(2\pi)^3}{V} \delta(\underline{k}_o - \underline{k}_j - \underline{k}_s) \delta(\omega_o - \omega(\overset{o}{j}) - \omega_s), \quad (1.31)$$

where

$$R^i_{os}(-\omega_o, \omega_s, \omega(\overset{o}{j})) = \frac{1}{V} \sum_{\alpha,\beta} \left\{ \frac{p^s_{o\beta} \Xi^i_{\beta\alpha} p^o_{\alpha o}}{(\omega_\beta + \omega(\overset{o}{j}) - \omega_o)(\omega_\alpha - \omega_o)} \right.$$

$$\left. + \text{five similar terms} \right\}. \quad (1.32)$$

The various symbols are defined as follows:

e = electron charge
m = electron mass
η = optical dielectric constant
a = lattice constant
M = reduced mass of the lattice atoms

N = number of unit cells in the crystal

V = crystal volume

$\underline{\xi}_j$ = unit vector which depends on the direction but not the magnitude of $\underline{k}_j$.

R^i_{os} = Raman scattering tensor for non-polar phonons. The subscripts o,s refer to the polarization directions of the photons ω_o, ω_s. The repeated index i is to be summed over x, y and z, and refers to the direction of polarization of the phonon.

$p^s_{o\beta}$ = electron momentum matrix element between states $|0\rangle$ and $|\beta\rangle$. Superscript s is a polarization index.

$\Xi^i_{\beta\alpha}$ = deformation potential related to the matrix element $\langle\beta|H_{EL}|\alpha\rangle$. The indices α,β specify single electron-hole pair states with energies $\hbar\omega_\alpha$, $\hbar\omega_\beta$.

The six terms in R^i_{os} arise from the six different time-ordered scattering processes. Signs attached to the frequencies in $R^i_{os}(\omega)$ are chosen so that a negative (positive) frequency corresponds to destruction (creation) of the appropriate photon or phonon. In general, R^i_{os} is not invariant under interchange of the polarizations of the incident and scattered photons. For it may be shown that

$$R^{i}_{os}(-\omega_o, \omega_s, \omega(^{o}_{j})) = R^{i}_{so}(-\omega_o + \omega(^{o}_{j}), \omega_s + \omega(^{o}_{j}), -\omega(^{o}_{j}))$$

for $\omega_o = \omega_s + \omega(^{o}_{j})$. However, when $\omega(^{o}_{j})$ is sufficiently small that it can be neglected in comparison with all other frequencies occuring in the tensor, R^{i}_{os} becomes symmetric. Thus R^{i}_{os} has the same symmetry properties as the Born-Bradburn polarizability tensor.

Loudon's theoretical work has given considerable impetus to experimental Raman spectroscopy, particularly in the investigation and understanding of Raman scattering by polaritons.

The theory of Birman and Ganguly[29] takes special account of the role of exciton states in Raman scattering. They assume that the virtual intermediate states are exciton states because the Coulomb interaction is always present between the electrons and the holes. Accordingly they consider the basic electron system in the Wannier exciton representation,[31] including bound and continuum states. The Hamiltonian for the interacting system of electrons, photons and phonons is written in second-quantized form. The resulting Raman tensor is investigated for frequency dependence and symmetry. Birman and Ganguly show that under certain conditions their tensor reduces to

Loudon's result. But at resonance there is a marked difference between the two theories. Recent experimental work on the resonance-enhanced Raman scattering in InSb[32] and the multiple-phonon resonance Raman effect in CdS[33,34] supports the Birman-Ganguly theory. These experiments clearly indicate that the exciton states must be considered. Burstein et. al.[35] give a more detailed treatment of the exciton-photon interaction in explaining exciton enhanced Raman scattering. Their theory is formulated in terms of the scattering of polaritons by optical phonons via the exciton part of the coupled modes.

Johnson's theory[30] concentrates on developing a realistic concept of the crystal phonon spectrum and the photon-phonon coupling through a microscopic approach. He shows that there is a striking parallel between the phonon spectrum and the two-phonon scattering tensors, and establishes the relationship between two-phonon scattering and the electronic terms in the phonon spectrum. This theory is too new yet to be fully tested.

The resurgence of interest in the physics of Raman scattering can be attributed in the main to the work of R. Loudon and S.P.S. Porto. The application

of new techniques developed by Porto and co-workers has enabled a rapid advancement in experimental Raman spectroscopy. The resultant wealth of experimental data has encouraged the new theoretical work outlined above. Raman spectroscopy is moving rapidly forward because of this healthy interaction between experimentalists and theoreticians.

C H A P T E R 2

THE RAMAN SPECTROMETER

The major components of a Raman spectrometer are the light source, the spectrum analyser, and the detector. Each of these components will be discussed separately and then together, when evaluating the performance of the complete system.

2.1 The Source

The requirements of a Raman light source are (1) high intensity, because Raman scattering efficiencies are very low (of the order of 10^{-7} for phonon scattering[28]); (2) true monochromatic light, because Raman lines can never be narrower than the linewidth of the exciting light; and (3) variable frequency, so as to avoid absorption and fluorescence problems associated with coloured samples. It would also help if the light source had a definite polarization and direction as this enables symmetry assignment of the Raman spectra of crystals.

Gas lasers are ideal light sources for the Raman spectroscopy of solids. They fulfil all the requirements

mentioned above, and are far superior to the conventional Raman sources such as the low-pressure mercury arc lamp. The advantages of lasers and their experimental utilization have been outlined in a review paper by Weber.[36]

We have chosen an argon ion laser as the Raman source. The reasons for this choice were (1) the argon laser gives the highest continuous output power in the visible of all the gas lasers commercially available, (2) it will operate on at least seven wavelengths in the blue-green region of the spectrum, (3) the laser may be operated at yellow and red wavelengths by changing the gas to krypton, and (4) because of the ν^4 dependence in the scattering intensity formula it is advantageous to work with blue laser lines whenever possible.

The laser purchased was a Spacerays, Inc. model 5600 argon ion laser. This laser can produce a maximum of 5 watts output power distributed over the seven wavelengths 4579, 4658, 4765, 4880, 4965, 5017 and 5145Å. Of the total output approximately 80% of the power is equally shared by the 4800 and 5145Å lines. The laser is normally operated in the single wavelength mode. This is achieved by replacing one of

conventional laser-cavity concave mirrors with a Brewster-angled reflecting prism.[37] The operating wavelength is selected by rotating the prism. There is an added bonus in that the laser cavity is now hemispherical, so that full output power may be obtained in the lowest-order radial mode. The laser lines have a half-width of about 0.15 cm^{-1}.

The d.c. gas discharge is contained in a water-cooled fine-bore quartz tube surrounded by a plasma-pinching solenoidal magnet. The anode and cathode are placed off-axis, and the ends of the discharge tube are sealed with replaceable Brewster's-angle windows. The system is particularly attractive to us because the laser is completely demountable for maintainence purposes, and the continuous gas flow design allows the use of industrial grade argon gas. The disadvantages are the fact that the Brewster windows need replacing every 15 operating hours because of contamination,[38] and that the cathode needs reactivating every 30 hours. However, neither of these operations is difficult or time consuming.

The Spacerays laser is shown in the photograph Fig. 2.1. A pair of Spectrogard laser safety glasses can be seen on the bench at the left-hand end of the

Fig. 2.1. The Argon Laser

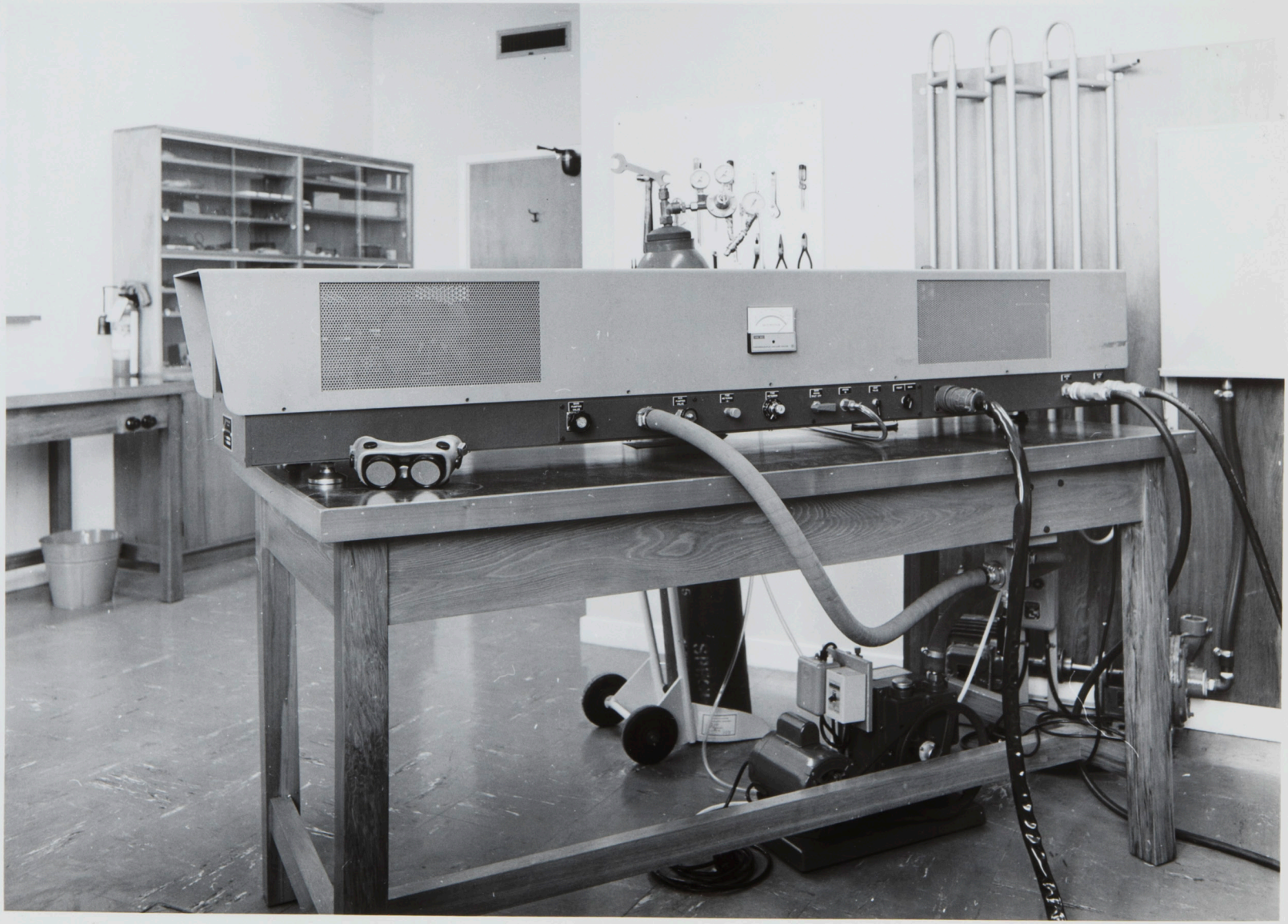

laser. These safety glasses are part of a set of safeguards[39] that are used to protect operating personnel. It cannot be over-emphasized that the argon laser beam is dangerous. A low power He-Ne laser is used for optical and other alignment work associated with the Raman spectrometer. This laser too is sufficiently powerful to cause eye damage.

2.2 The Spectrum Analyser

The requirements of the spectrum analyser are (1) a medium resolving power consistent with high optical speed; (2) a low stray light factor, because Raman scattering is so weak compared with Rayleigh scattering; and (3) the use of gratings as the dispersive elements, because of their near linear wavelength dispersion and general superiority over prisms. A double (or even triple) grating monochromator would be ideal, especially if it had a wavenumber grating drive. A detailed investigation[40] of light scattering within grating instruments demonstrated that a double monochromator is essential if weak Raman spectra are to be observed. The use of interferometrically ruled gratings is advisable because of their low ghost intensity.[41]

At the time we purchased our first double monochromator only two manufacturers, Spex and Jarrell-Ash, were producing suitable spectrometers. The instrument decided upon was the Jarrell-Ash 1/3 m - 1 m double monochromator system.[42] The reasons for this decision were (1) private enquiries had shown that the early models of the Spex tandem 3/4 m spectrometer were not altogether satisfactory, (2) the Jarrell-Ash double 1 m system was not yet operational, and was certain to be too expensive, (3) the 1/3 m - 1 m system was as efficient optically as the Spex 3/4 m and had the advantage of increased resolution, (4) the 1/3 m unit was easily removeable so that the 1 m section could be used with other equipment in separate experiments, and (5) by opening up the slits on the 1/3 m unit the 1 m section could be used as a photographic instrument or for signal averaging (to be described later) without separating the monochromators. The one major disadvantage of the system is that the stray light level is over five times higher than in the double 1 m system. We were also concerned about the accuracy of the grating tracking because the two monochromators were coupled through separate drive screws. However, Jarrell-Ash guaranteed that the system would track accurately enough.

The 1/3 m - 1 m double monochromator system as purchased comprises a type 84-527 0.33 m pre-monochromator coupled to a type 78-463 Czerny-Turner spectrometer. The two instruments bolt together, and their grating drives are coupled via a drive shaft taken from the control unit in the 1 m. A field lens in placed between the two spectrometers to match their apertures. A drawing of the instrument can be seen in Fig. 2.6.

The specifications of the 1/3 m are a concave grating mount of the Robin type with a 0.333 m radius grating (ruled area 33 x 33 mm, 590 grooves/mm, blazed for 6000Å); with a 5 cm high curved entrance slit; and with drive synchronization to provide scanning speed ratios in integral steps from 1:1 to 50:1. The 1 m specifications are a plane grating mount of the Czerny-Turner type with concave mirrors of 1 m focal length; with a 590 grooves/mm grating (102 x 102 mm ruled area, blazed for 10,000Å); with 5 cm high curved entrance and exit slits; and with camera facilities for taking plates.

The effective aperture of the 1 m at f/8.7 and a resolution of about 0.1Å in the second-order visible are consistent with the requirement of medium resolving

power and high optical speed. The use of curved slits means that the full resolution is obtained at full slit height. This is an important factor in photoelectric work where the use of maximum slit height can increase the signal level. The 1 m grating was chosen for use over a wide spectral region to cope with other experimental requirements. Consequently the grating parameters are not optimised for Raman spectroscopy. The grating will be used in second-order for work in the 5000Å region. As a result the grating ghosts will be more prominent than those for a similar first-order grating.[41]

In a double monochromator the dispersions of the individual elements may be crossed or additive.[43] If the two monochromators are identical then this is an important effect. Here, however, the 1/3 m dispersion is much less than that of the 1 m, and only the 1 m dispersion need be considered.

2.3 Spectrometer Dispersion

When interpreting spectra it is useful to know the spectral resolution of the spectrometer. The resolution is partly determined by the spectral slit

width, which is related to the mechanical slit width by

$$\text{spectral slit } (cm^{-1}) = \left(\frac{\partial \bar{\nu}}{\partial x}\right) \times \text{mechanical slit (mm)}. \quad (2.1)$$

The reciprocal linear dispersion $\frac{\partial \bar{\nu}}{\partial x}$ is the relating function. This function can be derived from the general grating equation[44]

$$n\lambda = d(\sin i + \sin \theta), \quad (2.2)$$

where λ is the wavelength of the light incident at angle i and diffracted at angle θ by the plane grating, d the grating spacing, and n the diffraction order.

The reciprocal angular dispersion is obtained by differentiating equation (2.2) with respect to θ;

$$\frac{d\lambda}{d\theta} = \frac{d \cos \theta}{n}. \quad (2.3)$$

Here it has been assumed that i is constant, which implies that the grating is stationary. This formula is the one most often quoted in the literature. It is seldom noted that θ can be eliminated from the equation if i = 0. For then equation (2.2) becomes

$$n\lambda = d \sin \theta,$$

and therefore

$$\cos\theta = \left[1 - \left(\frac{n\lambda}{d}\right)^2\right]^{\frac{1}{2}},$$

so that

$$\frac{d\lambda}{d\theta} = \lambda\left[\left(\frac{d}{n\lambda}\right)^2 - 1\right]^{\frac{1}{2}}. \qquad (2.4)$$

The reciprocal linear dispersion in the focal plane of the spectrometer is given by

$$\frac{d\lambda}{dx} = \frac{\lambda}{f}\left[\left(\frac{d}{n\lambda}\right)^2 - 1\right]^{\frac{1}{2}}, \qquad (2.5)$$

using $dx = fd\theta$, where f is the focal length of the spectrometer's exit mirror.

The dispersion formulae (2.3) and (2.5) both apply to a photographic instrument where the grating is fixed. A photoelectric instrument with fixed slits determines a unique light path, so that the grating must be rotated in order to scan the spectrum. Equations (2.3) and (2.5) no longer apply, and a search of the relevant review literature failed to produce a substitute. This made it necessary to derive a suitable formula from first principles.*

---

*Subsequent to this work a similar derivation was published by Hard and Lord.[45] They omit the minus sign in equation (2.9).

If α is the angle between the incident light and the spectrometer axis (see Fig. 2.2(a)) then

$$i = \theta - 2\alpha \tag{2.6}$$

and equation (2.2) becomes

$$n\lambda = 2d \sin(\theta-\alpha) \cos \alpha. \tag{2.7}$$

This is an exact equation with variables λ and θ. Differentiating equation (2.7) with respect to θ gives

$$\frac{d\lambda}{d\theta} = \frac{2d}{n} \cos (\theta-\alpha) \cos \alpha.$$

Using equation (2.7) to eliminate the cos $(\theta-\alpha)$ term we find

$$\frac{d\lambda}{d\theta} = \lambda\left[\left(\frac{2d \cos \alpha}{n\lambda}\right)^2 - 1\right]^{\frac{1}{2}}. \tag{2.8}$$

Or, in terms of wavenumber $\bar{\nu}$,

$$\frac{d\bar{\nu}}{d\theta} = -\bar{\nu}\left[\left(\frac{2\bar{\nu}d \cos \alpha}{n}\right)^2 - 1\right]^{\frac{1}{2}}. \tag{2.9}$$

The angle of rotation of the grating is $\theta-\alpha = i + \alpha$. Rotating the grating by angle $\delta\theta$ means that the diffracted angle changes by $2\delta\theta$, as the incident light has a fixed direction. Therefore $dx = f.2d\theta$, and the reciprocal linear dispersion is

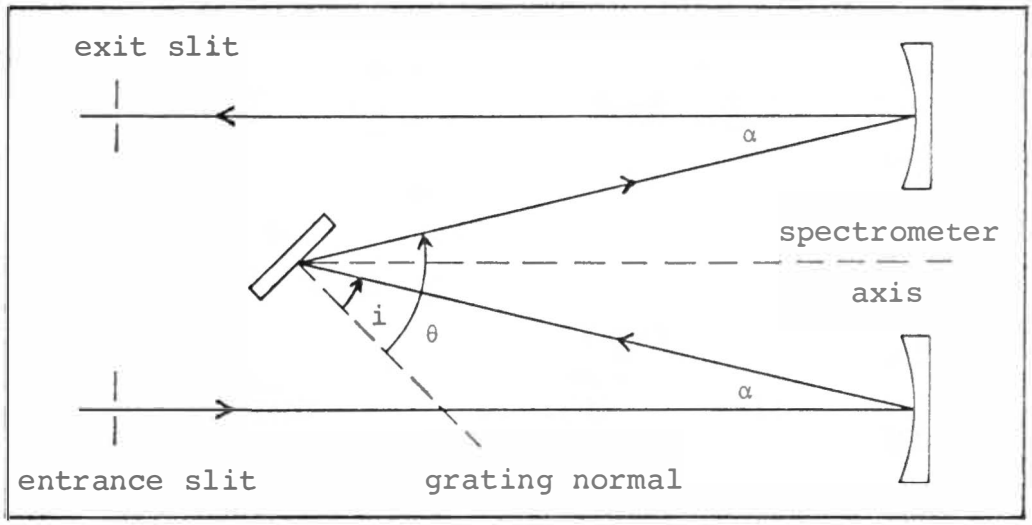

(a)

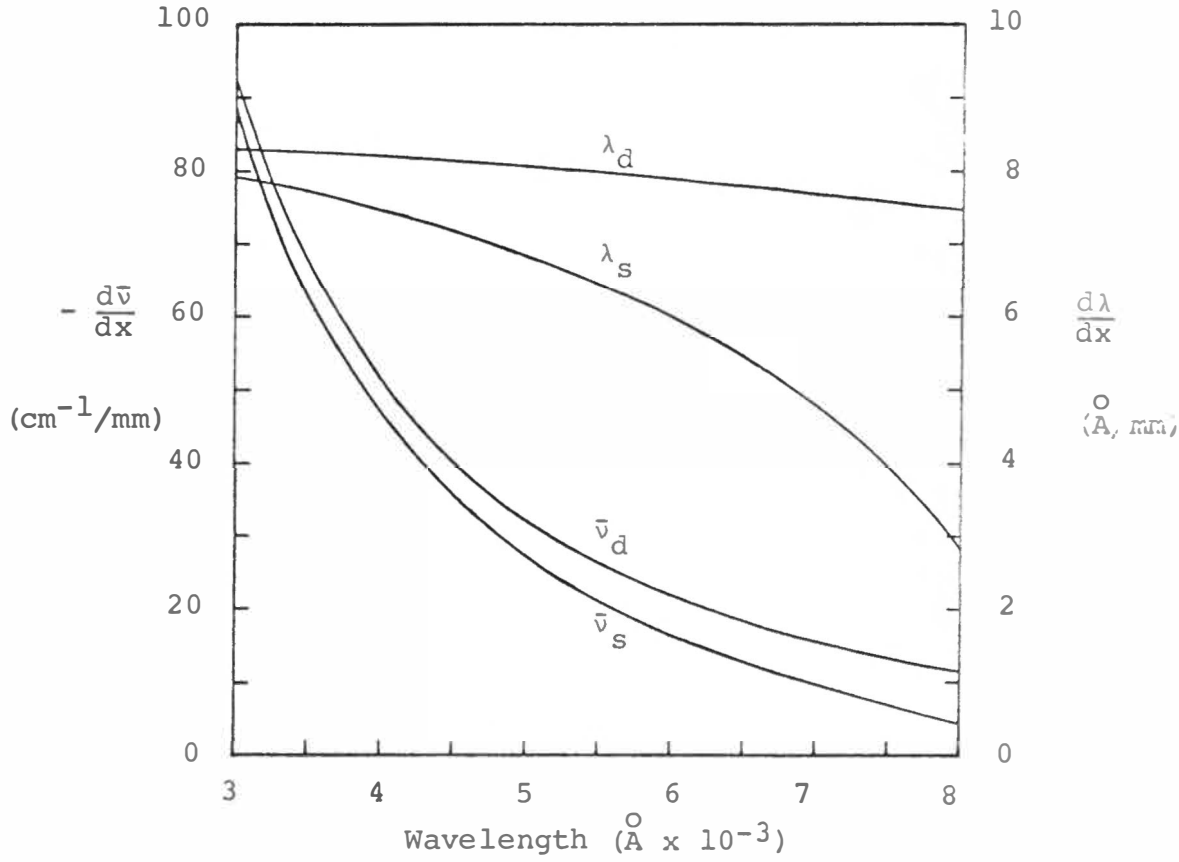

(b)

Fig. 2.2. (a) Optical path and grating angles in a Czerny-Turner spectrometer.

(b) Spectrometer dispersion curves.

$$\left.\begin{aligned} \frac{d\lambda_d}{dx} &= \frac{\lambda}{2f}\left[\left(\frac{2d\cos\alpha}{n\lambda}\right)^2 - 1\right]^{\frac{1}{2}}, \\ \text{or} \\ \frac{d\bar{\nu}_d}{dx} &= -\frac{\bar{\nu}}{2f}\left[\left(\frac{2\bar{\nu}d\cos\alpha}{n}\right)^2 - 1\right]^{\frac{1}{2}}. \end{aligned}\right\} \qquad (2.10)$$

This may be compared with

$$\left.\begin{aligned} \frac{d\lambda_s}{dx} &= \frac{d\cos\theta}{fn}, \\ \text{or} \\ \frac{d\bar{\nu}_s}{dx} &= -\frac{\bar{\nu}^2 d\cos\theta}{fn} \end{aligned}\right\} \qquad (2.11)$$

from equation (2.3), and

$$\left.\begin{aligned} \frac{d\lambda_s}{dx} &= \frac{\lambda}{f}\left[\left(\frac{d}{n\lambda}\right)^2 - 1\right]^{\frac{1}{2}}, \\ \text{or} \\ \frac{d\bar{\nu}_s}{dx} &= -\frac{\bar{\nu}}{f}\left[\left(\frac{\bar{\nu}d}{n}\right)^2 - 1\right]^{\frac{1}{2}} \end{aligned}\right\} \qquad (2.12)$$

from equation (2.5). It is proposed that equation (2.10) be called the dynamic dispersion to distinguish it from equations (2.11) and (2.12) which refer to the static case.

Equations (2.10) and (2.12) are plotted as a function of wavelength in Fig. 2.2(b). The dispersion curves apply to the 1 m Czerny-Turner spectrometer,

for which f = 1000 mm, n = 2, d = $\frac{1}{590}$ mm and $\alpha = 4^{o}18'$.[46] Equation (2.11) is not easily plotted, as it is a function of θ and i. A dispersion curve may be obtained for each value of i. For comparison purposes we choose i so that the grating is being used at the blaze angle $a = 17^{o}12'$. This corresponds to an operating wavelength of 5000Å in the second-order, where Raman spectra excited by the argon laser will be observed. At the blaze wavelength the spectrometer axis is normal to the blazed face of the grating so that $i = a-\alpha = 12^{o}54'$. Using this value for i, and equations (2.2) and (2.11), the reciprocal linear dispersion has been calculated for different values of θ. Some results are shown in Table 2.1.

Table 2.1 A comparison of dispersions.

Wavelength (Å)	Dispersion (Å/mm)		
	Eq.(2.10)	Eq.(2.11)	Eq.(2.12)
4800	8.10	7.96	6.98
5000	8.07	7.88	6.84
5200	8.04	7.80	6.69

Table 2.1 shows that the reciprocal dispersion in Å/mm

is almost linear and that the real dispersion in mm/Å is greater in the static case. The difference between the exact static dispersion given by equation (2.10) and that given by equation (2.11) is an indication of the accuracy of the approximation i = 0. For equations (2.10) and (2.11) to produce the same dispersion a must equal α. Physically this means using a 295 grooves/mm grating at the blaze wavelength (5000Å).

The ultimate resolution of the spectrometer is about 0.1Å in the 5000Å region. Therefore for slit widths greater than approximately 12μ the resolution is slit-width limited, and equation (2.1) determines the spectral resolution.

2.4 The Detector and Electronics

The requirements on the detection of the scattered light are that the detector should have a high quantum efficiency and low noise characteristics. Photoelectric detectors have a much higher quantum efficiency in the visible region than photographic detectors,[47] and have a linear intensity response. Besides this, the proper use of a double monochromator precludes the use of photographic detection. For these reasons photomultipliers were chosen as the basic

detectors of the scattered light. Even so, photographic facilities are useful for rapid survey work. A brief exposure on a high speed film such as Polaroid 3000ASA gives an overall view of the Raman spectrum. The details can then be investigated by photoelectric techniques. Such photographs can also be used to check the optical alignment of the sample with respect to the Raman spectrometer.

The photomultipliers used in this work were the EMI types 9558QA and 6255SA. The tubes were selected for high sensitivity and low noise. Both of these tubes have 2 inch diameter photocathodes which enables full use of the 5 cm curved slits on the spectrometer. The 9558QA tube has a S-20 spectral response, whereas the 6255SA has a special "S" type photocathode. The respective spectral response curves are shown in Fig. 2.4(d). It is obvious that the 9558QA tube has a higher quantum efficiency and therefore could be expected to make the use of the other tube unnecessary. However, the "S" cathode has been processed for minimum thermionic emission and consequently the 6255SA has a much lower dark current than the S-20 tube. This advantage is obtained at the expense of red sensitivity, and therefore the 9558AQ photomultiplier must be used

for detecting light at the red end of the spectrum. Otherwise the 6255SA tube should be used, despite its lower quantum efficiency.

The thermal dark current, and hence the noise, can be further reduced by cooling the photocathode. An investigation of the temperature dependence of the dark current[48] has shown that thermionic emission is reduced to a very small proportion of the dark current at temperatures below $-20^{o}C$ for both tube types. Cooling the tubes below $-40^{o}C$ does not further reduce the dark current, and in some cases may actually result in an increase in dark current.[49] Our photomultipliers can be cooled to a temperature of $-25^{o}C$ by means of a Jarrell-Ash model 83-056 thermoelectric refrigerator. This unit features complete electrostatic and magnetic shielding of the photomultiplier, and the shield is electrically connected to the cathode in accordance with EMI recommendations. A temperature stability of $\pm 0.5^{o}C$ is guaranteed.

The photomultipliers are operated with the anode at ground potential using standard epoxy-potted dynode chain-socket assemblies supplied by Jarrell-Ash. The negative high voltage needed to run the tubes is provided by a Hewlett-Packard model 6516A

d.c. power supply. This supply has an adjustable output of 0-3000 V d.c. in IV steps at 0 - 6 mA, and has excellent load-line regulation and stability. A stable power supply is necessary because photomultiplier gain is sensitive to voltage changes. Each tube is operated at a voltage determined partly by the recommended value given on a certificate accompanying the tube; and partly by resistor values in the dynode chain, as EMI advise that the optimum cathode-to-first dynode voltage is 150 V for both tubes. These considerations lead to an operating voltage of 1300 V for the 9558QA and 1150 V for the 6255SA. If more gain is required the voltage can be increased at the expense of higher noise levels.

The photomultiplier signal is processed by one of two systems; a synchronous (lock-in) amplifier system or a photon counting system. The first system is most useful at the average signal levels, whereas the second operates best at the very lowest light levels. It has been established that photon counting techniques are much superior to analogue systems when dealing with weak photomultiplier signals.[50-56] In general, the Raman spectrum is scanned using the lock-in amplifier system, and then probed with the more sensitive photon counting system if necessary.

The lock-in amplifier technique involves selective modulation of the signal information, amplification with a tuned amplifier, phase-sensitive detection, and low pass filtering. Translating the signal information to a frequency region where 1/f noise is minimised combined with narrow-bandwidth amplifiers decidedly improves the signal-to-noise ratio over d.c. amplifier systems. Our lock-in system is built around a PAR model HR-8 synchronous amplifier. This amplifier is precise, versatile and has excellent noise rejection. It is probably the best amplifier of this type currently available on the commercial market. The HR-8 uses a high input impedance preamplifier which has 21 input ranges from 100 nV to 500 mV rms full scale in a 1-2-5 sequence. The photomultiplier load resistance and signal chopping frequency were chosen at 100 kΩ and 840 Hz respectively so as to minimise amplifier noise. The synchronous-motor driven mechanical chopper assembly is placed inside the argon laser cavity at the Brewster-prism end (see Fig. 2.6). In this arrangement the chopper modulates the laser beam and not the non-laser fluorescence frequencies for which the feedback from the prism mirror is negligible.[57] The amplifier reference signal is derived from this same chopper by

means of a lamp-solar cell unit. The amplified photomultiplier signal is displayed on a Bristol model 552 0-10 mV chart recorder.

In the photon counting system, the photomultiplier output pulses are amplified, passed through a pulse height discriminator, and then counted with a ratemeter and recorded. Pulse amplifiers and discriminators are widely used in nuclear physics experiments. Consequently there are many commercial suppliers of these instruments. However, the commercial models are usually expensive and generally more sophisticated than is necessary for the low count-rates encountered in Raman spectroscopy. For this reason we decided to build our own unit based on Fairchild high speed integrated circuits. The resulting photon counting system is inexpensive, economical on parts, and satisfactory in performance.

Fig. 2.3 is a schematic circuit of the system. The photomultiplier output is first amplified by a charge sensitive preamplifier based on a μA709c operational amplifier. The conversion gain of the first stage is given by

$$\frac{E}{Q} = \frac{-A}{c_{in}+c_f(1+A)} ,$$

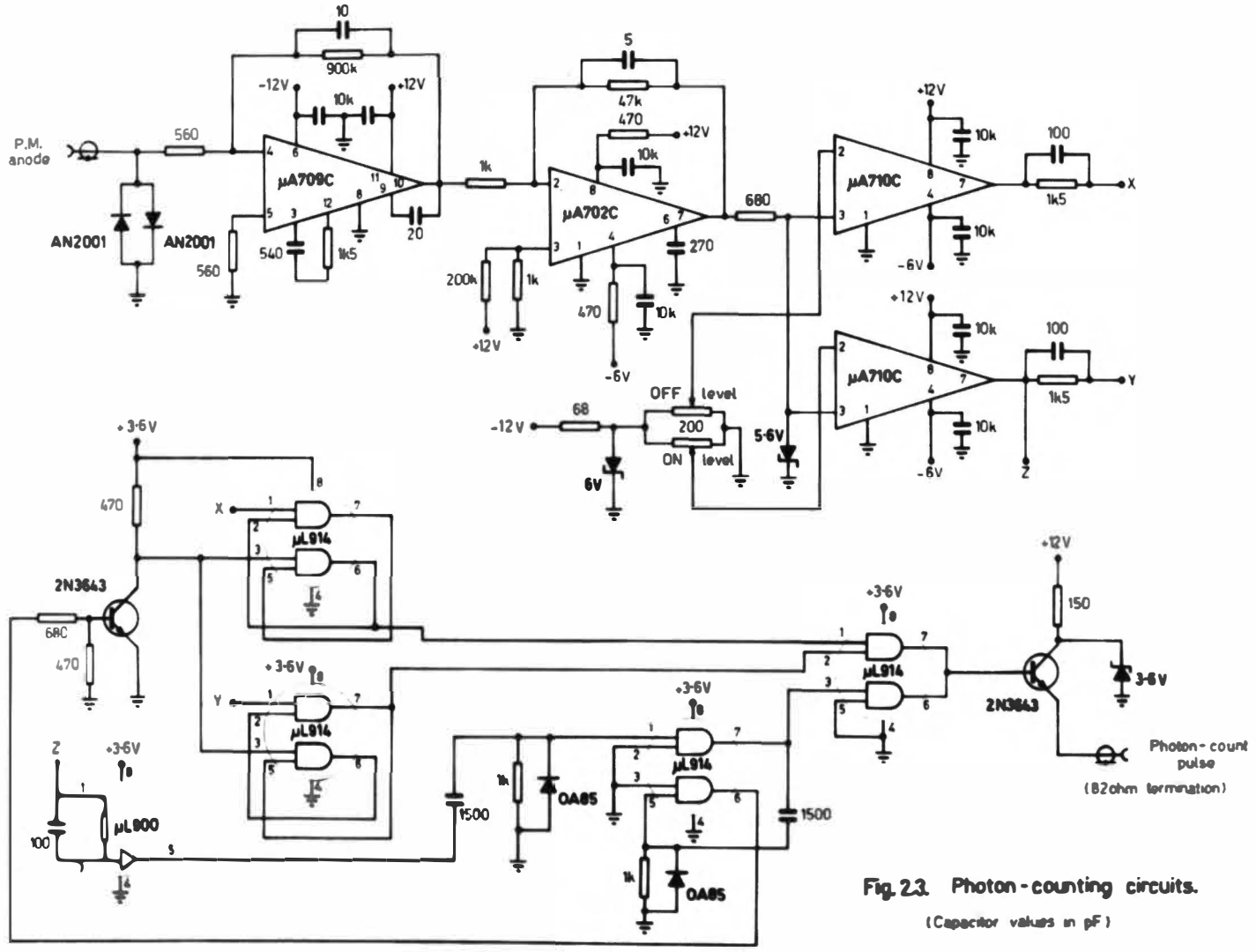

Fig. 2.3. Photon-counting circuits.

(Capacitor values in pF)

where E is the output voltage, Q the input charge, A the amplifier voltage gain, C_{in} the input capacitance, and C_f the feedback capacitance. If A>>1, so that $(A+1)C_f >> C_{in}$, then $\frac{E}{Q} \approx -\frac{1}{C_f}$. In our case A ≈ 20,000, C_f = 10 pF and C_{in} = 540 pF so that the approximation is valid, and the gain of the first stage is $\frac{E}{Q}$ ≈ 100 mV/picocoulomb. The capacitance C_{in} is provided by the 13 ft long coaxial cable connecting the photomultiplier anode to the amplifier. This cable was part of the standard Jarrell-Ash photomultiplier socket assembly and could not be shortened because of other requirements. The high input capacitance seriously affects the preamplifier preformance. The output pulse had to be severely damped to eliminate a ringing effect. The output time constant is given by the feedback network as approximately 10 μsec with an overall pulse width of 20 μsec. The μA709c is capable of producing pulses 1 μsec wide. If the extra frequency response is required, the charge preamplifier should be placed right at thephotomultiplier anode. The preamplifier is protected against voltage transients by the diode pair at its input.

The preamplifier is followed by a X50 voltage amplifier using a μA702c wideband d.c. amplifier. This

amplifier preserves the pulse shape. The pulse then enters the discriminator network which comprises two μA710c high speed differential comparators and associated logic circuitry. This section was based on an original design by M.G. Maginness of the Electrical Engineering Department, University of Canterbury. The circuitry checks that the pulse height is within a range determined by the "ON" and "OFF" 15-turn trimpots. A 2 μsec wide square output pulse is produced if the pulse height is satisfactory. There is an additional dead time of about 1 μsec to allow the flip-flops X,Y to be reset. So the overall dead time is ~ 3 μsec, which implies a maximum count-rate of better than 0.3 MHz. The discriminator output is made available through an isolating line-driver stage using a 2N3643 transistor.

Because the whole system is stable and of low noise, the level controls can be used over their entire range without producing spurious output pulses. The level controls are set to maximise the signal-to-noise ratio for any given photomultiplier. To do this it is necessary to investigate the pulse height distribution for each photomultiplier. The differential pulse height distributions for the 6255SA and 9558QA were

measured by recording the number of counts/sec within a given pulse height range. Some results are shown in Fig. 2.4(a) and (b) for both the dark current and a signal current at different ambient temperatures. The signal current was provided by a tungsten lamp light source, whose intensity was adjusted to give a count rate about 100 times higher than the dark pulses so that the latter's contribution could be neglected. The 9558QA curves were recorded with a second-stage voltage gain of 10 instead of the usual 50. Each channel number is related to the lower (ON) discriminator voltage by the factor $\times 0.1$. The channel width is 0.1V.

The graphs show that there is a noticeable drop in the dark current at the lower temperatures. The dark current falls by factors of 5 for the 6255SA and 100 for the 9558QA. This is striking evidence for the affect of red sensitivity on the thermal dark current and its temperature dependence. The 6255SA dark current increases at the higher channel numbers, probably because of noise sources such as cosmic rays and background radioactive radiation.[56]

Integral pulse height distribution curves obtained from the data in Fig. 2.4(a) are shown in Fig. 2.4(c). The dark current distribution has been fitted to the signal current distribution. Normally it would

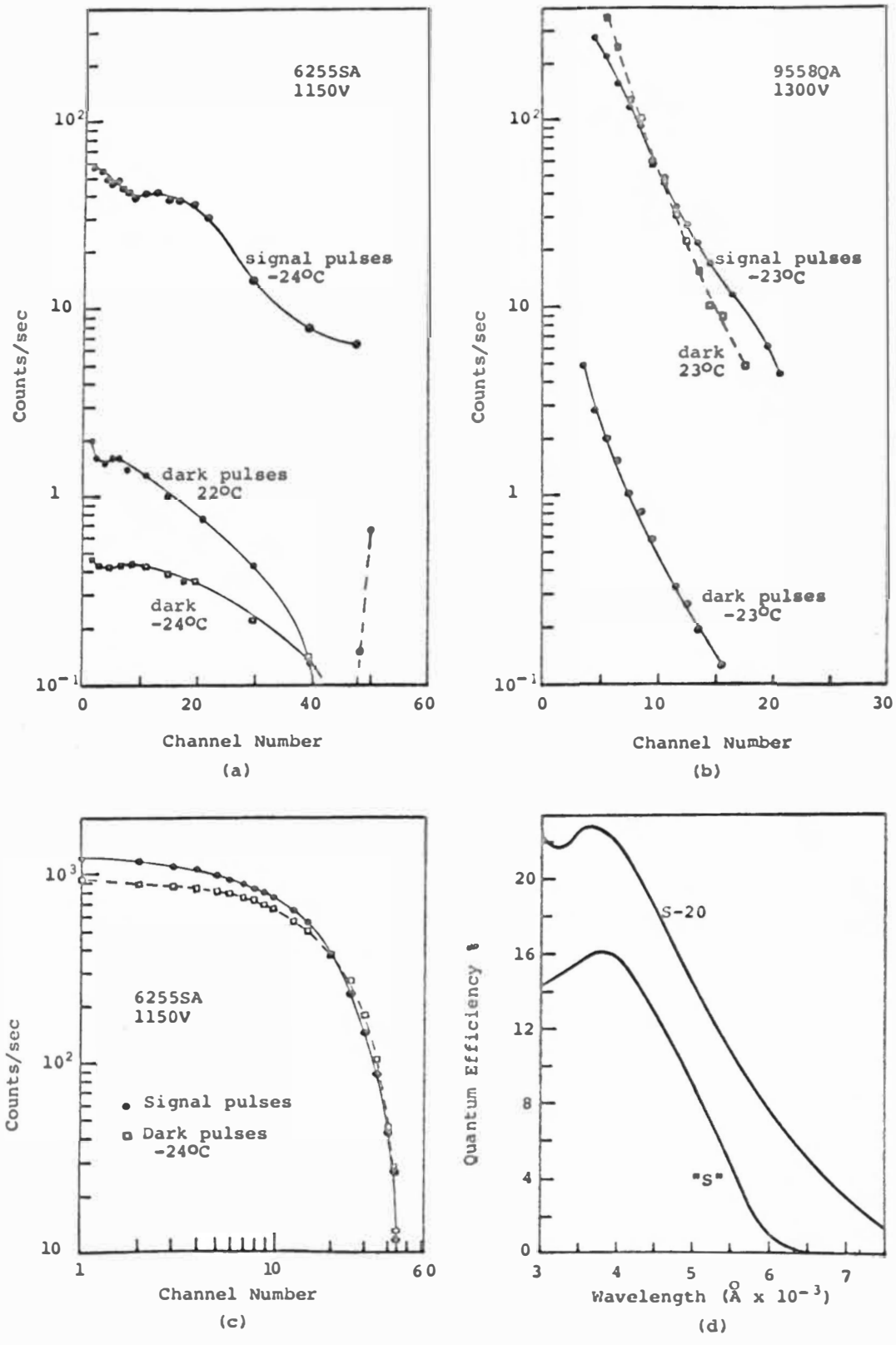

Fig. 2.4. Photomultiplier characteristics.

be below the signal distribution starting at a total integrated count of ~ 13 counts/sec. Examination of this graph shows that in photon counting there is no need to accept pulses from beyond channel 44 or below channel 3. These limits are set by the requirement that for maximum signal-to-noise ratio the dark pulse distribution should not diverge above the fitted signal pulse distribution.[56] Therefore the optimum discriminator settings for the 6255SA photomultiplier are 0.3 V for the ON level and 4.4 V for the OFF level.

Using these discriminator settings, the frequency response of the photon counting electronics was investigated. The 6255SA photomultiplier was irradiated with green light obtained from the light of a tungsten lamp passed through the 1 m spectrometer set at 5000Å. The intensity of the light incident on the photomultiplier was varied by altering the 1 m slit widths, and the corresponding count rates measured. The results are plotted in Fig. 2.5, where it can be seen that the frequency response becomes non-linear for count rates greater than 5000/sec. This figure is consistent with the 20 μsec pulse width (a rule of thumb states that the pulse separation should be 10 x (pulse width) for linear response).

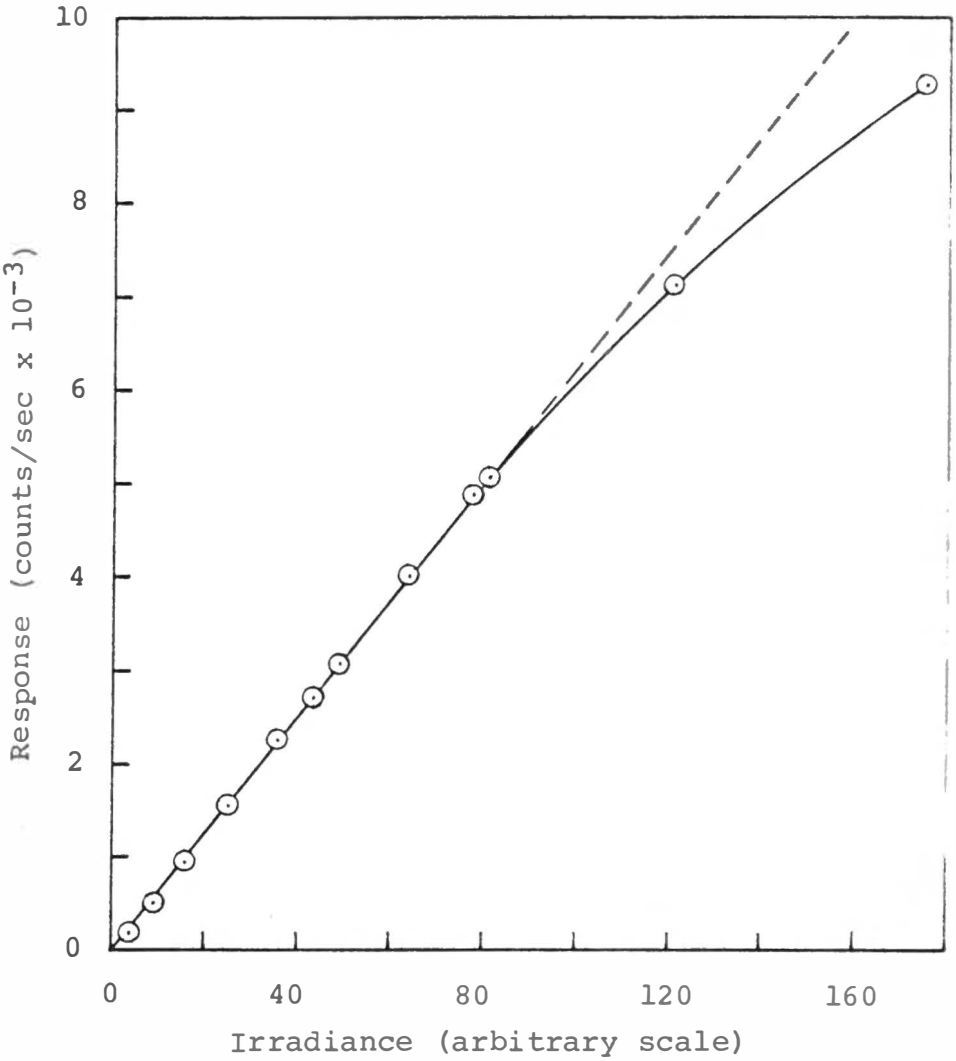

Fig. 2.5. Frequency response of photon counting electronics.

2.5 Spectrometer Performance

The complete Raman spectrometer is outlined in the diagram Fig. 2.6. The laser beam is reflected up into the sample by means of a prism, and the scattering geometry is arranged so that the incident and scattered light are at right angles. The scattered light is directed into the spectrometer by two f/2 lenses which are placed at their focal distance (4") from the sample and 1/3 m respectively. Devices such as polarizers and filters are placed in the parallel-light region between the lenses.

The actual physical arrangement is shown in the photographs Figs 2.7 and 2.8. A low power He-Ne laser can be seen at the end of the optical bench in Fig. 2.7. Fig. 2.8 features the electronics rack in the foreground with the argon laser power supply at the rear.

The Raman spectrum of CaF_2 was measured to test the spectrometer performance. An optically clear sample of CaF_2 in the shape of a cylinder 2 cm long by 5 mm in diameter was irradiated with 4880Å laser light along the cylinder axis. The recorded Raman spectrum is shown in Fig. 2.9, where the characteristic Raman line at 322 cm^{-1} [58] can be seen. The scattering

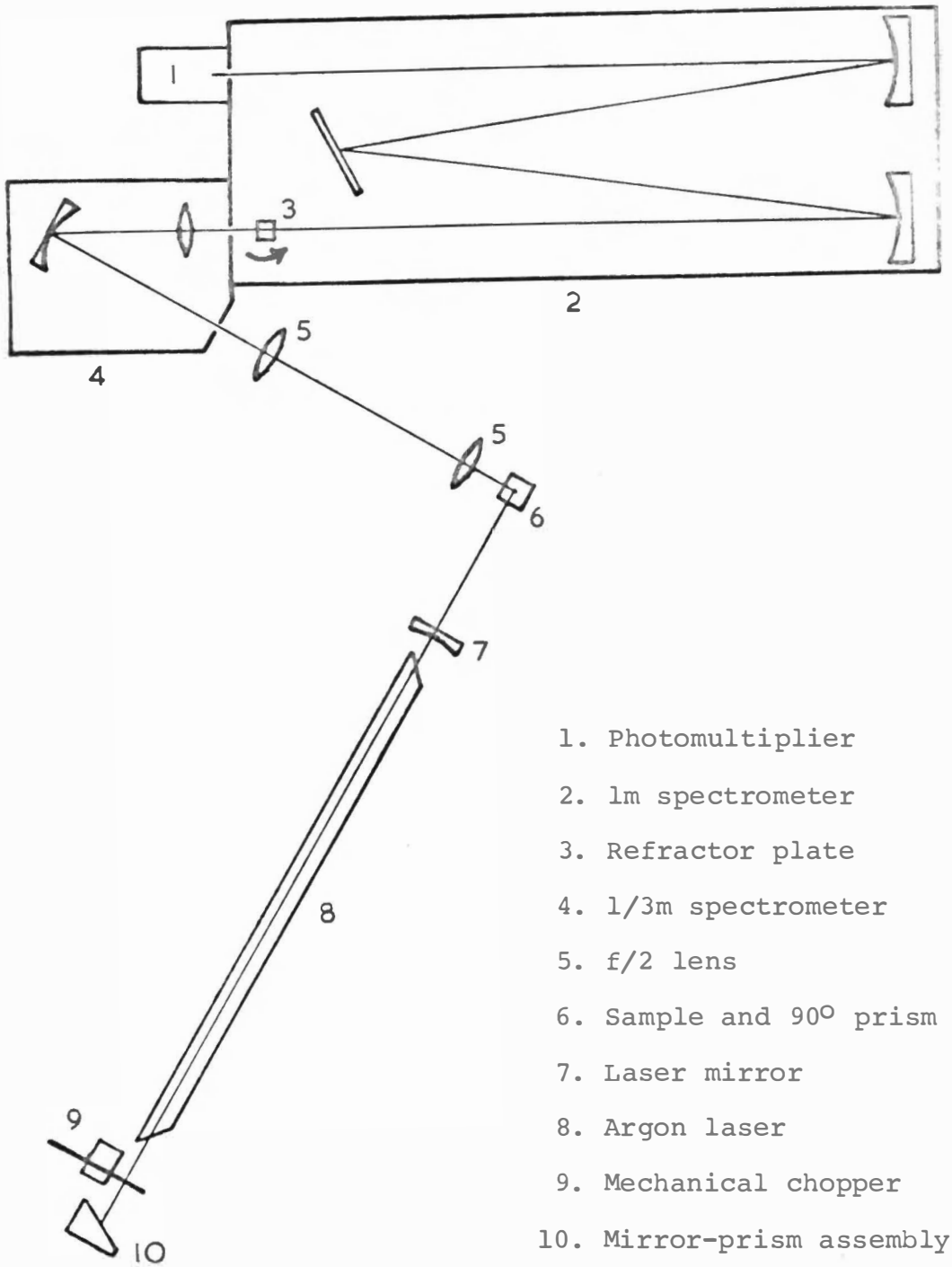

1. Photomultiplier
2. 1m spectrometer
3. Refractor plate
4. 1/3m spectrometer
5. f/2 lens
6. Sample and 90° prism
7. Laser mirror
8. Argon laser
9. Mechanical chopper
10. Mirror-prism assembly.

Fig. 2.6. Plan view of the Raman spectrometer.

Fig. 2.7. The Raman Spectrometer

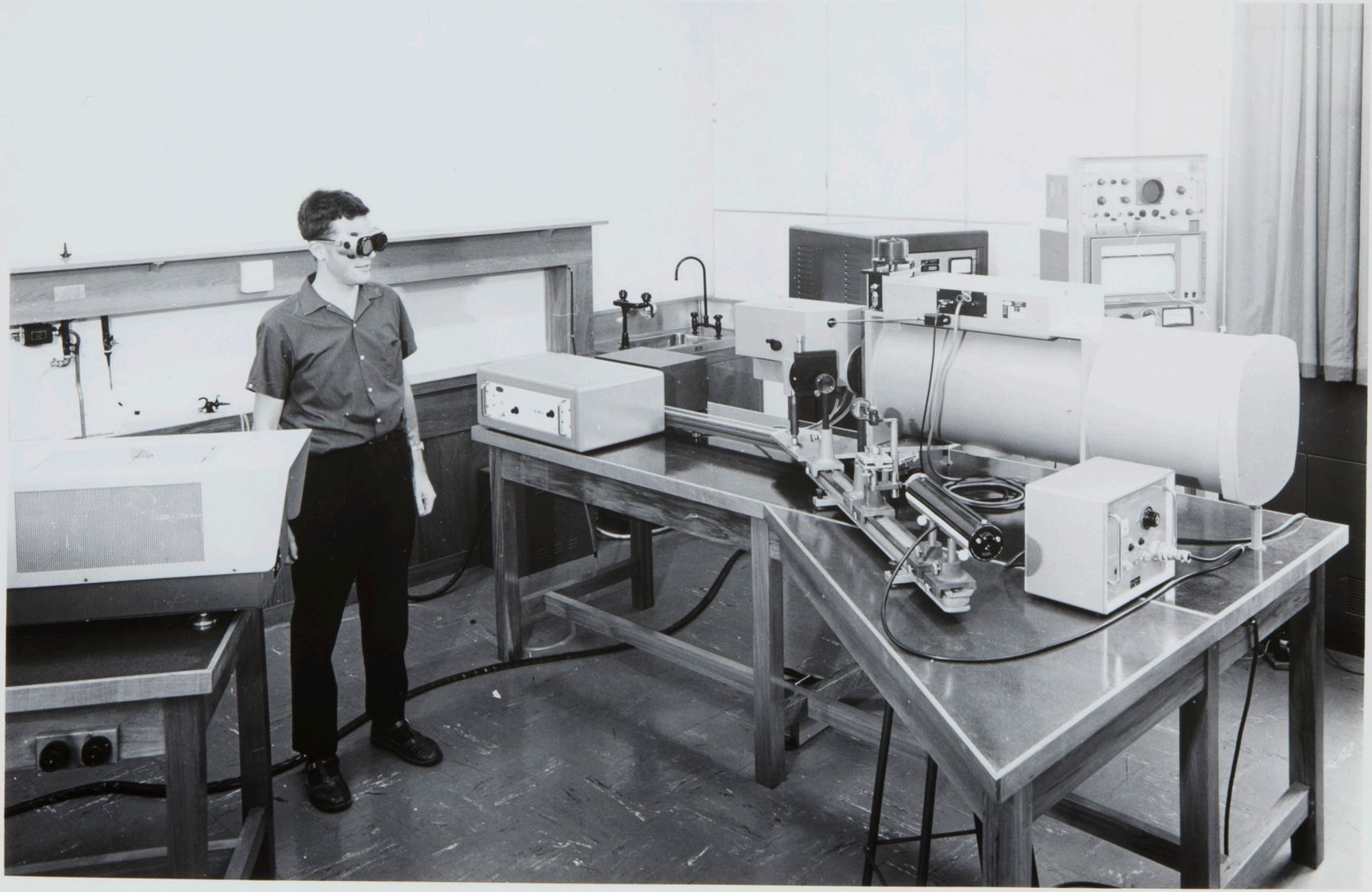

Fig. 2.8. The Electronics

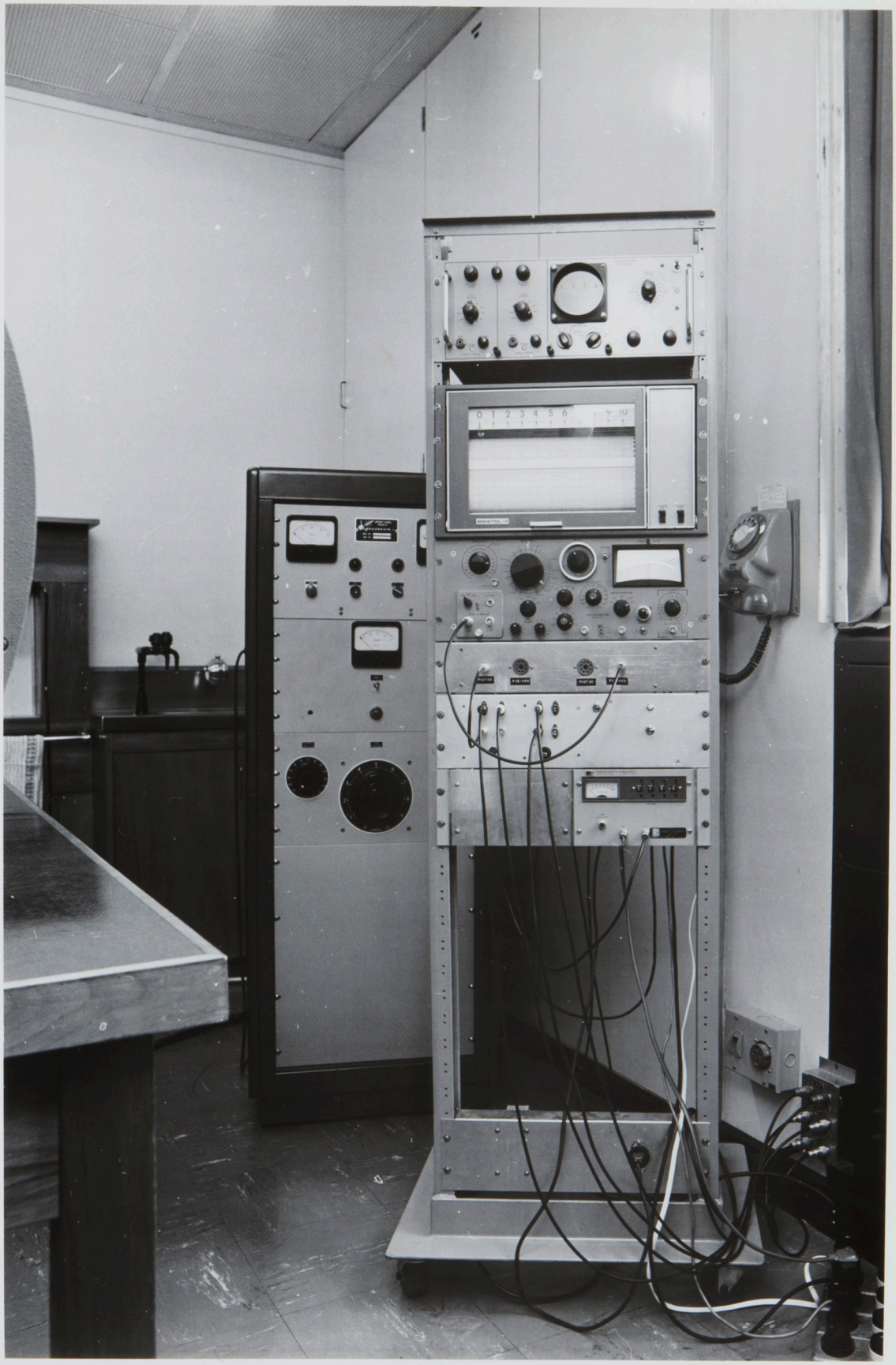

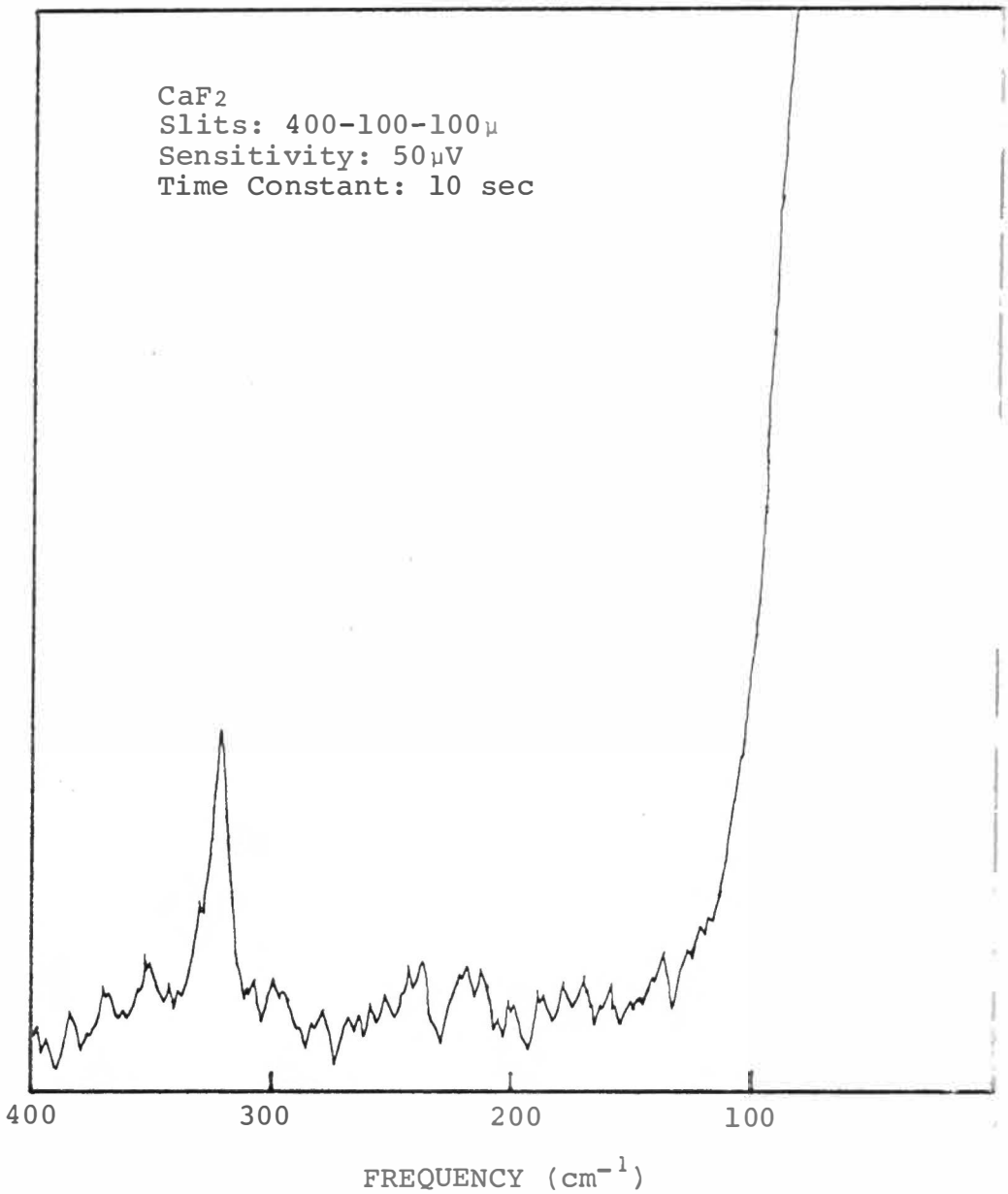

Fig. 2.9. Raman spectrum of CaF_2 at room temperature.

intensity is relatively low as evidenced by the HR-8 gain setting of 50 μV. Faults in this spectrum serve to point out the major faults in the system. Firstly, the exciting light blocks out the spectrum below 100 cm^{-1}; and secondly, some of the peaks in the background noise correspond to argon gas discharge lines.

The first fault is the result of grating tracking errors. The 1 m drive screw has a periodic error which produces a sinusoidal shift in wavelength (about the true position) of 5Å peak-to-peak amplitude. The 100Å period corresponds exactly to one revolution of the main drive screw. With the 1/3 m in place, a continuous tungsten-lamp spectrum shows an intensity modulation which exactly corresponds to this difference in tracking. In setting up the spectrometer the grating drives were adjusted to minimise this effect in the 5000Å region. However, complete elimination of the tracking error only occurs for 1/3 m slit widths $\geq$ 400 μ. Widening the 1/3 m slits immediately increases the stray light intensity, and the consequences can be seen in Fig. 2.9. The sharp change in the stray light level at ~ 100 cm^{-1} can be interpreted as the point at which the 1/3 m image of the laser line no longer overlaps the 1 m entrance slit.

The tracking fault could be corrected by installing a more accurate drive screw. Jarrell-Ash, when questioned about this, accepted responsibility for the fault and decided that rather than change drive screws they would prefer to exchange the spectrometer for one of their new double 1 m systems. This has been done, and we are currently installing a new model 25-103 double monochromator. The instrument consists of two 1 m Czerny-Turner monochromators stacked one on top of the other. The gratings share a common pivot and drive screw, an arrangement that has eliminated tracking problems right down to 10 μ slit widths. The machine is especially designed for Raman scattering work, being equipped with a cosecant drive and interferometrically ruled 1180 grooves/mm gratings blazed for 5000Å.

The second fault is not serious, but could prove troublesome when trying to find weak Raman lines. Obviously the use of a light chopper inside the laser cavity does not sufficiently reduce the intensity of Rayleigh scattered gas discharge lines. Narrow-band interference filters at the laser wavelengths can be used to further descriminate against the gas discharge lines. Suitable filters with narrow passbands at

either 4880Å or 5145 Å have recently been purchased. Other techniques dealing with this problem are outlined in Spex "Ramalogs" 1, No. 3, Dec. 1968 and 2, No. 1, Feb. 1969.

C H A P T E R 3

DATA PROCESSING BY COMPUTER

Powerful computer techniques are increasingly being applied to problems in spectroscopy. Off-line computers enable numerous manipulations to be performed on spectroscopic data. Many calculations are of a routine nature, while others are impossible to perform without a computer. The use of on-line computers to control experiments and present data in a suitable format is even more valuable.[59]

In our laboratory, both on-line and off-line computers are being used to process Raman spectral data. A DEC PDP-8 computer (see Fig. 3.1) is used on-line as an active information processor which can operate in three distinct modes under program control. In each mode of operation the computer performs a function that could be carried out by an independent set of conventional electronic equipment. The advantage is that one instrument performs the work of many, and each function can by easily modified by rewriting the control program. The modes of operation are (1) digitise, (2) photon-count, and (3) signal-average. Each of these modes will be described in detail presently. Spectral information

Fig. 3.1. The PDP-8 Computer


DIGITAL EQUIPMENT CORPORATION
PDP-8

obtained from the on-line computer is further processed with the aid of an IBM 360/44 computer to yield corrected Raman spectra. Examples will be given to demonstrate the usefulness of the off-line computer in this respect.

3.1 Digitise

In the digitise mode, the computer converts the analogue signal from the HR-8 into digital form and punches the result on paper tape. Wavelength information is also recorded.

The experimental arrangement is outlined in the block diagram of Fig. 3.2. Signals from the HR-8 are fed into the computer via its analogue-to-digital converter (ADC). Spectrometer wavelength markers are processed by means of the computer skip line facility.[60] The closing of a relay contact within the spectrometer produces a 6412-code pulse via the line-driver electronics given in Fig. 3.2. The computer recognises the 6412 pulse as a marker event, and encodes the information on the output tape. A remote control switch is used to start or stop the computer, because the PDP-8 is some distance away from the Raman spectrometer. The switch circuit (see Fig. 3.2) operates through the skip

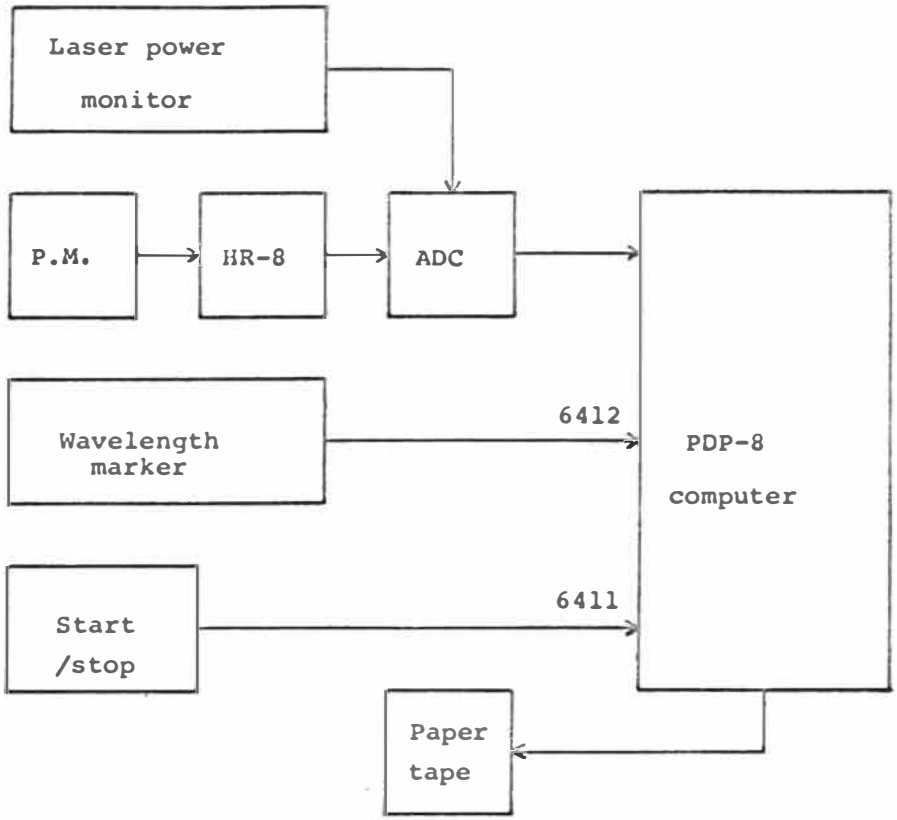

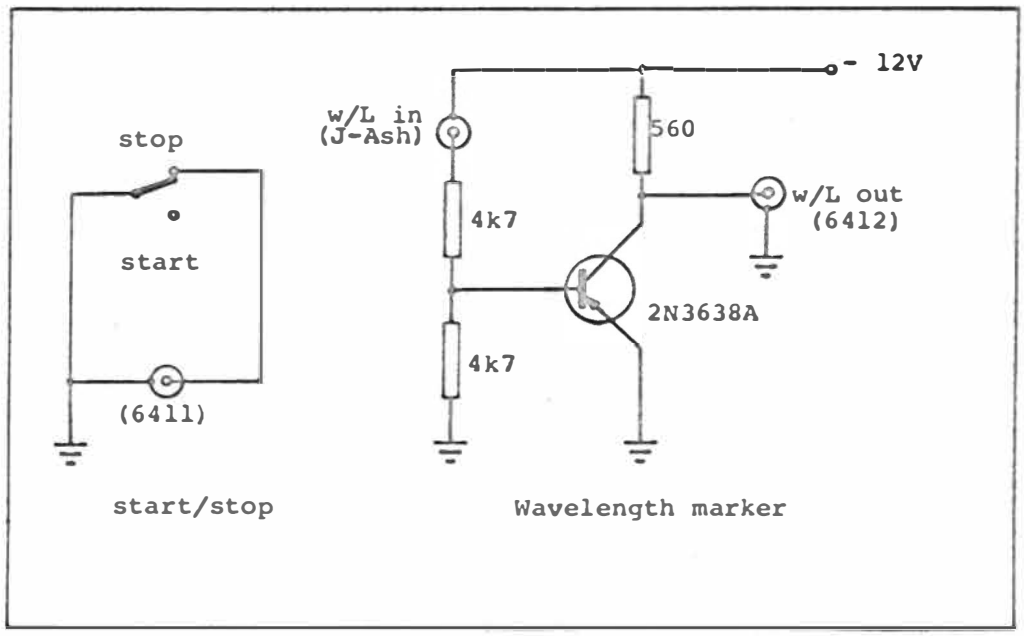

Fig. 3.2. Diagram of the "DIGITISE" apparatus and associated circuits.

line. The digitise control program is fully described in the Appendix.

A low speed paper tape punch (10 characters/sec) limits the output data rate to approximately one point every 0.2 sec. If the full 0.1Å spectrometer resolution is required, the maximum scan speed is therefore

$$\frac{\text{bandpass}}{\text{response time}} = \frac{0.1\text{Å}}{4 \times 0.2 \text{ sec}} = 7.5 \text{ Å/min}.$$

The scan speed determines the HR-8 time constant which in turn determines the signal-to-noise ratio.

The ADC unit has provision for a multiplexer which would enable laser power information to be fed to the computer. The Raman spectrum could then be corrected for variations in the source intensity by performing a simple ratio calculation in the computer.

3.2 Photon-Count

In the photon-count mode, the computer counts photomultiplier pulses for fixed time intervals while the spectrum is scanned, and punches the totals on paper tape. Wavelength information is recorded as in the digitise program. The total count is also produced as an analogue signal for chart recording purposes.

The experimental arrangement is outlined in Fig. 3.3. All input information in processed by means of the program interrupt facility.[60] The photomultiplier pulses are conditioned by the photon counting electronics before being fed to the computer. A crystal controlled clock provides timing pulses at the rate of 1/sec. These pulses are used in determining the integration time as defined by program control (see the Appendix). The wavelength marker and start-stop controls are the same as those described earlier. Again there is provision for laser power monitoring. The output signal is passed through one of the computer's digital-to-analogue converters (DAC) before being chart recorded.

The photon-counting section of the program has a cycle time of 15 μsec, which implies a maximum linear count rate of ~ 6 k counts/sec. This is compatible with the frequency response of the photon counting electronics. If necessary, the count rate can be speeded up by using the computer data break facility[60] which has a 1.5 μsec cycle time. At present the total count is limited to one computer word (4096). This can be expanded to 4096^2 by modifying the control program, but the frequency response will drop. The integration time determines the maximum spectrum scan speed. For the usual 10 sec integration time the maximum scan speed is 0.15Å/min

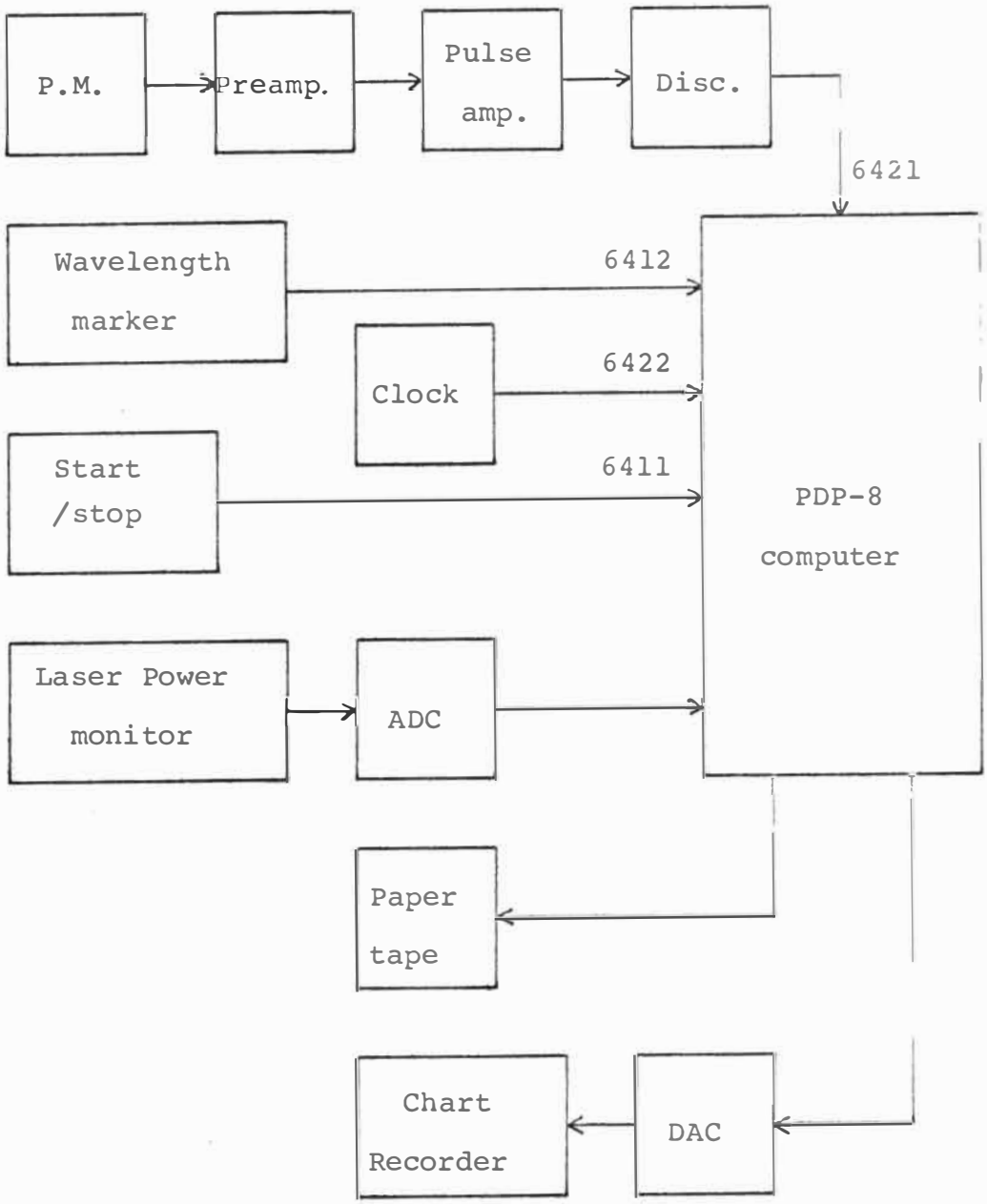

Fig. 3.3. Block diagram of the "PHOTON-COUNT" apparatus.

for 0.1Å resolution.

3.3 Signal-Average

By repeatedly scanning a spectrum and adding the results it is possible to improve the signal-to-noise ratio (S/N). The signal increases in strength in direct proportion to the number of scans n, whereas the noise increase as $\sqrt{n}$. In theory, the S/N can be improved without limit, provided the noise is completely random. Non-random noise can also be reduced if it is not synchronized with the scan repetition rate. However, the S/N will not improve as rapidly as for random noise.

Signal averaging possesses several advantages over conventional integrating techniques. It has been shown[61] that the performance of photoelectric detection used in a time-integrating manner is comparable with or even better than the traditional photographic plate. Moreover, the photoelectric response is linear and does not involve the uncertainties associated with the development of photographic plates. Reference 61 also demonstrates that the averaging technique permits photoelectric detection of weak lines which otherwise could not be detected photoelectrically. This latter

advantage results from practical limitations on the RC integrating time-constant of conventional detection systems.

The signal averaging technique is extensively used in research fields such as X-ray, NMR, Mössbauer and Brillouin spectroscopy.[62] In optical spectroscopy, the usual technique is to scan through a part of the spectrum in the normal manner by rotating the grating or prism; to repeat the process several times; and then average the spectra.[63] It is much simpler to keep the dispersive element stationary and scan the spectrum via a rotating refractor plate. In this arrangement a parallel plate of transparent refractive material is placed behind the entrance slit of the spectrometer, and the plate is rotated about an axis parallel to the length of the slit (see fig. 2.6). The spectrometer experiences at the focal curve a translation of wavelength proportional to the sine of the angle of rotation ϕ. The magnitude of the displacement is proportional to the thickness of the plate and the refractive index at any specific wavelength. In practice, the refractor plate will function only over a relatively small angular change near normal incidence so that $\sin \phi \approx \phi$, and the displacement is linear in ϕ. With this arrangement it is possible to average

the spectra while the scanning phase is in progress rather than at the end.[61]

Our scanning system uses the Jarrell-Ash model 82-134/124 rotary refractor plate and control unit. The quartz refractor plate is 1.6 cm thick, which corresponds to a 60Å scan-width at 5000Å in the 1 m spectrometer. The scan is linear in wavelength to within 6%, and the scan speed can be varied from 0-6000 rpm. One revolution of the refractor plate drive shaft corresponds to two spectral scans. Each scan is divided into 512 channels by a Wang model 43-256 digital shaft-position encoder. The encoder is locked onto the main drive shaft so that the refractor position (and hence wavelength) is always related to a definite channel number. Successive sweeps are synchronized by a start-scan pulse produced by another shaft-locked unit in the Jarrell-Ash 82-134 assembly. The refractor plate assembly (with the Wang encoder mounted on top) can be seen installed in the spectrometer in the photograph Fig. 3.5.

The repetitively scanned spectra are integrated by the PDP-8 computer operating in the signal-average mode. The experimental arrangement is given in Fig. 3.4. The photomultiplier signal and wavelength information are processed by the data break facility. This

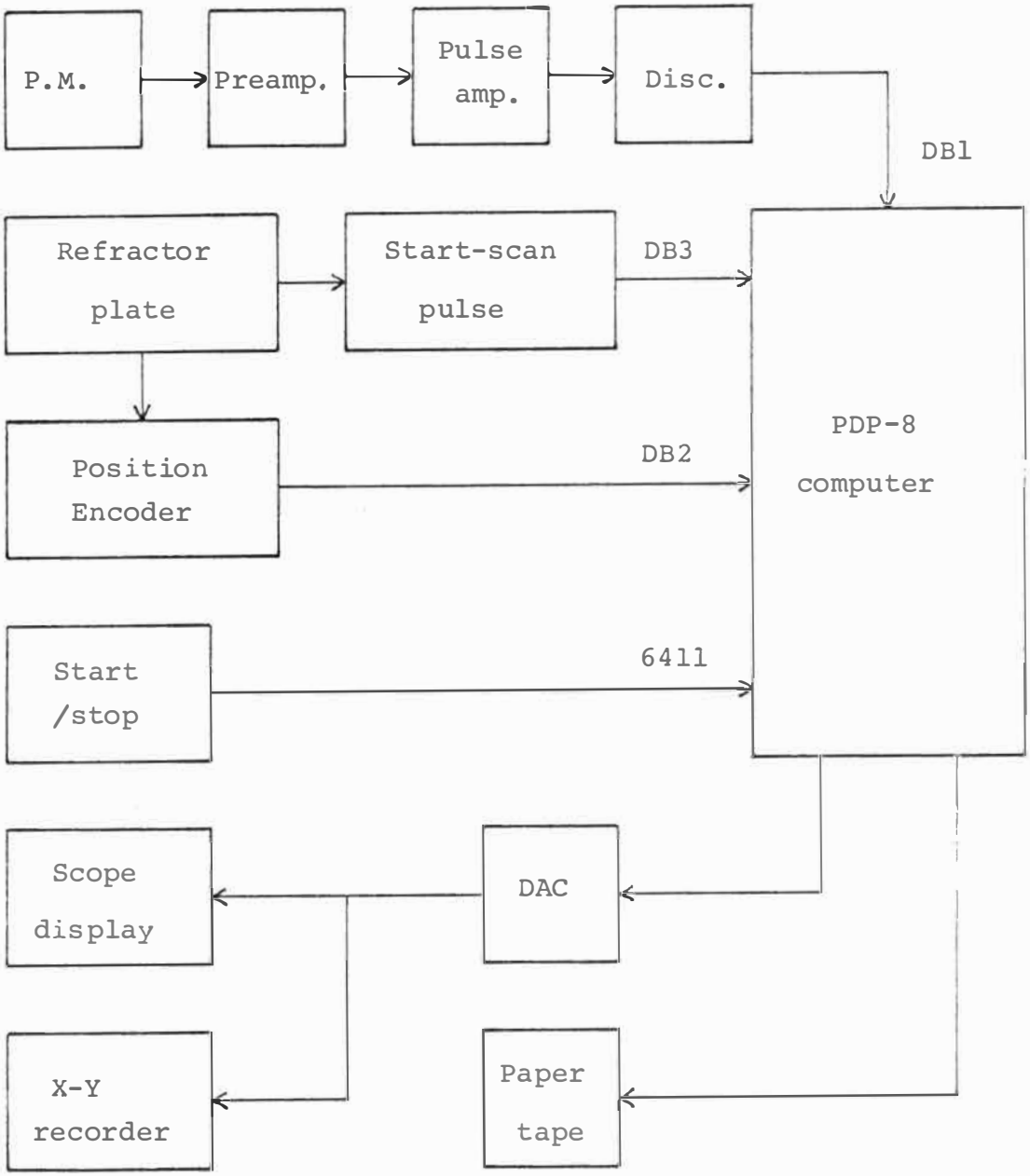

Fig. 3.4. Block diagram of the "SIGNAL-AVERAGE" apparatus.

Fig. 3.5. The Jarrell-Ash Spectrometer

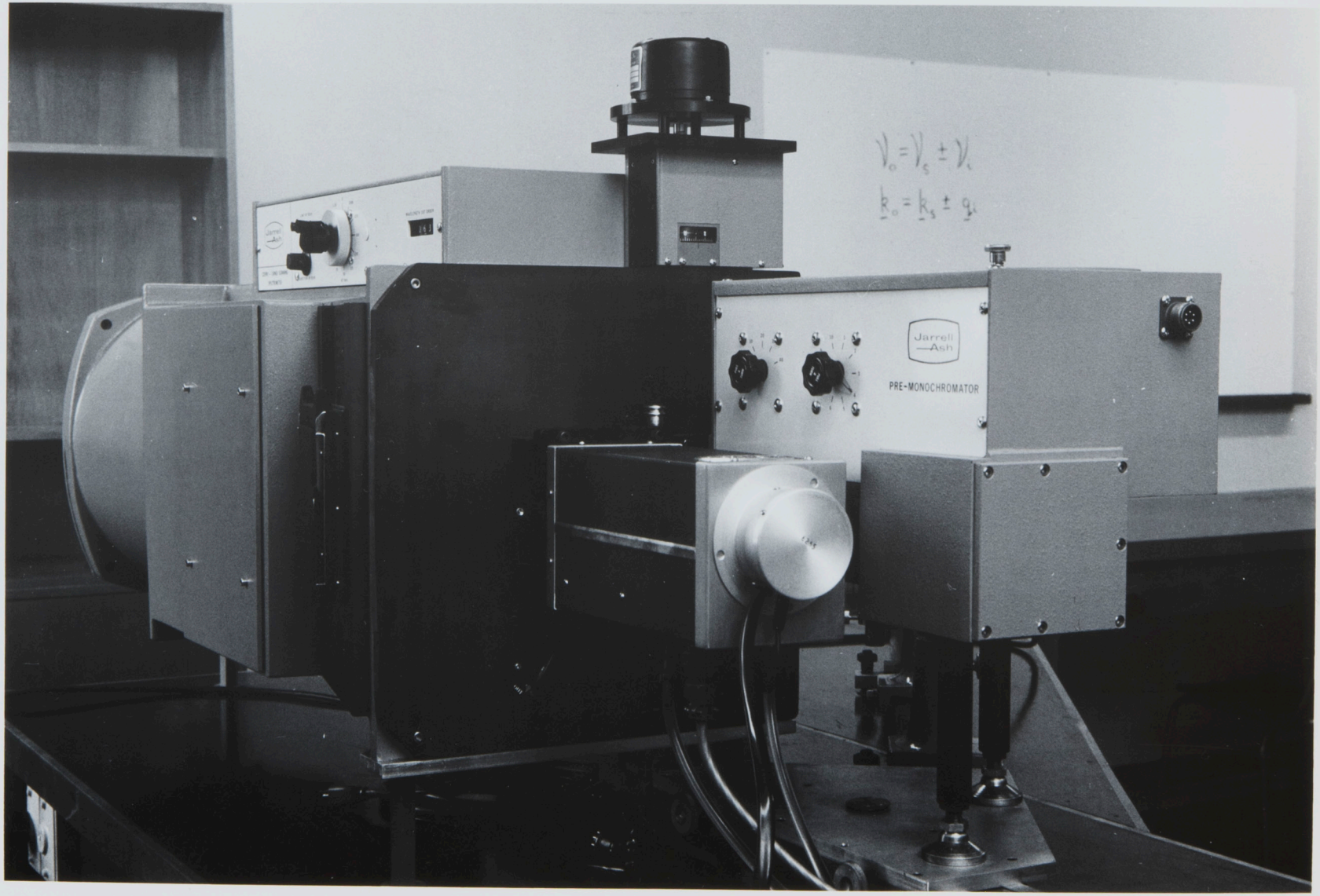
Jarrell Ash
PRE-MONOCHROMATOR

facility operates entirely through hardware, and so is independent of the control program (see the Appendix, section A.3). Starting at channel zero, the computer adds up the number of photomultiplier pulses received (DB1) by counting them into a switch-specified location in the computer's memory. On receipt of a channel increment pulse (DB2) the computer adds the signal pulses into the next consecutive memory location. This latter process is repeated until a start-scan pulse (DB3) is received, at which time the computer returns to the memory address corresponding to channel zero. In this way the computer integrates the spectrum by automatically adding the signal pulses from each successive sweep. A remote stop-start switch is used to halt the computer at the end of a run. Throughout the run the computer produces an oscilloscope display of the integrated spectrum so that the improvement in the S/N can be observed. At the conclusion of the run the computer punches the spectral information on paper tape. If a suitable X-Y recorder were available, the final result could also be displayed graphically.

All data break signals require some conditioning before being fed to the computer. The photomultiplier

pulses are passed through the photon counting electronics described earlier. The start-scan pulse from the 83-134 refractor unit is fed into a variable delay circuit in the 83-124 control unit. This time delay section is used to position spectral features in the centre of the sweep. The trailing edge of the delay output pulse, which represents the end of the delay period, is used to trigger a one-shot multivibrator (see fig. 3.6). The monostable output pulse is about 2 μsec wide, and has a sufficiently fast rise time to trigger the data break circuitry. A 2N3643 line-driver stage isolates the μL914 dual-gate monostable from the computer. The Wang encoder pulses required considerable modification before being delivered to the computer as channel increment pulses. The Wang output is a 256 cycles/rev. rounded square wave. The higher the scan speed the more rounded the output becomes, because of the low frequency response of photodiodes used in the encoder circuitry. Two such square waves are produced with a 90° phase difference. The leading and trailing edges of the square waves are used to determine the 1024 channels/rev. First of all the leading and trailing edges are sharpened by a squaring circuit using three BC177 transistors (see Fig. 3.6). The square waves

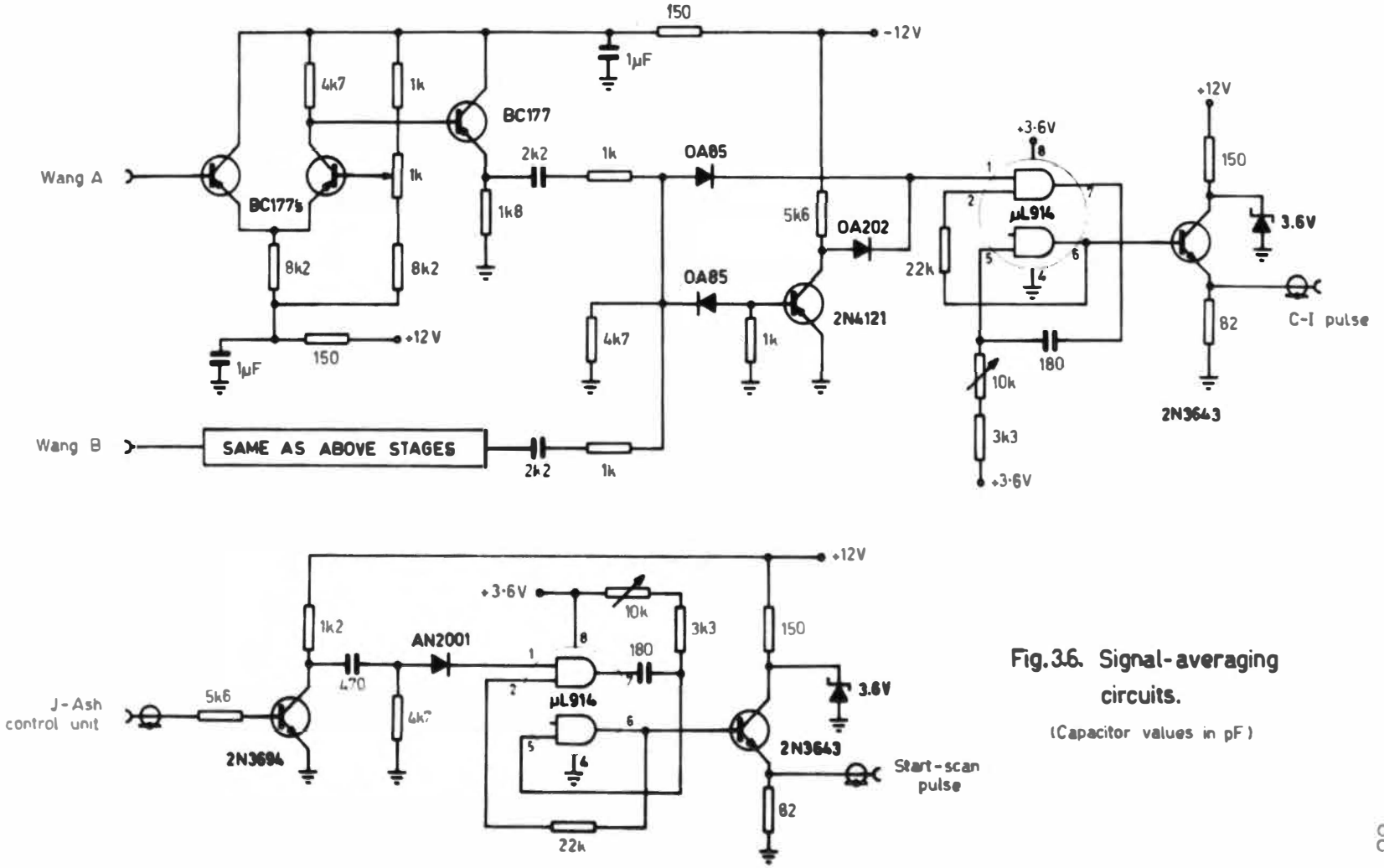

Fig. 3.6. Signal-averaging circuits.

(Capacitor values in pF)

are then differentiated, and the negative going pulses inverted and combined with the positive pulse to produce the channel increment pulses. Again a μL914 one-shot multivibrator stage is used to provide a suitable driving pulse.

The refractor drive speed was set at 150 rpm so as to give ~ 5 scans/sec. At this scan rate of 2560 channels/sec the sampling theorem says that no information is lost provided that the highest frequency present in the signal is not greater than 1280 counts/sec. As most weak Raman lines peak at count rates less than 200 counts/sec, higher scan speeds are not necessary. When setting up the phase controls on the Wang encoder it was noticed that there could be up to 20% jitter in the channel width. This is caused by fluctuations in the motor drive speed, and appears to be random. Proof of this was found by signal averaging a random signal such as the photomultiplier dark current. No consistent features were evident.

The maximum linear signal count rate is limited to about 60 k counts/sec by the 1.5 μsec data break cycle time. The data break operations occur almost instantaneously on request, and are certainly much faster than the present data rates. The maximum

count/channel is 4096^2, as the data break facility automatically deals with word overflow. The computer control program given in the Appendix is designed to handle 4096 counts/channel, but it can be easily extended to the two-word limit.

3.4 Performance Tests

Performance tests of the signal averaging equipment proved it satisfactory in all but one respect. It was found that the spectrometer resolution was drastically affected by the refractor plate. The resolution was not greatly influenced by the digitisation accuracy, as the 512 channel division produced a bandwidth of about 0.3Å.channel. This compares with the spectrometer resolution of 0.1Å. The major factor was the effect of the thick quartz plate on the spectrometer optics. At normal incidence, the plate moves the spectrometer entrance-mirror focus outside the entrance slit by ~ 0.75 cm. This can be corrected by moving the mirror back. (It was not possible to move the entrance slit because of its physical construction.) But this is inconvenient, as the mirror would have to be moved every time the refractor plate was used. The tests were made in the out-of-focus condition. Even

if the focus was correct, the resolution would deteriorate as the refractor plate turns because of the increasing path length inside the quartz plate. For angles of incidence close to zero this effect will be small. The situation would be much worse if the refractor plate was placed behind the exit slit.

Typical signal-averaging results are shown in Fig. 3.7(c) and (d). Mercury gas discharge spectra were recorded with the following spectrometer settings: 1/3 m slit 3000 μ x 5 mm; 1 m slits 20 μ x 5 mm; spectra recorded in the second-order of the 1 m grating; photomultiplier 6255SA (1150 V). The wavelengths of the mercury lines are given in the figure. The Hg lines in Fig. 3.7 (d) show bumps on their sides which are typical of spectra observed in an out-of-focus Czerny-Turner spectrometer. Both runs indicate a resolution of 5Å under these conditions.

The performances of the different signal processing techniques were compared by measuring a very weak signal. The signal was provided by the Rayleigh scattering in methanol of a 0.5 m watt He-Ne laser beam. To make the task even more difficult the 6255SA photomultiplier was used as the detector. This tube has a quantum efficiency of less than 0.2% at 6328Å. The spectrometer was set at 6328Å with slit

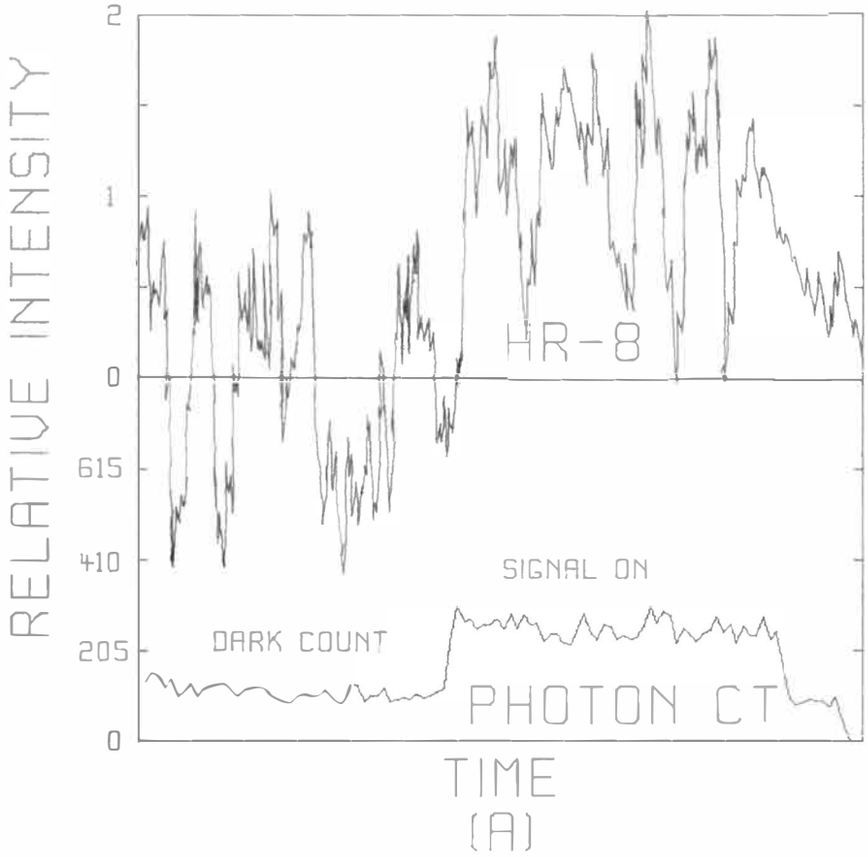

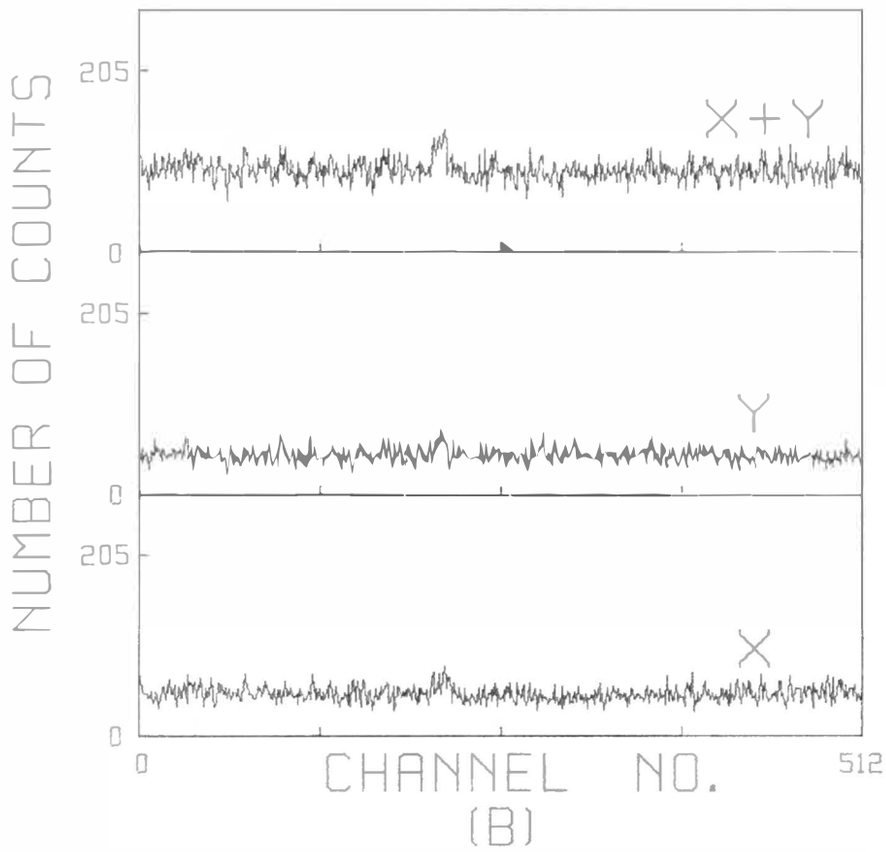

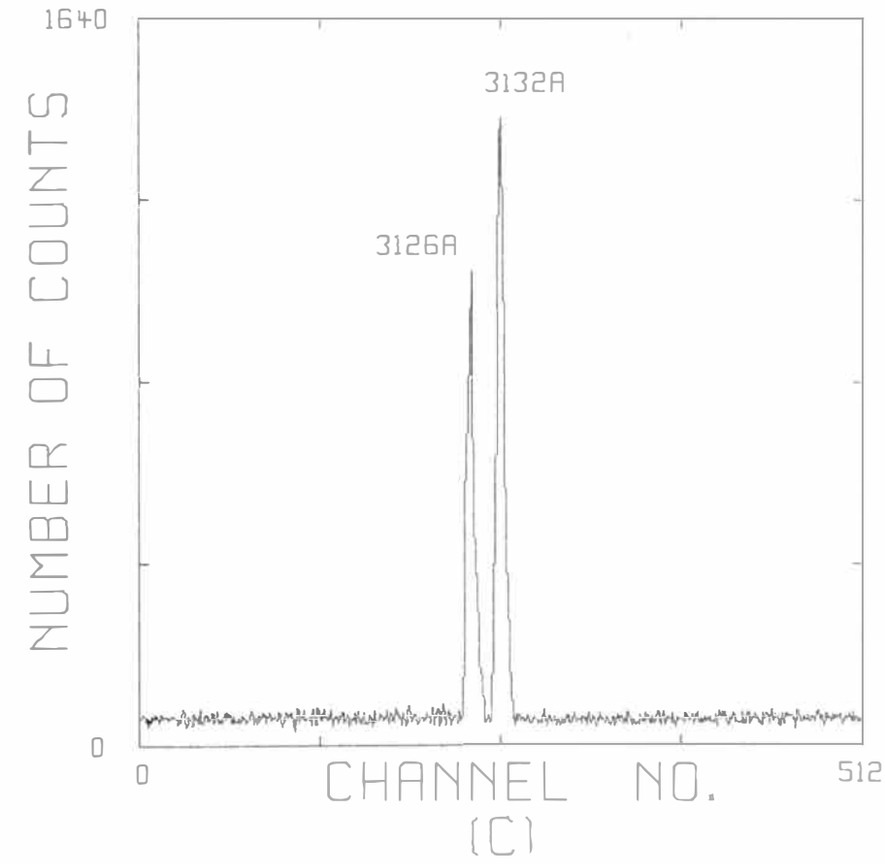

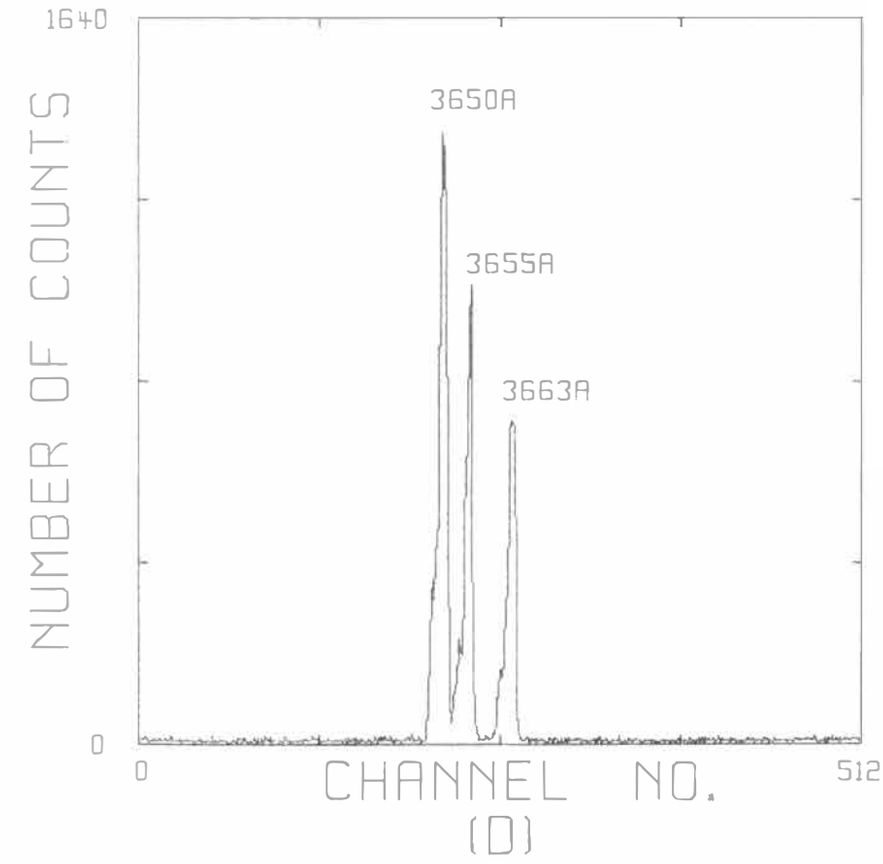

FIG. 3.7. PERFORMANCE TESTS OF THE DIFFERENT SIGNAL PROCESSING TECHNIQUES.

settings of 1000 μ x 5 mm for the 1/3 m and 100 μ x 30 mm for the 1 m. In the case of the HR-8 and photon counting electronics the dark current was recorded first, then the signal, and then the dark current again. The laser power was constant throughout the tests. Typical results are shown in Fig. 3.7(a). The HR-8 system with a gain setting of 2 μ V and a 10 sec time constant produced a S/N of 0.5; while the photon counting system with a 10 sec time constant produced a signal-to-dark count ratio of 2.0 and a S/N of 3.3. The photon-count run shown in the figure lasted 18 mins. Signal-average runs were made under the same conditions. Averaging for 30 mins produced the results X,Y shown in Fig. 3.7(b). The position of the 6328Å line is more clearly seen in the combined result X + Y, which is equivalent to averaging for 60 mins. The S/N has only just reached unity at the end of the 30 min. run. However, it must be remembered that a 60Å section of the spectrum has been integrated. The photon counting electronics would take 60Å/0.15Å/min = 400 mins to cover the same wavelength interval with 0.1Å resolution.

The results indicate that photon counting is superior to the HR-8 at very low light levels. This agrees with our earlier assertion. Signal-averaging

appears to be as good as, if not better than, photon counting. The signal averaging technique would be considerably improved by the use of a thinner refractor plate. This would alleviate the focus problem, and shorten the averaging time by narrowing the scan range. A suitable refractor plate is described by Perregaux and Ascarelli.[64]

Finally, Fig. 3.7 itself is an example of the practical use of off-line computers. The spectral information recorded on paper tape was processed by the IBM 360/44 computer to produce an output that the IBM 1627 plotter used to draw Fig. 3.7.

P A R T I I

THE LATTICE VIBRATIONS OF $CdCl_2$ AND $CdBr_2$

C H A P T E R 4

THEORY

4.1 Introduction

Crystals with the $CdCl_2$ structure after a period of neglect are now being extensively studied. In particular, $CdCl_2$ and $CdBr_2$ are very useful hosts for studying iron group transition metal ions. The crystals are optically clear down to 2800Å, and the crystal field is only a slight trigonal distortion from cubic. Several transition metal chlorides and bromides have the same structure as $CdCl_2$, and thus high doping concentrations of these ions can be achieved. Optical,[65] ESR[66] and Jahn-Teller effect[67] measurements have been reported on transition metal ions doped in $CdCl_2$ and $CdBr_2$ crystals. A knowledge of the lattice vibrations of the host is often necessary in explaining such results.

In this part of the thesis the lattice vibrations of the $CdCl_2$ structure are analysed group theoretically. Later, the theoretical results are used to interpret the Raman and infrared spectra of $CdCl_2$ and $CdBr_2$.

Once the lattice vibrations of the $CdCl_2$ structure are understood, many interesting Raman and infrared experiments become possible. The many crystals isomorphic with $CdCl_2$ [68] make it easy to study the effect of changing the anion or cation. The $CdCl_2$ crystal has a layered structure which involves a mixture of covalent and ionic bonding. It would be of interest to measure the lattice vibrations of mixed crystals such as $Cd_xCo_{1-x}Cl_2$ and $CdCl_{2x}Br_{2(1-x)}$. Mixed covalent-bonded and mixed ionic-bonded crystals have been studied and understood,[69] but as yet no experimental work has been done on mixed-bonding crystals.

The fact that the crystal structure is trigonal is also interesting. There have been few detailed studies of the second-order Raman and infrared spectra of non-cubic crystals. Experimental work is needed to test theory.

The work on $CdCl_2$ naturally leads to a study of the isomorphic transition metal halides. The low lying electronic energy levels can be determined, and magnon spectra can be measured in the antiferromagnetic crystals such as $CoCl_2$, $FeCl_2$, $MnCl_2$, $NiCl_2$ and $NiBr_2$. An attempt to measure the electronic Raman spectra of Fe^{2+} and Co^{2+} in $CdCl_2$ and $CdBr_2$ is reported in Chapter 7.

4.2 Crystal Structure

The $CdCl_2$ structure shown in Fig. 4.1 is trigonal, space group D_{3d}^5, with one molecule to the unit cell.[68] The crystal is made up of layers of chlorine ions which are nearly cubic close-packed, with cadmium ions sandwiched between alternate chlorine layers. The layers are perpendicular to the c axis of the crystal. Each cation is located at the centre of an octahedron consisting of six anions which is compressed along the cubic [111] direction. The smaller cadmium ion fits snugly inside the cage of chlorine ions, as the sum of the cadmium and chlorine ionic radii very nearly equals their separation distance.[68]

4.3 Vibrational Analysis

The fundamental lattice vibrations are analysed using the factor group method.[70-72] This method relies on the fact that at $\underline{k} = 0$ the vibrations of many unit cells will move in phase, and so only one unit cell need be considered. The unit cell modes are classified according to the way in which they transform under the operations of the factor group. The factor group is

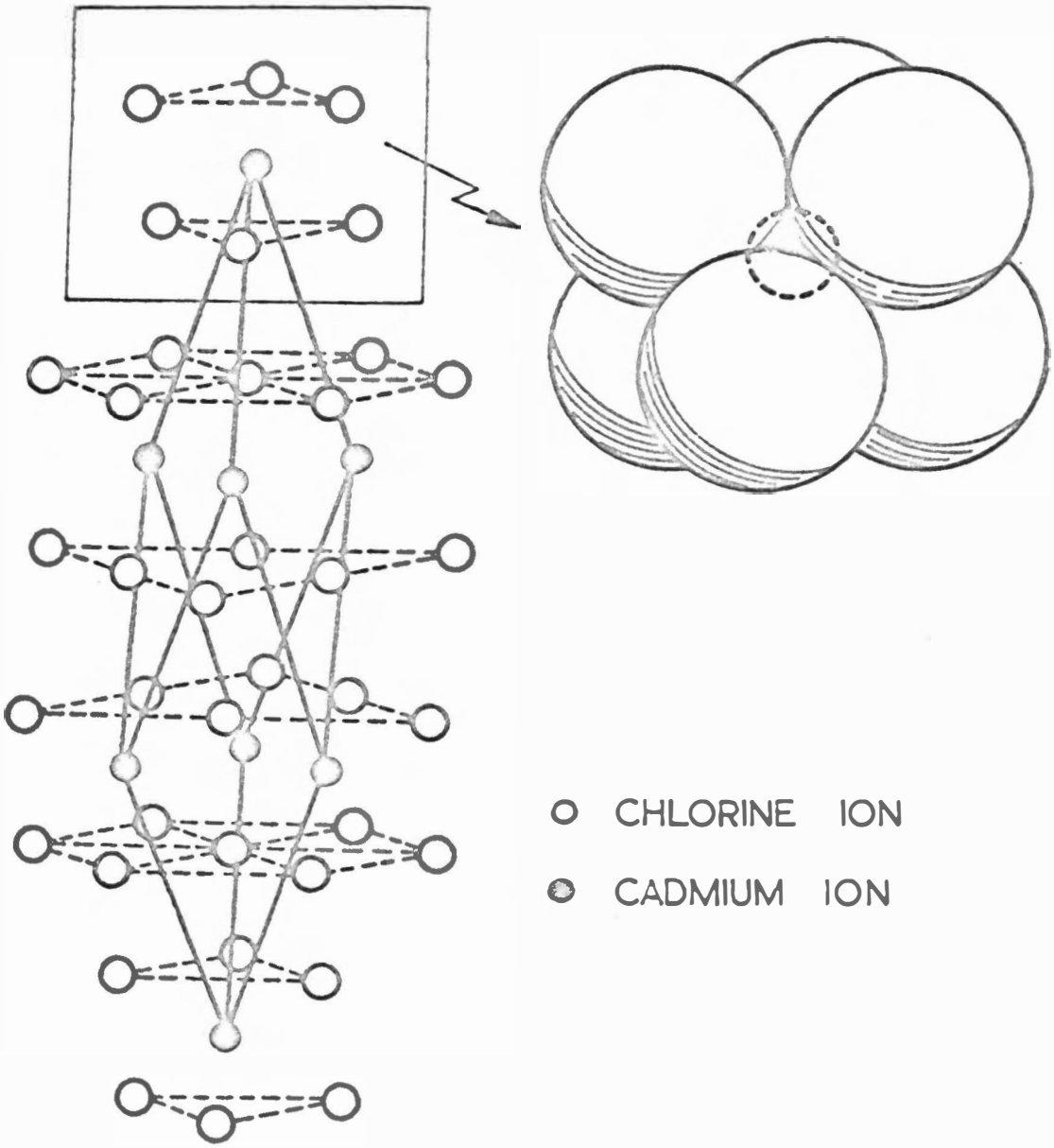

Fig. 4.1. Crystal structure of $CdCl_2$.

obtained from the space group by defining all operations involving the translation part of the space group as the identity operation. The $CdCl_2$ factor group is isomorphous with the D_{3d} point group.

The total number of $\underline{k} = 0$ vibrational modes which can occur in a unit cell is given by[70]

$$\sum_{\Gamma_i} n_i = \frac{1}{N} \sum_{\Gamma_i} \sum_{R} h_\rho \chi_\rho(R) \chi_i(R), \qquad (4.1)$$

where N is the order of the factor group, h_ρ the number of group operations falling under class ρ, $\chi_i(R)$ the character of the group operation R in an irreducible representation Γ_i of the factor group, $\chi_\rho(R)$ the character of the operation for the representation Γ of the displacement coordinates of the atoms in the unit cell, and n_i is the number of times Γ_i is contained in Γ. If n is the number of atoms in the unit cell, then

$$\sum_{\Gamma_i} n_i = 3n.$$

The characters for the reducible representation Γ are obtained from

$$\chi_\rho(R) = U_R(\pm 1 + 2 \cos \phi_R), \qquad (4.2)$$

where U_R is the number of atoms that remain invariant under the operation R, and the plus or minus sign

refers to proper or improper rotations through angle ϕ_R. The n_i obtained by substituting equation (4.2) into equation (4.1) will include all types of normal modes such as translations (T), translatory (T') and rotatory (R') types of external oscillations, and internal oscillations (n_i'). The translation modes correspond to acoustical vibrations, while the rest are optical modes. The general character $\chi_\rho(R)$ can be reduced into components corresponding to the different types of normal modes as follows.

$n_i(T)$ is given by $\chi_\rho(R) = \pm 1 + 2 \cos \phi_R$,

$n_i(T')$ " " " " " $= [U_R(s)-1](\pm 1+2 \cos \phi_R)$,

and

$n_i(R')$ " " " " " $= [U_R(s-v)](1 \pm 2 \cos \phi_R)$,

where s represents the sum of the number of groups of atoms and single atoms occupying non-equivalent lattice points, and v stands for the number of single atoms which occupy such sites. n_i' is given by the difference between n_i and $n_i(T+T'+R')$. Internal and rotatory oscillations will not be present in $CdCl_2$ type crystals because the structure does not involve molecular complexes.

Application of the above formulae to the $CdCl_2$ structure produces the results given in Table 4.1.

Table 4.1 Symmetry analysis of the $\underline{k}$ = 0 vibrational modes in the $CdCl_2$ structure.

Representations of D_{3d}	Character Table E	$2C_3$	$3\sigma_V$	I	$2S_6$	$3C_2'$	Number of Modes n_i	$n_i(T)$	$n_i(T')$	Selection Rules
A_{1g}	1	1	1	1	1	1	1	0	1	Raman
A_{2g}	1	1	-1	1	1	-1	0	0	0	Inactive
E_g	2	-1	0	2	-1	0	1	0	1	Raman
A_{1u}	1	1	1	-1	-1	-1	0	0	0	Inactive
A_{2u}	1	1	-1	-1	-1	1	2	1	1	IR
E_u	2	-1	0	-2	1	0	2	1	1	IR
U_R	3	3	3	1	1	1	The results agree with the conditions that $n_i=n_i(T+T')$, and $\Sigma n_i=3n=9$.			
$\pm 1 + 2\cos\phi_R$	3	0	1	-3	0	-1				

The factor group analysis is made easier by the fact that D_{3d}^5 is a point space group.[73] Because the crystal possesses a centre of inversion, no optical modes of vibration are simultaneously Raman and infrared active. Thus both infrared and Raman measurements are necessary to determine the lattice vibrations. The vibrational analysis indicates that all optical modes are either infrared or Raman active, and hence, in principle, all the fundamental lattice frequencies can be measured directly.

Group theory predicts an infrared spectrum comprising one band with z axis polarization (A_{2u}) and one band polarized in the x,y plane (E_u). The Raman spectrum is expected to consist of two lines, one with A_{1g} symmetry and the other of E_g symmetry. The polarizability tensors for these symmetries have the following form.[22]

$$A_{1g}: \begin{bmatrix} a & 0 & 0 \\ 0 & a & 0 \\ 0 & 0 & b \end{bmatrix}; \quad E_g: \begin{bmatrix} c & 0 & 0 \\ 0 & -c & d \\ 0 & d & 0 \end{bmatrix}, \begin{bmatrix} 0 & -c & -d \\ -c & 0 & 0 \\ -d & 0 & 0 \end{bmatrix}.$$

Simple polarization measurements should provide sufficient information to enable a symmetry assignment of the observed frequencies.

4.4 Symmetry Coordinates

Following Bhagavantam and Venkatarayudu,[70] symmetry coordinates for the predicted lattice vibrations have been constructed. The Cartesian coordinate system was chosen so that the z axis corresponds to the crystal c axis. The choice of the orthogonal x and y axes in the x,y plane is arbitrary. For convenience, we take the x axis to be one of the three twofold axes corresponding to the rotations C_2'. The most general linear expression in the 3n Cartesian coordinates is

$$Q = \sum_{i=1,2,3} (a_i x_i + b_i y_i + c_i z_i). \qquad (4.3)$$

The labels 1, 2 and 3 refer to the two chlorine atoms and the cadmium atom which make up the unit cell. The normal coordinates are derived from the transformation properties of equation (4.3) under the different operations of the group. If R is a group operation and λ is its character under the one-dimensional irreducible representation Γ_i, then

$$RQ = \lambda Q. \qquad (4.4)$$

For two-dimensional representations,

$$RQ_i = \sum_{k=1,2} a_{ik} Q_k, \qquad (4.5)$$

where a_{ik} is the matrix representing R in the irreducible representation Γ_i.

Solving equations (4.4) and (4.5) for the $CdCl_2$ structure we obtain the following symmetry coordinates:

Symmetry Coordinate	D_{3d} Representation
$S_1 = c_1(z_1 - z_2)$	A_{1g}
$S_2 = c_1(z_1 + z_2)$	A_{2u}
$S_3 = c_3 z_3$	
$S_4 = a_1(x_1 - x_2)$	E_g
$S_5 = -a_1(y_1 - y_2)$	
$S_6 = a_1(x_1 + x_2)$	E_u
$S_7 = a_3 x_3$	
$S_8 = -a_1(y_1 + y_2)$	
$S_9 = -a_3 y_3$	

The normal coordinates Q are obtained by forming independent combinations of the symmetry coordinates for each representation. If the number of modes of oscillation coming under Γ_i is one, the normal coordinate is uniquely determined. If n_i is greater than one, Q will involve n_i arbitrary constants. These constants are determined from a knowledge of the forces acting on the point system.

The normal coordinate for the A_{1g} mode is uniquely determined as

$$Q_1 = z_1 - z_2,$$

taking $c_1 = 1$. The two A_{2u} modes have normal coordinates given by

$$Q_{2,3} = c_1(z_1+z_2) + c_3 z_3.$$

From the previous analysis we know that one of the A_{2u} modes is a pure translation. Therefore one normal coordinate is

$$Q_2 = z_1 + z_2 + z_3. \qquad (c_1 = c_3 = 1)$$

The other coordinate must be orthogonal to Q_2, so we take

$$Q_3 = z_1 + z_2 - 2z_3. \qquad (c_1 = 1,\ c_3 = -2)$$

There is only the one E_g mode. The normal coordinates are determined as

$$Q_4 = x_1 - x_2,$$

and $(a_1 = 1)$

$$Q_5 = -(y_1 - y_2),$$

from the orthogonality condition. There are two E_u modes of vibration, so the normal coordinates can not be uniquely determined. However, two of the coordinates

correspond to an acoustic mode. Therefore we must take

$$Q_6 = x_1 + x_2 + x_3,$$

and $(a_1 = a_3 = 1)$

$$Q_7 = -(y_1 + y_2 + y_3).$$

The other two coordinates are given by the orthogonality condition. We choose

$$Q_8 = x_1 + x_2 - 2x_3,$$

and $(a_1 = 1, a_3 = -2)$

$$Q_9 = -(y_1 + y_2 - 2y_3).$$

Coordinates Q_1 - Q_9 are not the true normal coordinates because of the arbitrary disposal of the constants, but they do possess the correct symmetry properties with respect to the displacement coordinates x_i, y_i, z_i.

The symmetry coordinates Q_1, Q_3, Q_4, Q_5, Q_8 and Q_9 are shown pictorially in Fig. 4.2. It is immediately obvious that vibrations along the z axis are completely different from motions in the x,y plane. For example, in the Raman-active A_{1g} mode the planes of cadmium ions remain stationary while the planes of chlorine ions move directly against each other; whereas in the E_g mode the planes of chlorine ions move over each other with a sliding action as though they were acted upon by a shear force. It would be reasonable to expect the A_{ig}

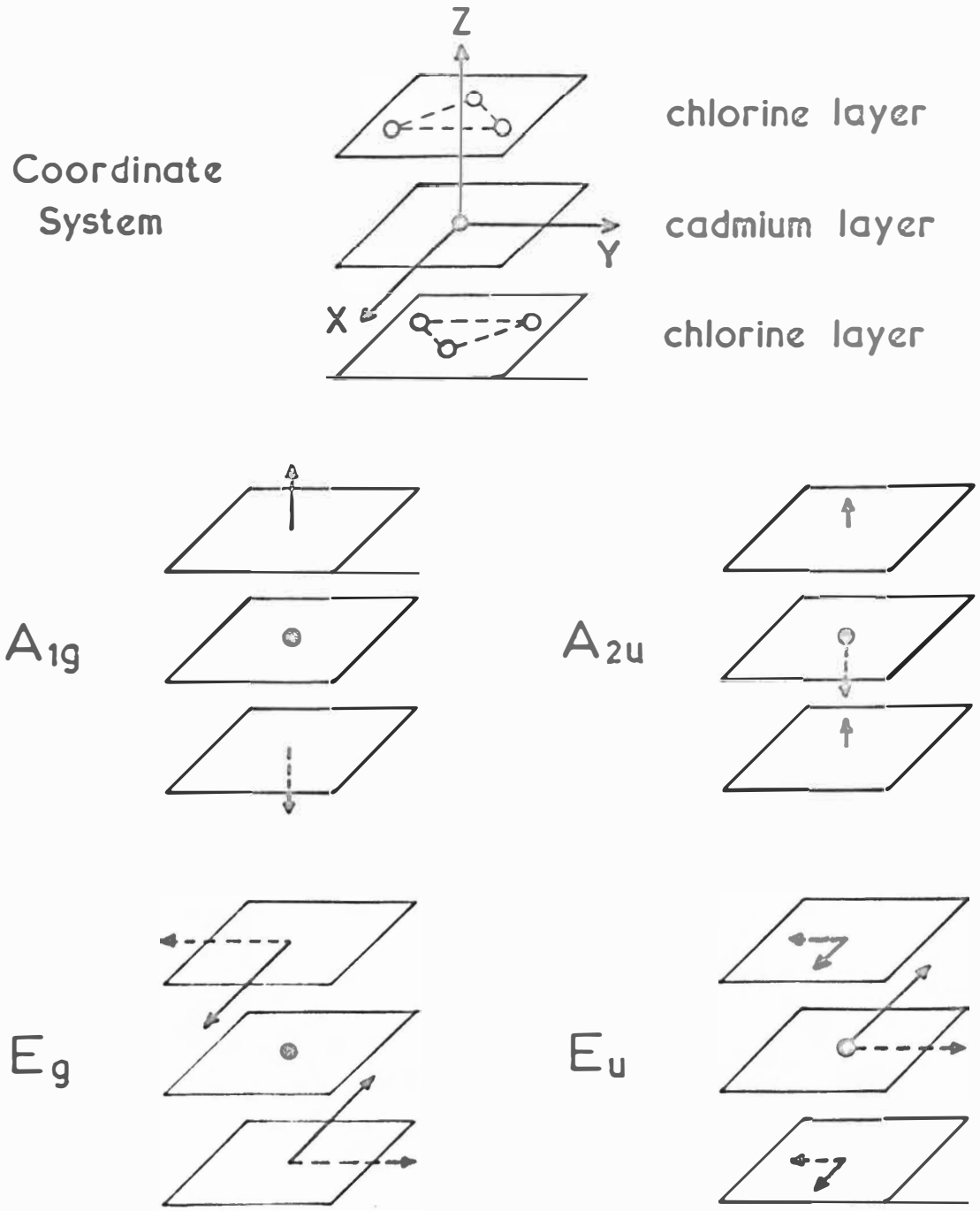

Fig. 4.2. Symmetry coordinates for the optical modes in $CdCl_2$.

mode to have a higher force constant than the E_g mode. The harmonic oscillator model would thus predict that the A_{1g} mode has the higher frequency. As the Raman-active modes do not involve movement of the cations, the Raman frequencies will be independent of the cation to a first approximation. The infrared-active modes involve motion of both cations and anions, so that similar predictions can not be made.

C H A P T E R 5

EXPERIMENT

5.1 Crystal Growth

The $CdCl_2$ and $CdBr_2$ crystals were grown from the melt using the Stockbarger technique.[74] Analar or reagent grade powders of the hydrated salts were used as the starting material. The powders were first dehydrated by heating in vacuum for several days, and then sealed into inert-gas filled glass ampoules. The crystals were grown by slowly lowering the ampoules through a sharp temperature gradient. The full details of the method are given by Freeman.[75]

Crystals of $CdCl_2$ and $CdBr_2$ are deliquescent, the chloride more so than the bromide. To overcome rehydration problems, the ampoules in which the crystals were grown were also used as sample holders for the Raman measurements. This avoided exposing the crystals to atmospheric moisture. The ampoules were formed from 3 mm I.D. glass tubing, with the crystal-growing end flattened to form a window. Several single crystals, each at least 2.5 cm in length, were grown in this manner. The samples used in the infrared measurements

were grown in 10 mm I.D. tubes. Examples of $CdCl_2$ crystals grown in both types of ampoule are shown in Fig. 5.1. The photographic reproduction is very near life size.

The crystal orientation was determined from the direction of the cleavage planes, as the crystals cleave very readily along covalent-bonded chlorine planes perpendicular to the c axis. The c-axis direction varied from crystal to crystal, and was usually inclined to the axis of the sample tube.

5.2 Raman Spectra

The Raman spectra were recorded using the apparatus described in Part I. Plane-polarized 4880Å laser light travelling parallel to the spectrometer entrance slit was directed into the crystal through the window at the bottom of the sample tube. Scattered light was collected at 90° from incidence and focused on the spectrometer entrance slit. In some measurements an analysing polarizer was placed between the sample and the spectrometer. The spectrometer output was detected using the 9558QA photomultiplier, HR-8 lock-in amplifier, and chart recorder.

Fig. 5.1. $CdCl_2$ Crystals

Typical room temperature spectra for $CdCl_2$ and $CdBr_2$ are shown in Fig. 5.2. The spectra were recorded under similar conditions, with a spectral resolution of about 3.5 cm^{-1}. The spectrometer slits were set at 400-100-100μ, and the HR-8 gain and time-constant settings were 500 μV x 1 sec for the bromide and 100 μV x 3 sec for the chloride. As the spectra of Fig. 5.2 indicate, only one Raman line was found in both $CdCl_2$ and $CdBr_2$. The frequencies of the lines are 232.0 ± 1.2 cm^{-1} for the chloride and 147.3 ± 1.0 cm^{-1} for the bromide, with linewidths of about 15 cm^{-1} and 9 cm^{-1} respectively. The $CdBr_2$ line is approximately five times stronger than the $CdCl_2$ line.

In order to facilitate the search for the missing lines, Raman measurements were made on a single crystal of $CdBr_2$ that was not enclosed in glass. The crystal was shaped into a cube of dimension 4 mm on a side, with two opposite faces being cleavage planes perpendicular to the crystal c axis. The other faces were arbitrarily cut at right angles to the x,y plane. Different orientations of the crystal relative to the polarization of the laser light and the scattered light were tried. With the experimental conditions

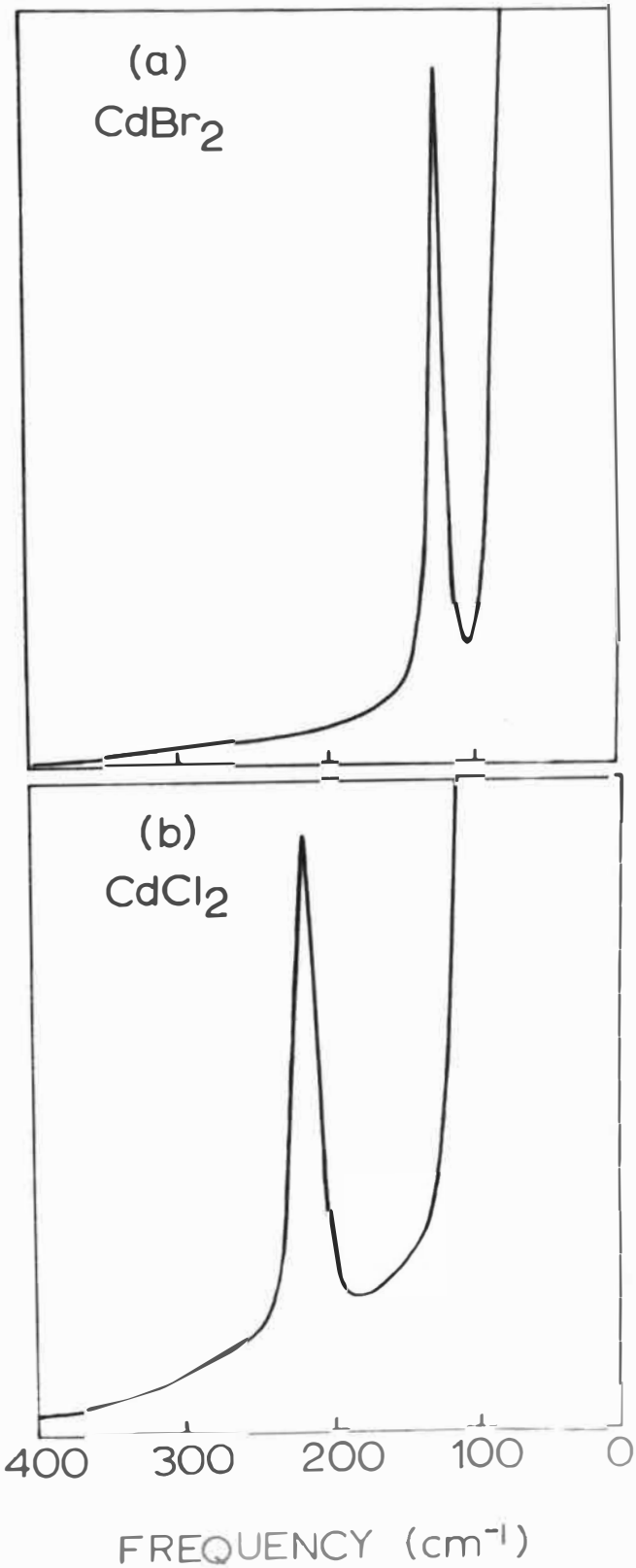

Fig. 5.2. Raman spectrum of (a) $CdBr_2$ and (b) $CdCl_2$ at room temperature.

x(zz)y* and y(xx)z, where, according to the polarizability tensors given earlier, both modes should appear, only the 147 cm^{-1} line was observed. This line was also seen under x(zx)y and y(xy)z conditions at a slightly reduced intensity. Polarization measurements were also made on $CdCl_2$ and $CdBr_2$ crystals in glass, with similar results. The single line observed in each crystal never vanished under any polarization condition , and the diagonal polarizability tensor components were generally stronger than the corresponding off-diagonal elements.

The crystals examined were of indifferent optical quality. Cleavage planes and other crystal-growth imperfections were evident in all the samples (see Fig. 5.1 for example). Because of this, the crystals scattered light by reflection and refraction, and the effect can be seen in Fig. 5.2 where the tail of the exciting line intrudes upon the spectrum. The stray light level should be compared with that obtained in the

---

*The polarization notation of Damen et. al.[76] is used here. The term x(zz)y indicates that the incident light enters the crystal along the x axis, and that the scattered light is observed along the y axis. The symbols in the brackets denote the polarization of the incident and scattered light respectively.

Raman spectrum of the optically clear sample of CaF_2. The CaF_2 spectrum (Fig. 2.9) was recorded with a 10X higher gain setting than the $CdBr_2$ spectrum, and yet the stray light levels are roughly the same. Correspondingly, the background of laser gas discharge lines is also higher at about one-fifteenth the intensity of the $CdCl_2$ Raman line. (The argon plasma lines have not been drawn in Fig. 5.2, as they are similar to those shown in Fig. 2.9) Stray light was the limiting factor in finding the missing Raman lines. All that can be said about these lines is that their frequencies may be less than ~ 120 cm^{-1}, and if not, their intensities must be less than one-fifteenth the intensity of the 232 cm^{-1} line in $CdCl_2$.

5.3 Infrared Spectra

Far infrared absorption spectra were recorded in the range 20 - 400 cm^{-1} using the Chemistry Department's RIIC model FS-720 Fourier transform spectrometer. Some results were checked by Grubb Parsons in England with their IS-3 Fourier transform spectrometer. All runs were made at room temperature on powder samples dispersed in polyethylene. Polyethylene was chosen as the supporting

medium because apart from a narrow line at 70 cm^{-1} it is transparent throughout the spectral region of interest.[77] The samples were prepared by thoroughly mixing dehydrated crystal powder with approximately 3 gm of Microthene 710 polyethylene powder.[78] The mixture was heated in a mould to melt the polyethylene, which, on cooling, formed a solid disc 5 cm in diameter by 1 mm thick. The sample powder was held within the polyethylene matrix virtually free from contamination by atmospheric moisture. Sample concentrations ranged from 1% to 10% by weight.

Typical absorption spectra recorded at 2 cm^{-1} resolution are shown in Fig. 5.3. The fundamental infrared spectrum consists of two broad overlapping bands. These bands are so broad that a spectrometer resolution of 5 cm^{-1} does not appear to affect their shape. Consequently, most runs were made at 5 cm^{-1} resolution. Some of the $CdCl_2$ measurements carried out by Grubb Parsons produced a weak absorption band at 96 cm^{-1}. This feature was not observed in the RIIC spectra, nor could any corresponding absorption be found in $CdBr_2$. It must be assumed that the absorption is due to an impurity in the $CdCl_2$ sample. As mentioned earlier, $CdCl_2$ is much more hygroscopic than $CdBr_2$, and

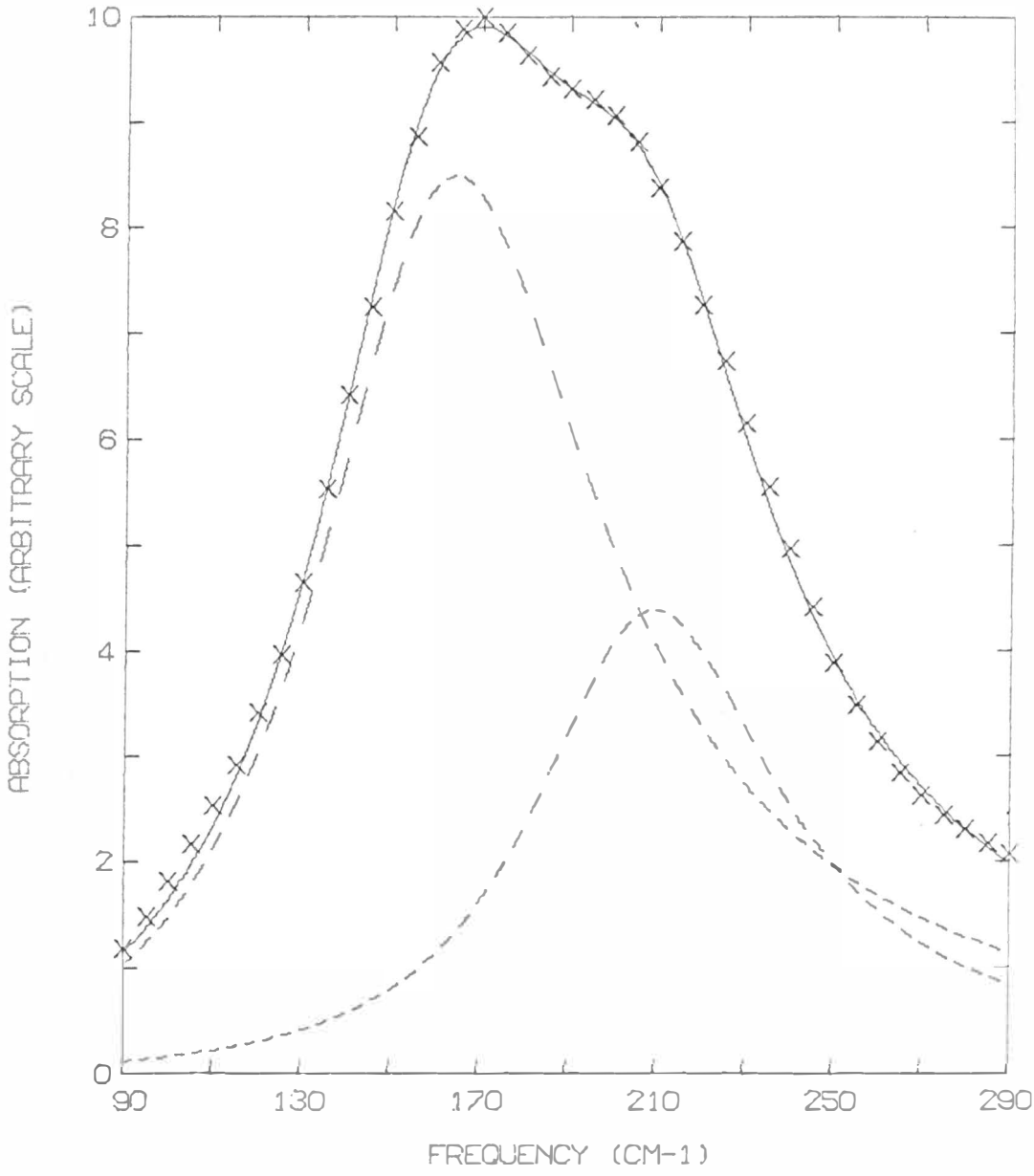

Fig. 5.3(a). Infrared spectrum of powdered $CdCl_2$ at room temperature.

X Experiment

——— Theory

---- Individual Lines

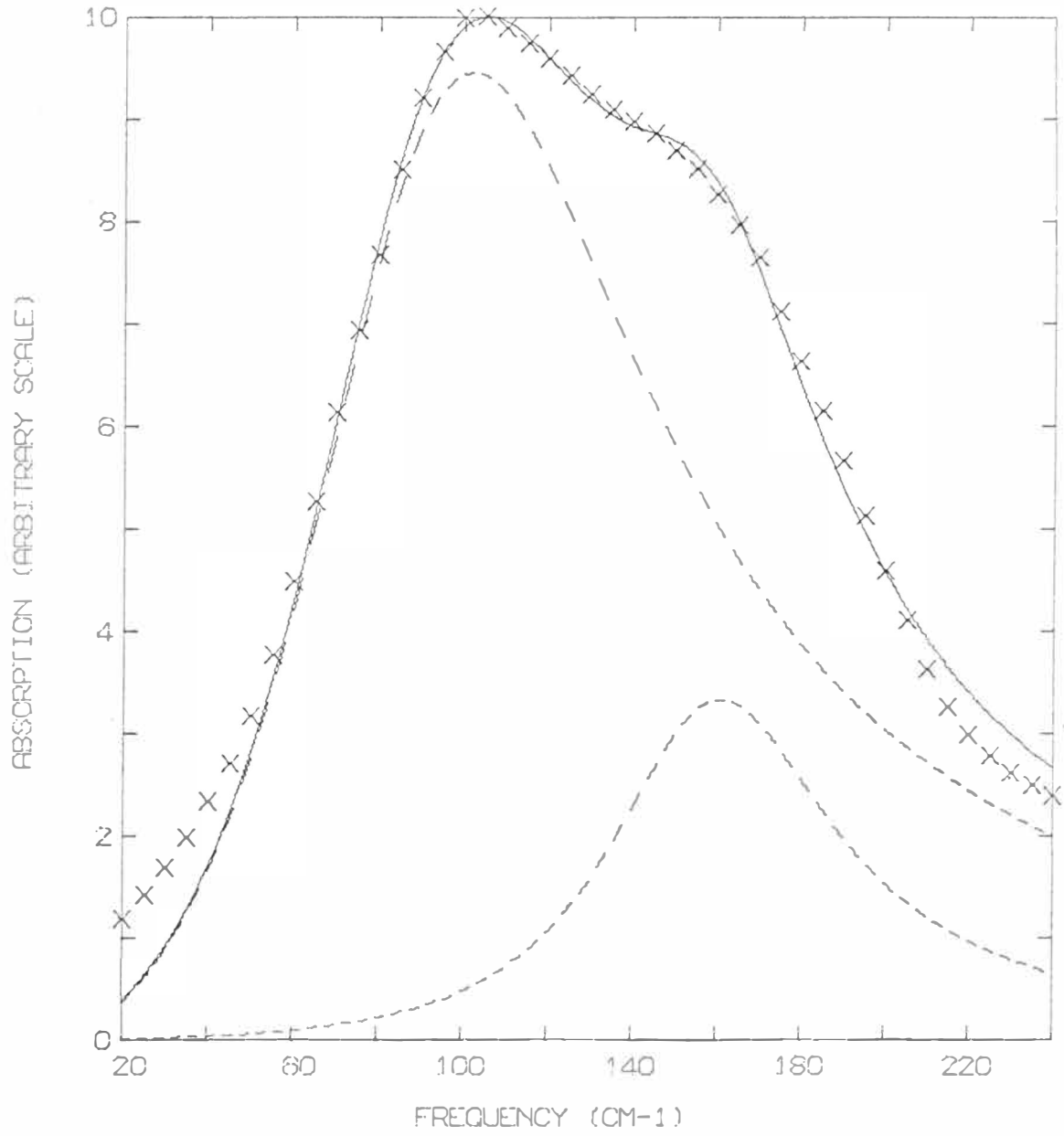

Fig. 5.3(b). Infrared spectrum of powdered $CdBr_2$ at room temperature.

so the $CdCl_2$ samples could have deteriorated on the outside, despite the fact that all samples were airmailed to Grubb Parsons in air-tight packages.

The spectra were analysed using the Lorentz model of absorption and dispersion in insulators.[79] The classical oscillator dispersion parameters are determined from the imaginary part of the complex dielectric constant[80]

$$\varepsilon''(\nu) = \sum_j 4\pi\rho_j\nu_j^2 \frac{\gamma_j\nu}{(\nu_j^2-\nu^2)^2 + \gamma_j^2\nu^2}, \qquad (5.1)$$

where the summation is over the j resonances in the spectrum. Each oscillator is described by its strength ρ_j, width γ_j and frequency ν_j, and is assumed independent of other resonances. The frequency of a given resonance is the frequency at which the conductivity

$$\sigma_j = \varepsilon_j'' \nu/2 \qquad (5.2)$$

is a maximum, where the quantity ε_j'' is the contribution of the jth resonance to ε'' and ν is the frequency of the incident light. The conductivity is related to the absorption coefficient η by[79]

$$\eta = 4\pi\sigma_j/c, \qquad (5.3)$$

where c is the velocity of light. From equations (5.1),

(5.2) and (5.3) it can be seen that the absorption line shape is determined by the asymmetric function

$$F = \frac{\nu^2}{(\nu_j^2-\nu^2)^2+\gamma_j^2\nu^2} . \qquad (5.4)$$

This formula is essentially the same as that derived using quantum mechanics, except that γ is a function of frequency ν in the quantum theory.[81]

The dispersion analysis is carried out by fitting the absorption spectrum to a set of oscillators of line shape and strength defined by equations (5.1) - (5.3). The actual function used here was

$$F(\nu) = \sum_{j=1,2} \frac{k_j\nu^2}{(\nu_j^2-\nu^2)^2+\gamma_j^2\nu^2} + C . \qquad (5.5)$$

The $CdCl_2$ and $CdBr_2$ infrared spectra were first analysed by the wing-folding technique to obtain values for the parameters ν_1,γ_1,k_1 and ν_2,γ_2,k_2. The wing-folding technique involves choosing a reasonable value for ν_1, reflecting the free outer line shape about frequency ν_1, and subtracting the symmetric line ν_1 from the combined spectrum to reveal the line of frequency ν_2. The parameter values thus obtained were then used as initial values for a least squares fit if equation (5.5) to the observed spectrum. The least-squares fitting was

carried out in the IBM 360/44 computer using a general program (ORGLS) based on a Taylor expansion of the fitting function. The experimental data was weighted for accuracy.

The values obtained for the computer calculated parameters are as follows:

	Parameters (ν and γ in cm^{-1})					
Crystal	ν_1	γ_1	k_1	ν_2	γ_2	k_2
$CdBr_2$	102.1	101.7	10.4	161.0	65.0	1.50
$CdCl_2$	164.2	77.8	3.77	209.6	67.1	1.45

The closeness of the least-squares fit can be seen in Fig. 5.3. The overall fit is very good, especially in the case of $CdCl_2$. The data in the wings of the absorption carried the least weight, and so the fit here is not as good as elsewhere. The estimated uncertainties in the calculated results are given in Table 5.1.

Table 5.1 Room temperature first-order infrared lines. The frequencies ν and linewidths γ are given in cm^{-1}.

Crystal	ν_1	γ_1	ν_2	γ_2
$CdBr_2$	102 ± 2	102 ± 10	161 ± 2	65 ± 5
$CdCl_2$	164 ± 2	78 ± 5	210 ± 2	67 ± 5
$MnCl_2$	180 ± 5	45 ± 25	230 ± 5	35 ± 25
$CoCl_2$	190 ± 5	40 ± 25	235 ± 5	35 ± 25

The infrared spectra of $MnCl_2$ and $CoCl_2$ were briefly investigated for comparison purposes. Results obtained at 5 cm^{-1} resolution are given in Table 5.1. The estimated errors are large because the spectra were analysed by the wing-folding technique only.

Several far infrared measurements were made on single crystals as well as the powder samples. Discs approximately 0.1 mm thick were cleaved off the bulk crystal in such a way that the disc faces were perpendicular to the c axis. These slices were arranged to cover the sample area of the spectrometer, and were carefully aligned so that the crystal c axis was parallel to the direction of propagation of the near-parallel infrared light. As could be expected, the axial spectra showed complete absorption over a wide frequency interval. Several runs were made on each sample, and the averaged results are given below.

Crystal	Limits of Zero Transmission	Average of Limits.
$CdBr_2$	65±3.5 cm^{-1} - 240±3.5 cm^{-1}	153±12 cm^{-1}
$CdCl_2$	95±3.5 cm^{-1} - 330±3.5 cm^{-1}	213± 8 cm^{-1}

The second-order infrared absorption spectra of $CdBr_2$, $CdCl_2$, $CoCl_2$ and $MnCl_2$ were recorded using a Beckman IR-12 spectrometer. Measurements were made at

room and liquid air temperatures by means of a metal dewar in which the sample is cooled by thermal contact with a refrigerated copper block. The construction of the dewar is described in detail by Robson.[82] The dewar was fitted with CsI windows which are transparent over the entire operating region (200 - 4000 cm^{-1}). The crystal samples were cleaved and cut to size just prior to mounting in the dewar, which was then evacuated. The whole process was carried out as quickly as possible to minimise exposure of the sample to the atmosphere. Despite the precautions taken, sample contamination was seen in several spectra as will be mentioned later. Axial and transverse (σ,π) spectra were measured for different crystal thicknesses. Unfortunately, it was physically impossible to cut sufficiently thin specimans for transverse second-order measurements. The crystal fell apart along cleavage planes whenever a thin transverse cut was attempted.

Representative axial spectra taken at 85°K are shown in Fig. 5.4. The sharp line at 670 cm^{-1} common to all the spectra is a CO_2 absorption. The $CoCl_2$ spectrum exhibits an interference pattern at wavenumbers beyond 500 cm^{-1}. Such patterns are caused by interference of the incident light within the sample. Very thin samples were needed to completely resolve the

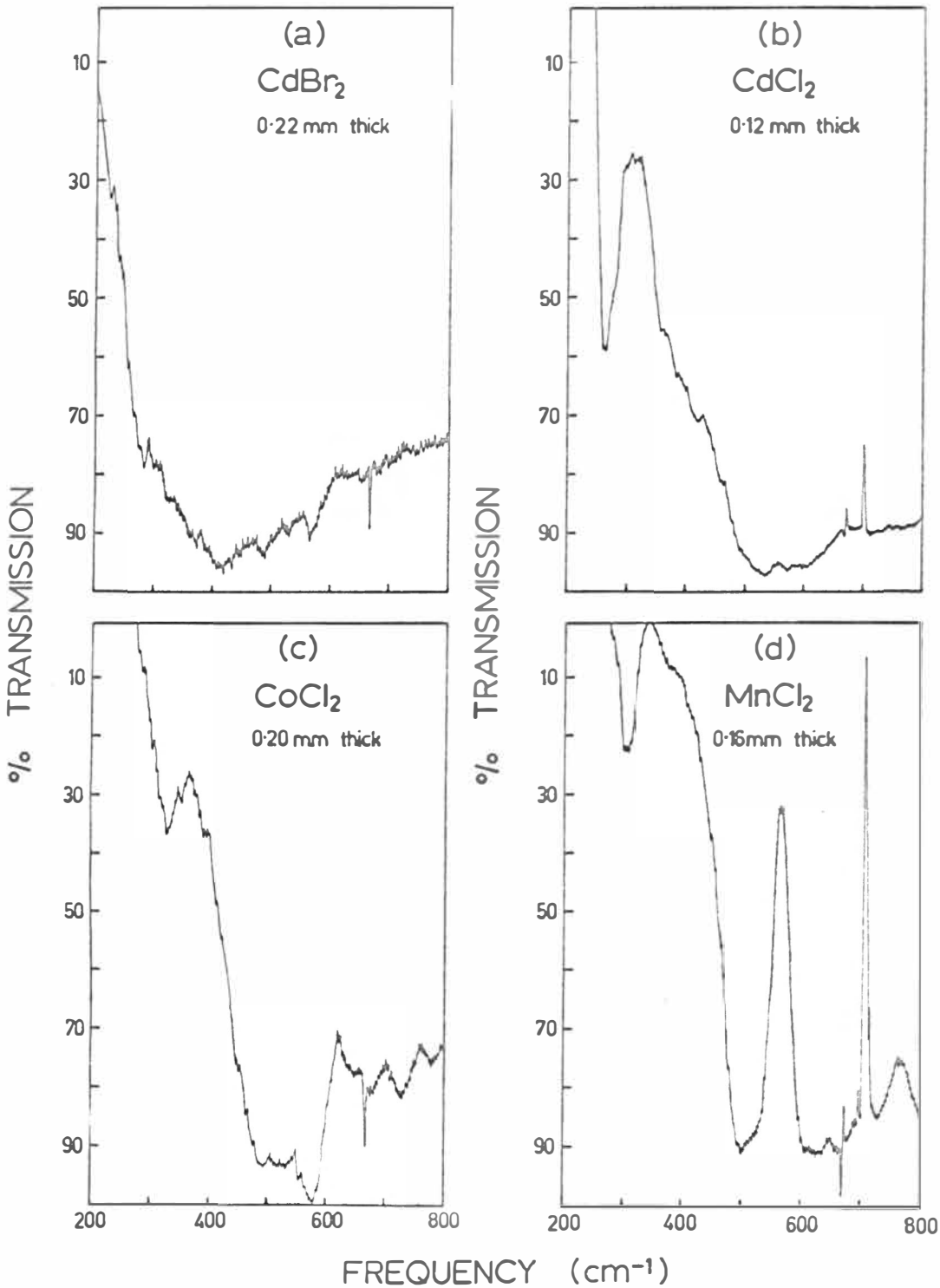

Fig. 5.4. Axial infrared absorption spectra at 85°K.

second-order spectrum because of the close proximity of a first-order infrared line. The two-phonon cut-offs are at ~ 300 cm^{-1} for $CdBr_2$ and ~ 500 cm^{-1} for the rest. The second-order bands are almost featureless.

The IR-12 spectrometer slits are programmed to give constant energy on the detector with no sample present. Consequently, the slit width varies with wavenumber. In Fig. 5.4, the spectrometer resolution ranges from 4.2 cm^{-1} at 200 cm^{-1}, through 5.1 cm^{-1} at 350 cm^{-1} to 1.1 cm^{-1} at 700 cm^{-1}.

The spectra in Fig. 5.4 show typical additional features that were observed in some samples. These features are listed in Table 5.2.

Table 5.2 Infrared impurity lines.

No.	Description	Frequency in cm^{-1} at $85^{o}K$			
		$CdBr_2$	$CdCl_2$	$CoCl_2$	$MnCl_2$
1	n[a],w[b]	230	-	-	-
2	n,w	290	-	-	-
3	b,m	390	560	-	560
4	v.n,w	-	587	-	-
5	v.n,w	-	600	-	-
6	v.n,w	-	631	-	-

		$CdBr_2$	$CdCl_2$	$CoCl_2$	$MnCl_2$
7	v.n,v.w	-	660	-	-
8	v.n,w	-	-	-	673
9	v.n,v.w	-	-	-	690
10	v.n,w	-	not resolved	-	697
11	v.n($\leqslant 5 cm^{-1}$),s	696.5±0.5	700.5±0.5	-	708.5±0.5
12	v.n,w	-	not resolved	-	715
13	v.n,v.w	740	745	-	780
14	b,w	-	760	-	770
15	v.n,w	-	1202	-	1030
16	v.n,w	-	1223	-	1055
17	b,v.w	-	-	-	1110
18	n,m	-	1595	1595	1600
19	b,w	-	-	-	2360
20	v.n,v.w	-	-	-	3140
21	v.n,w	-	-	3185	3190
22	v.n,w	-	3260	-	-
23	v.n,w	-	3338	-	-
24	v.n,w	-	3355	-	-
25	b,m	-	3470	3420	3450
26	b,m	-	3530	3480	3510

[a]Line shape: n = narrow, b = broad, v = very.

[b]Line strength: w = weak, m = medium, s = strong.

Line no. 3 was usually observed some time after exposure of the crystal to the atmosphere. Leaving the crystal in the dewar overnight was a sufficiently long time. This line caused considerable trouble in the early measurements because it appeared to be part of the second-order spectrum. However, later measurements with improved techniques indicated that it was completely independent of the two-phonon spectrum. The occurrence and strength of the impurity lines listed in Table 5.2 depended upon the quality of the crystal starting material, the crystal growing treatment, and the handling of the sample. The σ-π spectra of $CdCl_2$ and $CdBr_2$ did not show any new impurity features. Polarization measurements were made on the strong impurity line no. 11 using a AgCl stacked-plate polarizer inserted in the IR-12 optical path. The ratio of the π/σ intensities was ~ 1.5 in $CdCl_2$. The AgCl absorption limited polarization measurements to frequencies greater than 450 cm^{-1}.

C H A P T E R 6

DISCUSSION OF RESULTS

6.1 The Raman Spectra

The observed Raman lines have been assigned to the A_{1g} mode in each crystal for the following reasons.

(1) The Raman lines are strong; a characteristic feature of totally symmetric modes.[13]

(2) The Raman second harmonics are at frequencies of 295 cm^{-1} in the bromide and 464 cm^{-1} in the chloride. The infrared two-phonon cut-off at 300 cm^{-1} for the bromide and 500 cm^{-1} for the chloride does not support a higher fundamental Raman frequency. The two-phonon absorption edge is cation independent, which suggests that the limit is set by a Raman-active overtone.

(3) The Raman line is always strongest in experimental conditions which involve the diagonal components of the polarizability tensor. Because of the strength of the diagonal tensor components, the line can be associated with the completely polarized A_{1g} mode. However, some care must be taken with polarization measurements in uniaxial crystals. The

polarization of the A_{1g} mode is very sensitive to the directions of the incident and scattered light within the crystal. The light need only diverge slightly from the optic axis to be strongly depolarized due to interference of its ordinary and extraordinary components.[83] Besides this, wandering of the c axis within the crystal will produce a residual depolarization.[84] The crystals used were not optically perfect, so reflection and refraction of the scattered light will also tend to depolarize the A_{1g} line. All three effects combine to produce the experimentally observed depolarization.

(4) The chloride to bromide frequency shift is consistent with the fact that the A_{1g} mode involves movement of the anions only. The harmonic oscillator model gives the frequency of a mode as $\nu = (k/4\pi^2 m)^{\frac{1}{2}}$, where k is the force constant and m is the reduced mass. The chlorine to bromine mass shift gives a frequency ratio of $\nu_{Cl}/\nu_{Br} = (80/35)^{\frac{1}{2}} = 1.52$ which compares with the experimental result of 1.58. A small change in the force constant is implied.

Electronic absorption spectra of Fe^{2+} in these crystals show vibronic side-bands such as those in Fig. 6.1.[85] The arrows in the figure mark the position of

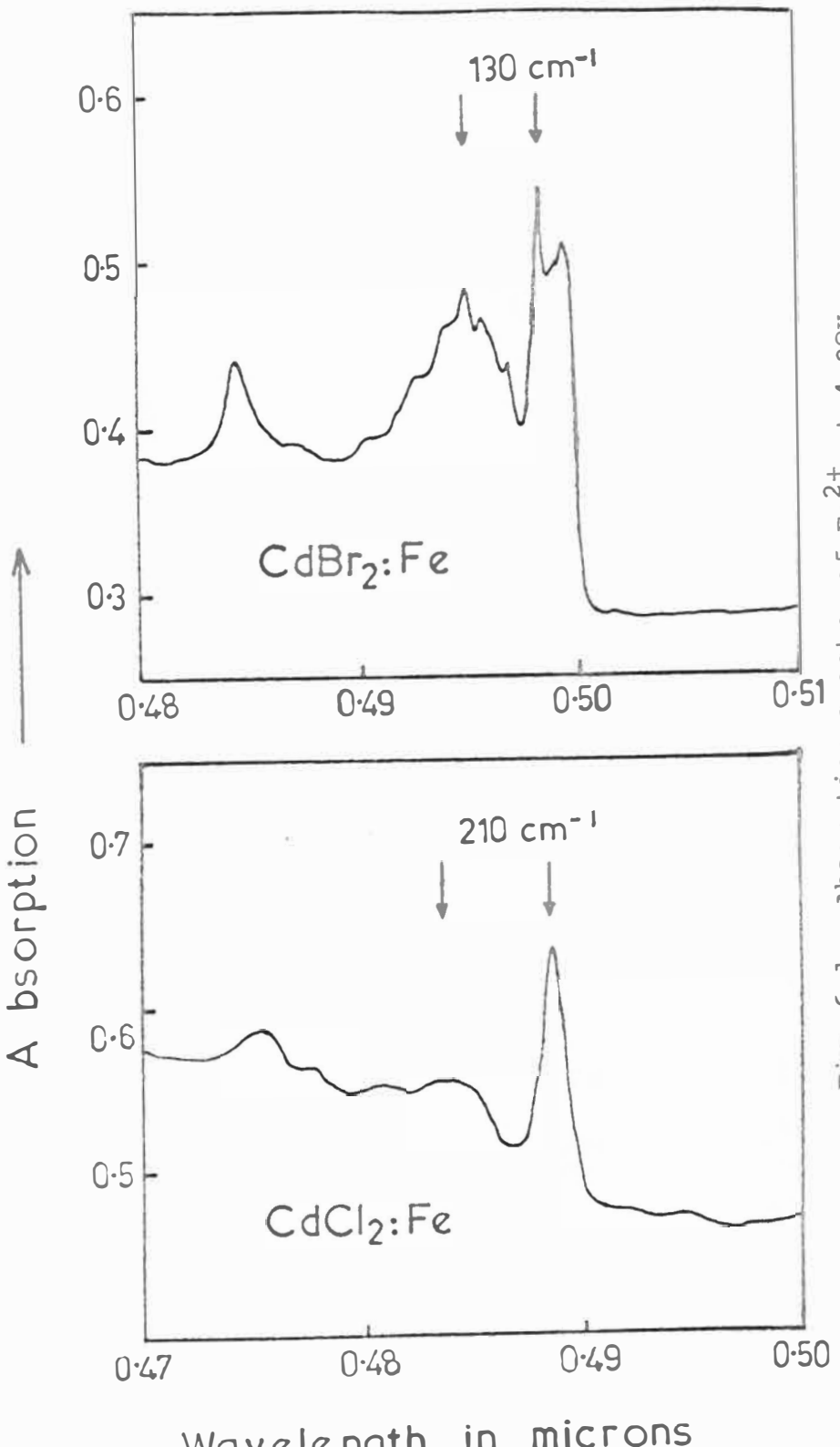

Fig. 6.1. Absorption spectra of Fe^{2+} at 4.2°K.

the electronic line and the highest peak in the vibronic side-band. The spacing between arrows is given in cm^{-1}. The energy shifts confirm that the Raman results are of the right order.

Even though the E_g modes have not been observed, their frequencies can be predicted. Jahn-Teller effect measurements on Fe^{2+} in $CdCl_2$ and $CdBr_2$ provide the information required. In crystals of trigonal symmetry, E_g vibrational modes are involved in lifting the degeneracy of the $^5E_g(^5D)$ states of Fe^{2+} through the dynamic Jahn-Teller effect.[86,67] The E_g modes involved can come from throughout the entire Brillouin zone. Freeman and Jones[67] have obtained a value for the effective E_g frequency from the temperature dependence of the Jahn-Teller splitting. These frequencies are 93 cm^{-1} for $CdCl_2$ and 66 cm^{-1} for $CdBr_2$. Unless the phonon dispersion curves show marked curvature, the $\underline{k} = 0$ E_g modes are likely to have frequencies close to these effective values.

It is intended to remeasure the Raman spectrum of $CdCl_2$ and $CdBr_2$ with the new Jarrell-Ash spectrometer. The spectrometer should enable Raman frequencies less than 100 cm^{-1} to be observed. The measurements will be made on crystals of improved optical quality. (The

crystals were annealed after the growing stage to minimise dislocations and other crystal growth defects.) Careful attention will be paid to polarization measurements. A half-wave retardation plate will be used to rotate the plane of polarization of the laser line within the crystal, instead of rotating the crystal. This manoeuvre will assist in distinguishing between the E_g and A_{1g} modes through their different intensity versus laser polarization behaviour.[87,88]

6.2 The Infrared Spectra

The fundamental infrared frequencies can not be directly assigned to any symmetry because the measurements were made on powders. However, the single crystal work does provide some information. In theory, axial infrared spectra should not show the A_{2u} mode, as the infrared electric vector is orthogonal to the A_{2u} vibrational moment. If the crystal is not correctly oriented, the A_{2u} mode will couple to the light. The strength of coupling increases as the alignment deteriorates. The far infrared measurements of the axial spectrum were carefully arranged to minimise the A_{2u} mode coupling. The resultant spectra (see page 122) show very little absorption at the low energy and

where, according to the powder results, another line exists. The results indicate that the high-frequency ν_2 line is the E_u mode. The fact that the ν_2 frequency (Table 5.1) is close to the centre of the axial absorption band indicates that very little, if any, of the A_{2u} mode was observed in the axial spectra.

The symmetry assignment we have made is that line ν_2 belongs to the E_u mode and ν_1 to the A_{2u} mode for all crystals listed in Table 5.1. This assignment should be confirmed by single crystal reflection measurements using wire-grid polarizers. Low temperature results would also be interesting, because the two lines in the powder spectra should be resolved at low temperatures. Such experiments are beyond the scope of the present equipment.

The $MnCl_2$ and $CoCl_2$ infrared spectra are very similar, as can be expected from the position of Co and Mn in the periodic table. The $MnCl_2$ and $CoCl_2$ linewidths as given in Table 5.1 are probably less than the true value, because the wing-folding technique produces narrower lines compared with those produced by fitting the classical dispersion formula. The large error in linewidth takes account of this. The $CdCl_2$ frequencies are lower than those of the other chlorides

in accordance with the greater atomic mass of Cd compared with Co and Mn.

It should be noted that inorganic powder spectra generally give higher frequencies and broader linewidths than reflection spectra of single crystals.[89] The higher frequencies and linewidths are a consequence of the small particle size. The lines may also be broadened by impurities in the powder. This is almost certainly the case here, as it is very difficult to completely remove the water of crystallization from the starting material. $CdCl_2$ and $CdBr_2$ crystals readily accept the OH^- ion, because CdCl(OH) and CdBr(OH) have the same structure as $CdCl_2$.[68]

The assignment of peaks in the second-order spectrum is difficult because the phonon dispersion curves are not known. As in the second-order Raman effect, the second-order infrared spectrum involves contributions from pairs of phonons of equal and opposite wave vector from throughout the Brillouin zone. Peaks in the spectrum are associated with peaks in the density of states arising at critical points.[20] The discussion of the second-order spectra will be restricted to the assignment of peaks arising from the zone-centre critical point, where the fundamental frequencies are known.

The Kronecker products of pairs of all fundamental-mode irreducible representations were formed,[90] and the infrared-active combinations selected. The symmetrized Kronecker squares are not needed, as the $\underline{k} = 0$ overtone states are not infrared active.[91,92] Four $\underline{k} = 0$ combinations are infrared active. These combinations and the assigned experimental results are given in Table 6.1 for $CdBr_2$, $CdCl_2$, $CoCl_2$ and $MnCl_2$. The E_g frequencies used in the table are the approximate values given by the Jahn-Teller effect measurements. The $CdCl_2$ Raman frequencies were used for $CoCl_2$ and $MnCl_2$ also. This latter approximation is reasonable, as the symmetry coordinate analysis shows that the Raman modes are almost independent of the cation. The A_{2u} combination state is not observable in the axial spectrum.

The experimental results listed in Table 6.1 are not expected to be in close agreement with theory because of the approximations mentioned above. In addition, experimental frequencies measured at $85^{o}K$ are compared with room temperature theoretical values. Allowing for these facts, there is a reasonable agreement between theory and experiment. The lack of structure in the second-order spectra of $MnCl_2$ and $CoCl_2$ does not assist the assignment. This general lack of structure is

Table 6.1 Selection Rules and the assignment of peaks in the second-order infrared axial spectra.

Allowed $\underline{k} = 0$ Combinations.	Frequency Assignment (cm^{-1})							
	$CdBr_2$		$CdCl_2$		$CoCl_2$[b]		$MnCl_2$[b]	
	Theory	Expt	Theory	Expt	Theory	Expt	Theory	Expt
$A_{1g} \times A_{2u} = A_{2u}$	249	-	396	-	422	-	412	-
$A_{1g} \times E_u = E_u$	308	305	442	430	467	460	462	455
E_g[a] $\times A_{2u} = E_u$	168	-	257	270	283	-	273	-
E_g[a] $\times E_u = A_{1u} + A_{2u} + E_u$	227	240	303	310	328	350	323	340

[a] The E_g frequencies are taken from Freeman and Jones.[67]

[b] The $CdCl_2$ A_{1g} and E_g frequencies are used for this crystal.

disappointing, especially since experimental studies of two-phonon spectra of non-cubic systems are of interest at present.[93] Cooling the samples to liquid helium temperatures may enable more structure to be resolved.

6.3 The Impurity Spectra

The impurity lines in the $CdCl_2$ type crystals can be divided into three groups. The first group consists of lines 18, 25 and 26 (see Table 5.2), which always occur together. These lines can be associated with vibrations of the OH^- ion. The line at 1595 cm^{-1} is associated with the bending of the OH bond[94] and the lines 25 and 26 with the stretching of the bond.[94,95] Line 18 appears to be independent of the host, whereas 25 and 26 are slightly dependent on the host. Lines 25 and 26 represent peaks in a complex broad structure. It is interesting to note that the peak separation is 60 cm^{-1} in all three crystals. The splitting of the OH stretching band, and the fact that the frequencies are much lower than those for OH^- in the alkali halides,[95] is probably due to the host. Crystals with the $CdCl_2$ structure readily accept OH^- ions because CdCl(OH) forms the same structure. Consequently there will be a strong interaction between the OH^- ion and the host.

The lines were never seen in the $CdBr_2$ samples. This is because $CdBr_2$ is much less hygroscopic than $CdCl_2$, $CoCl_2$ or $MnCl_2$. The $CdBr_2$ starting material was very pure, and the impurity lines that were observed were much weaker than those in the other crystals.

The second group comprises the broad lines 3, 14, 17 and 19. Lines 3 and 14 always appear together with approximately the same intensity ratio. These two lines are independent of the cation, but they are dependent on the anion. As mentioned earlier, the lines usually appear some time after exposure of the crystal to the atmosphere. These facts suggest that the frequencies can be assigned to vibrations of oxy-chloride and oxy-bromide bonds. The origin of lines 17 and 19 is unknown.

The third group consists of the remaining lines, which are all very narrow. Their frequencies are much higher than the vibrational frequencies of the host. This suggests that the lines arise from impurity vibrations of the local-mode type. The exceptions are lines 1 and 2, which coincide with water vapour lines. Line 1 is definitely due to water vapour contained in the IR-12 spectrometer. Line 2 is not so definite, as this line was very strong in some $CdBr_2$ samples. The strongest impurity feature is line 11. This line was examined in some detail. The line position did not

appear to change with temperature from 10°K to 300°K, although the linewidth decreases at the lower temperatures, and the line frequency is almost independent of the host. Adding CdO to the $CdBr_2$ crystal resulted in a marked increase in the intensity of the impurity line. Polarization measurements show that the line is partially π polarized. These facts indicate that the line is caused by an oxygen centre that could be associated with an anion vacancy. The centre is not a free O_2^- ion, as this ion does not produce infrared-active vibrations.[96] Line 13 also appears to be due to an oxygen centre, as its intensity and occurrence are related to the behaviour of line 11. The remainder of the narrow impurity lines are weak in intensity, and only occur in samples with high impurity concentrations. Lines 4 - 10 and 12 are most likely associated with the strong oxygen-centre line. Lines 22-24 can be assigned to OH^- ions near impurities.[95] The rest of the lines are of unknown origin.

$CoCl_2$ exhibits electronic absorption in the 800 cm^{-1} region. Newman and Chrenko[97] report a sharp line at 0.0912 eV (735 cm^{-1}) in addition to a broad vibronic envelope. We have seen the vibronic structure which covers the range 800 - 1300 cm^{-1}, but have not

found the line at 735 cm^{-1}. The absorption strength of the 735 cm^{-1} line is as great as that of the vibronics,[97] so it could not have been missed. We suggest that the 735 cm^{-1} line is due to the oxygen impurity centre. Our $CoCl_2$ samples were relatively free of impurities, and did not show any impurity lines in the low wave-number region.

Further study of the impurity spectra is beyond the scope of this thesis. However, the effect of the impurities on the second-order infrared or Raman spectra is important. The impurities could considerably influence the shape of the two-phonon density-of-states versus wave-vector curves. Future second-order measurements would have to be made on much purer samples.

CHAPTER 7

THE ELECTRONIC RAMAN EFFECT

7.1 Introduction

The study of electronic Raman scattering by ions in crystals is a relatively new field in Raman spectroscopy. The first experimental results on $PrCl_3$ were reported by Hougen and Singh in 1963,[98] in response to a theoretical paper by Elliott and Loudon.[99] The advent of the laser light source has enabled full development of work in this field.

A study of the electronic Raman effect is worthwhile for two reasons. Firstly, new information can be obtained on low-lying energy states of an ion. Raman selection rules are different from those associated with electric-dipole transitions, and hence different transition frequencies can be observed. Secondly, information is obtained on the fundamental processes involved in Raman scattering. In particular, the electronic Raman effect has brought forward the significance of the antisymmetric components in the polarizability tensor.[100]

Having studied the lattice vibrations of $CdCl_2$ and $CdBr_2$, it was an obvious step to go on and examine the electronic Raman effect of transition metal (TM) ions in these crystals. Scattering by TM ions is especially interesting because all previous studies have involved rare earth ions only. The points to note in measuring the spectra are the appearance of new frequencies, the intensity of the transitions, and the symmetry of the Raman tensor.

The TM ions chosen for detailed study were iron and cobalt. These ions can be heavily doped into $CdCl_2$ and $CdBr_2$ because their chlorides are isomorphic with the $CdCl_2$ structure. Cobalt doped $CdCl_2$ is blue in colour, and the bromide is green; the iron doped crystals have a pale yellow colour. Thus these crystals are ideal for study using the blue-green argon laser lines. The Raman scattering in the case of the ferrous ion could be resonance enhanced under excitation by the 4880Å line. As Fig. 6.1 shows, this line is close to weak spin-forbidden Fe^{2+} absorptions.

When this work was attempted, little was known about the low-lying energy levels of iron and cobalt in $CdCl_2$ type crystals. The effect of a trigonal crystal field on the ground states of Fe^{2+} ($3d^6$ configuration) and Co^{2+} ($3d^7$ configuration) is shown

in Fig. 7.1. The order of the two lowest energy levels is determined by the sign of the crystal field. ESR measurements on Co^{2+} in $CdCl_2$ and $CdBr_2$ have shown that the orbital singlet ($^4A_{2g}$) is lowest.[101] This means that for Fe^{2+} the doublet is lowest.[102] The energy levels as drawn are also split by the spin-orbit interaction, and additional complications arise in the case of iron from Jahn-Teller splitting of the degenerate ^5E_g levels.[67,75]

7.2 Experiment

The energies of the spin-orbit split $^5E_g - {}^5A_{1g}$, $^4A_{2g} - {}^4E_g$ transitions were investigated by Raman scattering. Crystals of $CdCl_2$ and $CdBr_2$ doped with Fe^{2+} and Co^{2+} at five mole percent concentrations were examined at room temperature using the 4880Å laser line. Careful examination of the 80 - 1200 cm^{-1} Stokes region at the limit of sensitivity of the present equipment failed to show any electronic Raman lines.

Subsequent optical[75] and infrared[82] work has determined the energy levels of Co^{2+} and the upper energy levels of Fe^{2+} in these crystals. At present, the splitting of the $^5T_{2g}$ ground state of iron has not been determined. If these energy levels are to be

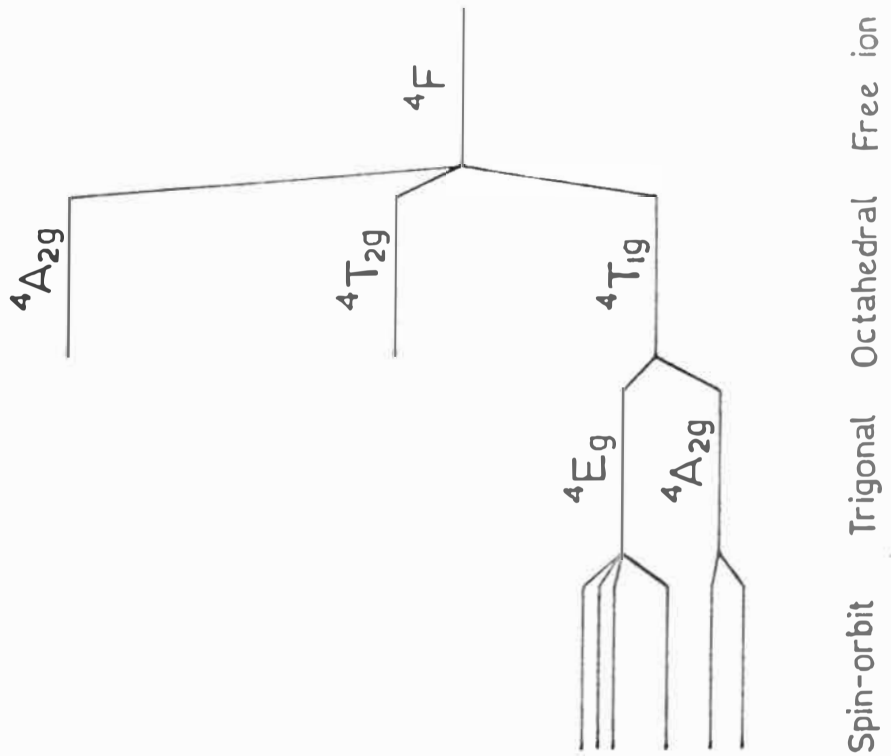

Fig. 7.1. Ground state energy-level splittings for (a) Fe^{2+} and (b) Co^{2+} ions in $CdCl_2$.

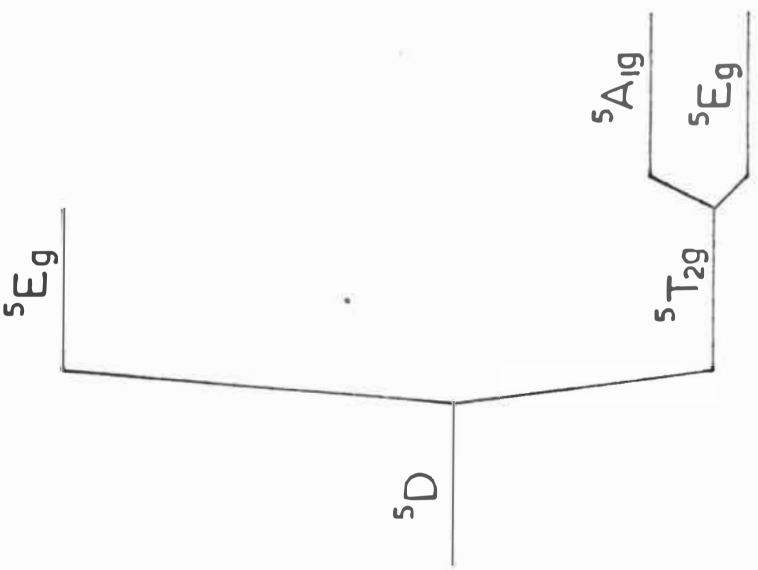

observed in Raman scattering, the measurements should be made at low temperatures to sharpen the lines, and with higher sample concentrations.[103] However, there is no guarantee that the transitions can be observed. For example, rare earth ions in CaF_2 and $CaWO_4$ failed to produce observable low energy electronic spectra,[104,105] while such ions in the garnets,[100,106] YVO_4[107] and the rare earth trichlorides[98,108] produce spectra almost as strong as the Raman phonon spectra. It is intended that further electronic Raman measurements be made on TM ions using the new Jarrell-Ash spectrometer in combination with low temperature facilities.

REFERENCES

1. G.B. Wright, Ed., "Light Scattering in Solids" (Springer Verlag, New York, 1969).
2. C.V. Raman, Indian J. Phys. 2, 387 (1928); C.V. Raman and K.S. Krishnan, Nature 121, 501 (1928).
3. G. Landsberg and L. Mandelstam, Naturwiss. 16, 557, 772 (1928).
4. A. Smekal, Naturwiss.11, 873 (1923).
5. H.A. Kramers and W. Heisenberg, Z. Phys. 31, 681 (1925).
6. P.A.M. Dirac, "The Principles of Quantum Mechanics" (4th ed., Oxford University Press, London, 1958).
7. W. Heitler, "The Quantum Theory of Radiation" (3rd ed., Oxford University Press, London, 1954).
8. P.A.M. Dirac, Proc. Roy. Soc. (London) A114, 710 (1927).
9. G. Placzek, "Marx Handbuch der Radiologie", 2nd ed., Vol. VI, Part 2, pp 209-374, 1934.
10. J. Behringer and J. Brandmüller, Z. Elektrochem. 60, 643 (1956) and 62, 906 (1958); and J. Behringer in "Raman Spectroscopy, Theory and Practice", H.A. Szymanski, Ed., (Plenum Press, New York, 1967).
11. V. Heine, "Group Theory in Quantum Mechanics" (Pergamon Press, London, 1960).

12. A.C. Albrecht, J. Chem. Phys. 34, 1476 (1961); J. Tang and A.C. Albrecht, J. Chem. Phys. 49, 1144 (1968).

13. C.H. Ting, Spectrochim. Acta 24A, 1177 (1968).

14. J.A. Koningstein, J. Mol. Spectry 28, 309 (1968).

15. See reference 12 for recent examples.

16. M. Born and M. Bradburn, Proc. Roy. Soc. (London) A188, 161 (1947).

17. M. Born and K. Huang, "Dynamical Theory of Crystal Lattices" (Oxford University Press, London, 1954).

18. Reference 6, p.68.

19. C.H. Henry and J.J. Hopfield, Phys. Rev. Letters 15, 964 (1965).

20. F.A. Johnson and R. Loudon, Proc. Roy. Soc. (London) A281, 274 (1964).

21. G.W. Cohen-Solal, C. Leenhardt and A. Bassompierre, Comptes Rendus 261, 357 (1965).

22. R. Loudon, Advan. Phys. 13, 423 (1964) and references therein.

23. L.N. Ovander, Opt. Spectry 9, 302 (1960).

24. J.L. Birman, Phys. Rev. 127, 1093 (1962).

25. R.A. Cowley, Proc. Phys. Soc. London 84, 281 (1964).

26. V.L. Strizhevskii, Soviet Phys. - Solid State, 3, 2141 (1962) 4, 1096 (1962) and 5, 1099 (1963).

27. L.N. Ovander, Soviet Phys. - Solid State 3, 1737 (1962) and subsequent papers referenced in the review article: L.N. Ovander, Soviet Phys. - Uspekhi 8, 337 (1965).

28. R. Loudon, Proc. Roy. Soc. (London) A275, 218 (1963).

29. J.L. Birman and A. Ganguly, Phys. Rev. Letters 17, 647 (1966) and Phys. Rev. 162, 806 (1967).

30. F.A. Johnson, reference 1, paper B-1.

31. R.S. Knox, "Theory of Excitons" (Academic Press, New York, 1963).

32. A. Pinczuk and E. Burstein, Phys. Rev. Letters 21, 1073 (1968).

33. R.C.C. Leite, J.F. Scott and T.C. Damen, Phys. Rev. Letters 22, 780 (1969).

34. M.V. Klein and S.P.S. Porto, Phys. Rev. Letters 22, 782 (1969).

35. E. Burstein, D.L. Mills, A. Pinczuk and S. Ushioda, Phys. Rev. Letters 22, 348 (1969).

36. A. Weber, The Spex Speaker 11, No. 4, Dec. 1966.

37. A.D. White, Appl. Opt. 3, 431 (1964).

38. G. de Mars, M. Seiden and F.A. Horrigan, IEEE J. Quantum Electronics QE-4, 631 (1968).

39. J.C. Kaufman, MicroWaves 5, No. 4, April 1966.

40. D. Landon and S.P.S. Porto, Appl. Opt. 4, 762 (1965).

41. G.W. Stroke in "Handbuch der Physik", S. Flügge, Ed., (Springer Verlag, Berlin, 1967), Vol. 29, pp. 426-754.

42. Jarrell-Ash Technical Bulletin no. EB-130, June 1965.

43. R.L. Christensen and R.J. Potter, Appl. Opt. 2, 1049 (1963).

44. F.A. Jenkins and H.E. White, "Fundamentals of Optics" (3rd Ed., McGraw-Hill, New York, 1957), p.333.

45. T.M. Hard and R.C. Lord, Appl. Opt. 7, 589 (1968).

46. Jarrell-Ash Technical Bulletin no. EB-133, May 1966.

47. M. Delhaye and M. Bridoux, Comptes Rendus 261, 2079 (1965).

48. J. Sharpe, EMI Electronics Ltd, document no. C.P. 5475, Oct. 1964; J.P. Rodman and H.J. Smith, Appl. Opt. 2, 181 (1963).

49. L. Frommhold and W.A. Feibelman, J. Sci. Instrum. 44, 182 (1967).

50. M.L. Franklin, G. Horlick and H.V. Malmstadt, Anal. Chem. 41, 2 (1969).

51. R.R. Alfano and N. Ockman, J. Opt. Soc. Am. 58, 90 (1968).

52. R.G. Tull, Appl. Opt. 7, 2023 (1968).

53. D.L. Akins, S.E. Schwartz and C.B. Moore, Rev. Sci. Instrum. 39, 715 (1968).

54. Y.-H. Pao and J.E. Griffiths, J. Chem. Phys. 46, 1671 (1967).

55. F.T. Arecchi, E. Gatti and A. Sona, Rev. Sci. Instrum. 37, 942 (1966).

56. G.A. Morton, Appl. Opt. 7, 1 (1968).

57. R.C.C. Leite and S.P.S. Porto, J. Opt. Soc. Am. 54, 981 (1964).

58. V. Ananthanarayanan, Z. Phys. 167, 39 (1962).

59. For recent examples of such applications see the IBM J. Res. Develop. 13, 1-148, Jan. 1969.

60. The PDP-8 Users Handbook.

61. R.T. Schneider and R.O. Whitaker, "Photoelectric Detection of Weak Spectrum Lines", NASA Contractor Report No. 397, March 1966.

62. See for example D.A. Jackson and E.R. Pike, J. Sci. Instrum. (Series 2) 1, 394 (1968); J.W. Weymouth, J. Costello, S. Schuster and P. Schulze, Rev. Sci. Instrum. 39, 476 (1968).

63. M. Delhaye, Appl. Opt. 7, 2195 (1968).

64. A. Perregaux and G. Ascarelli, Appl. Opt. 7, 2031 (1968).

65. H. Matsumoto, J. Phys. Soc. Japan 20, 1579 (1965).

66. T. Iri and G. Kuwabara, J. Phys. Soc. Japan 24, 127 (1968) and references therein.

67. T.E. Freeman and G.D. Jones, Phys. Rev. (to be published).

68. R.W.G. Wyckoff, "Crystal Structures", 1 (Interscience Publishers, New York, 1964).

69. I.F. Chang and S.S. Mitra, Phys. Rev. 172, 924 (1968).

70. S. Bhagavantam and T. Venkatarayudu, "Theory of Groups and Its Application to Physical Problems" (Andhra University, Waltair, India, 1951).

71. D.F. Hornig, J. Chem. Phys. 16, 1063 (1948).

72. H. Winston and R.S. Halford, J. Chem. Phys. 17, 607 (1949).

73. S.K. Dickinson, "Guide to the Interpretation of Space Group Symbols", U.S. Air Force Cambridge Research Laboratories Report No. AFCRL-65-279, April 1965.

74. D.C. Stockbarger, Rev. Sci. Instrum. 7, 133 (1936).

75. T.E. Freeman, M.Sc. thesis, University of Canterbury, 1969.

76. T.C. Damen, S.P.S. Porto and B. Tell, Phys. Rev. 142, 570 (1966).

77. G.D. Dean and D.H. Martin, Chem. Phys. Letters 1, 415 (1967).

78. The polyethylene powder was supplied by Robert Bryce and Co. Ltd, Christchurch, N.Z.

79. F. Seitz, "The Modern Theory of Solids" (McGraw-Hill, New York, 1940).

80. W.G. Spitzer and D.A. Kleinman, Phys. Rev. 121, 1324 (1961); W.G. Spitzer, R.C. Miller, D.A. Kleinman and L.E. Howarth, Phys. Rev. 126, 1710 (1962).

81. See reference 17, p. 358.

82. A.B. Robson, M.Sc. thesis, University of Canterbury, 1969.

83. S.P.S. Porto, J.A. Giordmaine and T.C. Damen, Phys. Rev. 147, 608 (1966).

84. C.K. Asawa, R.A. Satten and O.N. Stafsudd, Phys. Rev. 168, 957 (1968).

85. The Fe^{2+} results were provided by T.E. Freeman.

86. G.D. Jones, Phys. Rev. 155, 259 (1967).

87. S.P.S. Porto, reference 1, paper A-1.

88. J.A. Koningstein and O. Sonnich Mortensen, J. Opt. Soc. Am. 58, 1208 (1968).

89. J.T. Luxon and R. Summitt, J. Chem. Phys. 50, 1366 (1969).

90. E.B. Wilson, J.C. Decius and P.C. Cross, "Molecular Vibrations" (McGraw-Hill, New York, 1955), p.331.

91. R. Loudon, Phys. Rev. 137, A1784 (1965).

92. M. Hulin, Phys. Stat. Sol. 21, 607 (1967).

93. K.H. Hellwege, W. Lesch, M. Plihal and G. Schaack, Solid State Comm. 7, 185 (1969).

94. G. Herzberg, "Infrared and Raman Spectra of Polyatomic Molecules" (Van Nostrand, New York, 1945), p.280.

95. B. Wedding and M.V. Klein, Phys. Rev. 177, 1274 (1969).

96. W. Holzer, W.F. Murphy, H.J. Bernstein and J. Rolfe, J. Mol. Spectry 26, 543 (1968).

97. R. Newman and R.M. Chrenko, Phys. Rev. 115, 1147 (1959).

98. J.T. Hougen and S. Singh, Phys. Rev. Letters 10, 406 (1963) and Proc. Roy. Soc. (London) A277, 193 (1964).

99. R.J. Elliott and R. Loudon, Phys. Letters 3, 189 (1963).

100. J.A. Koningstein and O. Sonnich Mortensen, reference 1, paper C-7. This paper reviews developments in the electronic Raman effect.

101. K. Morigaki, J. Phys. Soc. Japan 16, 1639 (1961).

102. J.H. Van Vleck, Discussions Faraday Soc. 26, 96 (1958).

103. J.A. Koningstein, private communication.

104. H.Z. Cummins, "Laser Raman Scattering Studies of Crystals" (Annual Technical Report under Project DEFENDER, Contract No. 4010(06), ARPA Order No. 306-63, June 1966).

105. J.Y.H. Chau (J. Chem. Phys. 44, 1708 (1966)) has reported high energy Raman scattering by Ce^{3+} in $CaWO_4$.

106. J.A. Koningstein, J. Chem. Phys. 46, 2811 (1967).

107. J.A. Koningstein and O. Sonnich Mortensen, Phys. Rev. Letters 18, 831 (1967).

108. A. Kiel, reference 1, paper C-8.

A P P E N D I X

PDP-8 COMPUTER PROGRAMS

A DEC PDP-8 computer has been used as an on-line data processor which can operate in three distinct modes. The computer programs associated with each of these modes of operation are outlined below. The programs were written in Pal III, a computer language devised by the Digital Equipment Corp. for use with the PDP-8. Each program description is accompanied by flow-diagrams and a listing. The format of the listing is a memory address in octal followed by the contents of the address in octal and concluding with the source statement in Pal III. The Pal III compiler ignores any comment statements preceded by the slash symbol.

A.1 Digitise

The object of this program is to convert analogue Raman data into digital form and store the result on paper tape. The main program is designed to cycle in a fixed time so that each data point can be related to wavelength via the scan-rate of the Jarrell-Ash spectrometer. Wavelength information is also

recorded on the paper tape output by means of the 10Å interval marker in the spectrometer. The paper tape output is suitable for use with the University's IBM 360/44 computer. The tape format is arranged so that it is impossible for any row to be blank, otherwise the 360/44 tape reader would ignore the row and thus get out of step.

As the flow diagram of Fig. A.1 shows, the main program consists of a number of subroutines. Subroutine LDR produces 6" of blank paper tape which is used as a leader for the 360/44 tape reader. The ADCVT subroutine digitises the analogue signal presented to the analogue-to-digital converter (ADC). ADC accuracy or word length is controlled by a switch which should be set at 10 bits. This gives a digitisation accuracy of one part in 1024. The digital value is punched on tape by means of subroutine BINPCH.

Subroutine BINPCH takes the first 5 bits of the number, arranges them into a suitable format, tests for the occurrence of a wavelength marker pip, and then outputs the result. The computer waits for approximately 0.1 sec while the punching takes place, and then repeats the process for the remaining 5 bits of the number.

Fig. A.1. Flow diagrams and listing of the DIGITISE computer program.

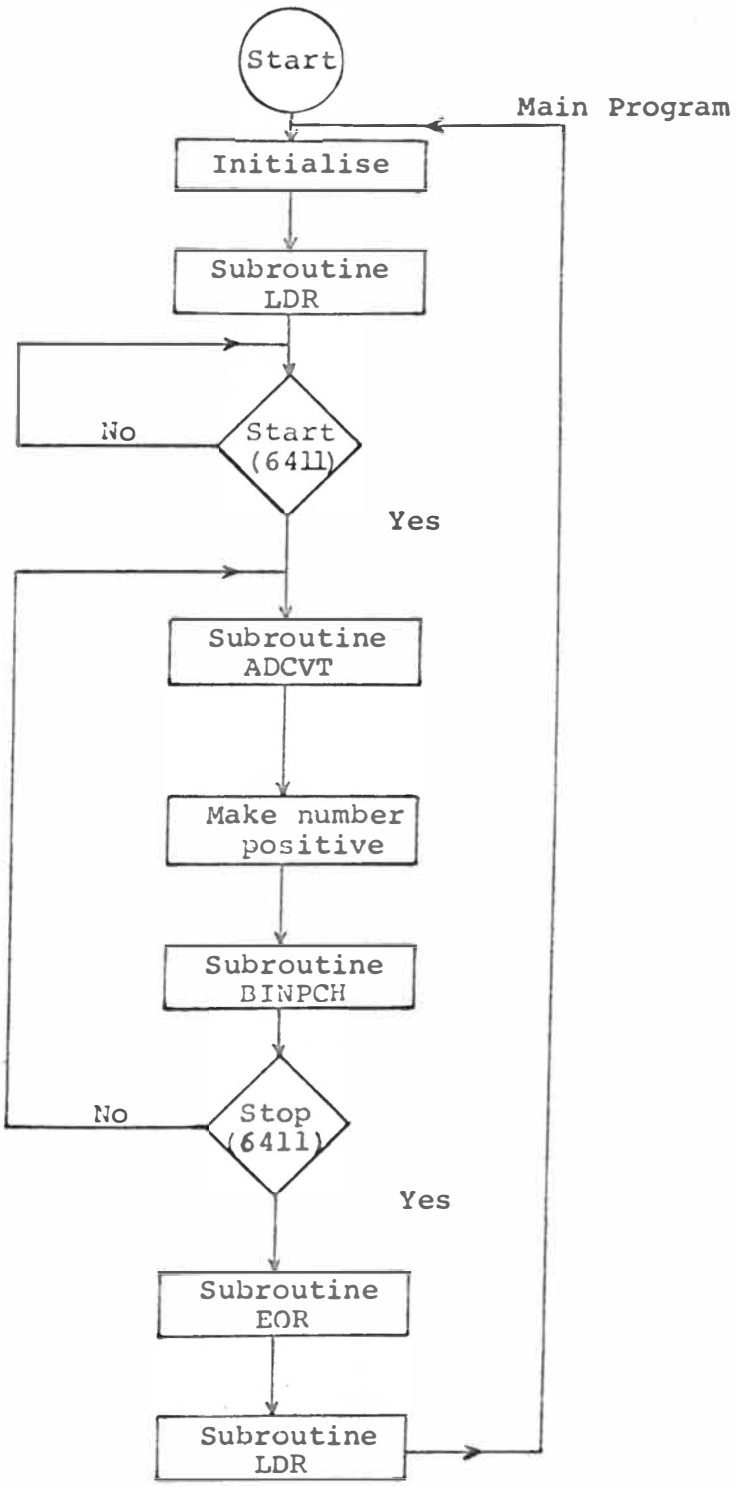

Subroutine BINPCH

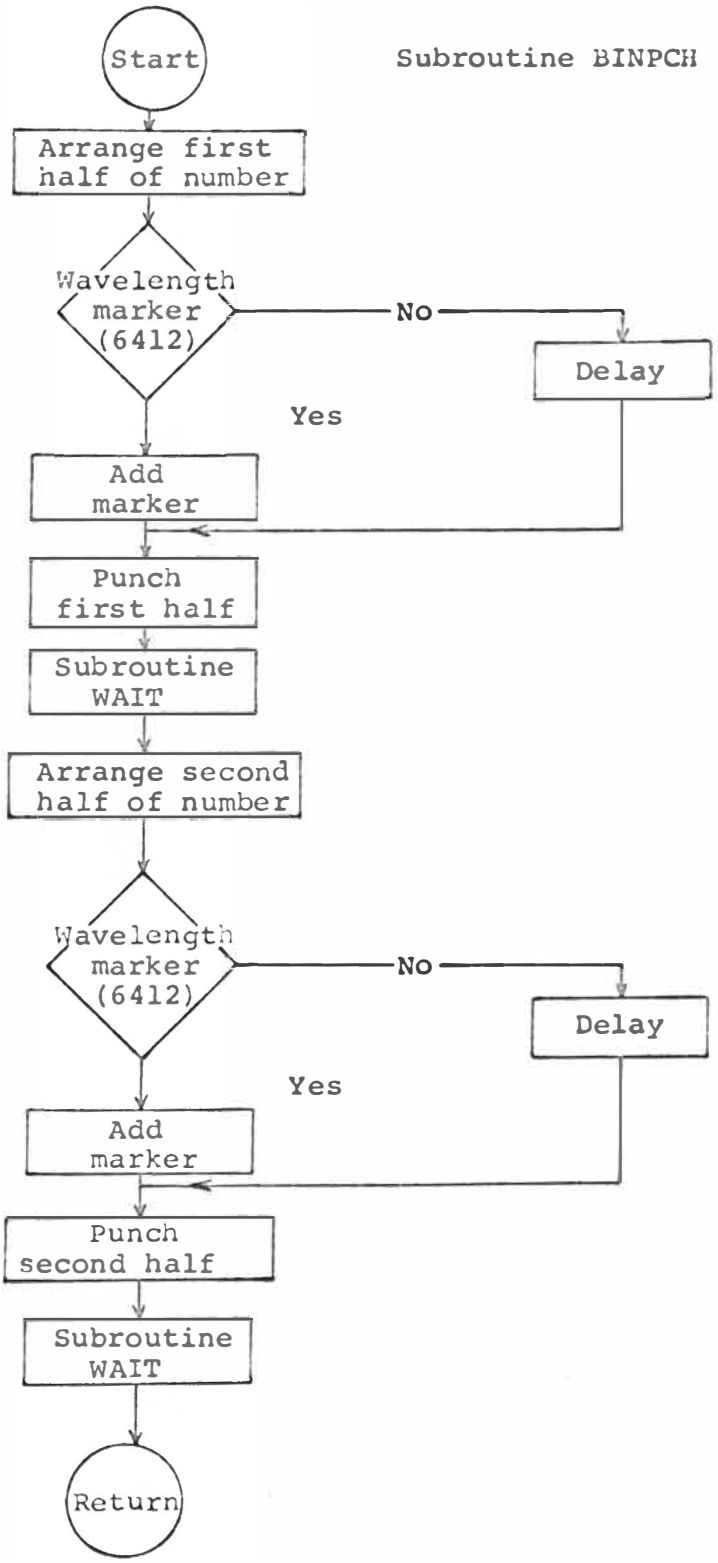

```
                    /MAIN PROGRAM  DIGITISE
                    *200
0200    6044          TPC
0201    7300    START,CLA CLL
0202    4221          JMS LDR
0203    6411          6411    /SKIP IF START FLAG=1
0204    5203          JMP.-1
0205    4235    CONTIN,JMS ADCVT
0206    1220          TAD MKPOS
0207    3217          DCA NUM
0210    4244          JMS BINPCH
0211    6411          6411
0212    5214          JMP.+2
0213    5205          JMP CONTIN
0214    4333          JMS EOR
0215    4221          JMS LDR
0216    5201          JMP START
0217    0000    NUM,0000
0220    4000    MKPOS,4000
                      PAUSE
                    /SUBROUTINE  LDR
                    /PUNCHES BLANK LEADER FOR IBM360-44
0221    0000    LDR,0000
0222    7200          CLA
0223    6041    FREE,TSF
0224    5223          JMP.-1
0225    6046          TLS
0226    2233          ISZ CTR
0227    5223          JMP FREE
0230    1234          TAD CTRA
0231    3233          DCA CTR
0232    5621          JMP I LDR
0233    7704    CTR,-74
0234    7704    CTRA,-74
                      PAUSE
                    /SUBROUTINE  ADCVT
                    /A-D CONVERSION
0235    0000    ADCVT,0000
0236    7200          CLA
0237    6532          ADCV
0240    6531          ADSF
0241    5240          JMP.-1
0242    6534          ADRB
0243    5635          JMP I ADCVT
                      PAUSE
```

```
                /SUBROUTINE  BINPCH
                /PUNCHES 10-BIT BINARY NUMBERS
                /5 BITS AT A TIME
                /A WAVELENGTH MARKER BIT IS PUNCHED
                /WHEN REQUIRED
0244  0000    BINPCH,0000
0245  7200      CLA
0246  1217      TAD NUM
0247  7110      CLL RAR
0250  7130      STL RAR
0251  7012      RTR
0252  7012      RTR
0253  7010      RAR
0254  6412      6412    /SKIP IF MARKER FLAG=1
0255  5260      JMP DELAY1
0256  1313      TAD PIP
0257  5262      JMP PUNCH1
0260  7000    DELAY1,NOP
0261  7000      NOP
0262  6041    PUNCH1,TSF
0263  5262      JMP.-1
0264  6046      TLS
0265  4314      JMS WAIT
0266  7200      CLA
0267  1217      TAD NUM
0270  7006      RTL
0271  7006      RTL
0272  7004      RAL
0273  7130      STL RAR
0274  7110      CLL RAR
0275  7110      CLL RAR
0276  7012      RTR
0277  7012      RTR
0300  6412      6412
0301  5304      JMP DELAY2
0302  1313      TAD PIP
0303  5306      JMP PUNCH2
0304  7000    DELAY2,NOP
0305  7000      NOP
0306  6041    PUNCH2,TSF
0307  5306      JMP.-1
0310  6046      TLS
0311  4314      JMS WAIT
0312  5644      JMP I BINPCH
0313  0200    PIP,200
                PAUSE
```

```
                /SUBROUTINE  WAIT
                /PRODUCES A TIME DELAY OF
                /APPROX. 100MILLISEC.
0314  0000    WAIT,0000
0315  7200      CLA
0316  2327      ISZ INR
0317  5316      JMP.-1
0320  1330      TAD INRA
0321  3327      DCA INR
0322  2331      ISZ OUTR
0323  5316      JMP.-5
0324  1332      TAD OUTRA
0325  3331      DCA OUTR
0326  5714      JMP I WAIT
0327  4313    INR,-3465
0330  4313    INRA,-3465
0331  7763    OUTR,-15
0332  7763    OUTRA,-15
                PAUSE
                /SUBROUTINE  EOR
                /PUNCHES END-OF-RECORD MARK (37 OCTAL)
                /FOR USE WITH THE IBM360-44
0333  0000    EOR,0000
0334  7200      CLA
0335  1342      TAD EORMK
0336  6041      TSF
0337  5336      JMP.-1
0340  6046      TLS
0341  5733      JMP I EOR
0342  0037    EORMK,37
                PAUSE
```

SYMBOL TABLE

ADCVT	0235
BINPCH	0244
CONTIN	0205
CTR	0233
CTRA	0234
DELAY1	0260
DELAY2	0304
EOR	0333
EORMK	0342
FREE	0223
INR	0327
INRA	0330
LDR	0221
MKPOS	0220
NUM	0217
OUTR	0331
OUTRA	0332
PIP	0313
PUNCH1	0262
PUNCH2	0306
START	0201
WAIT	0314

Subroutine EOR punches a character that the 360/44 tape reader recognises as signifying the end of a run.

A.2 Photon-Count

The photon-count program makes use of the PDP-8 program interrupt facility. In this mode of operation information arriving at the computer interrupts the main program and is then processed via the program interrupt subroutine. The object of the program is to count photomultiplier pulses for a given time and then punch the total on paper tape together with wavelength information. The total count is also produced as an analogue signal for chart recording purposes.

The main program is defined in the first flow diagram of Fig. A.2. Many of the subroutines are similar to those in "digitise" and will not be discussed further. Subroutine DSPLY provides the photon-count analogue signal via a digital-to-analogue converter. The DSPLY subroutine is used frequently so that the comparitively long time constant of the chart recorder makes the displayed signal seem continuous.

The program interrupt subroutine is outlined in the second flow diagram of Fig. A.2. Each interrupt

Fig. A.2. Flow diagrams and listing of the PHOTON-COUNT computer program.

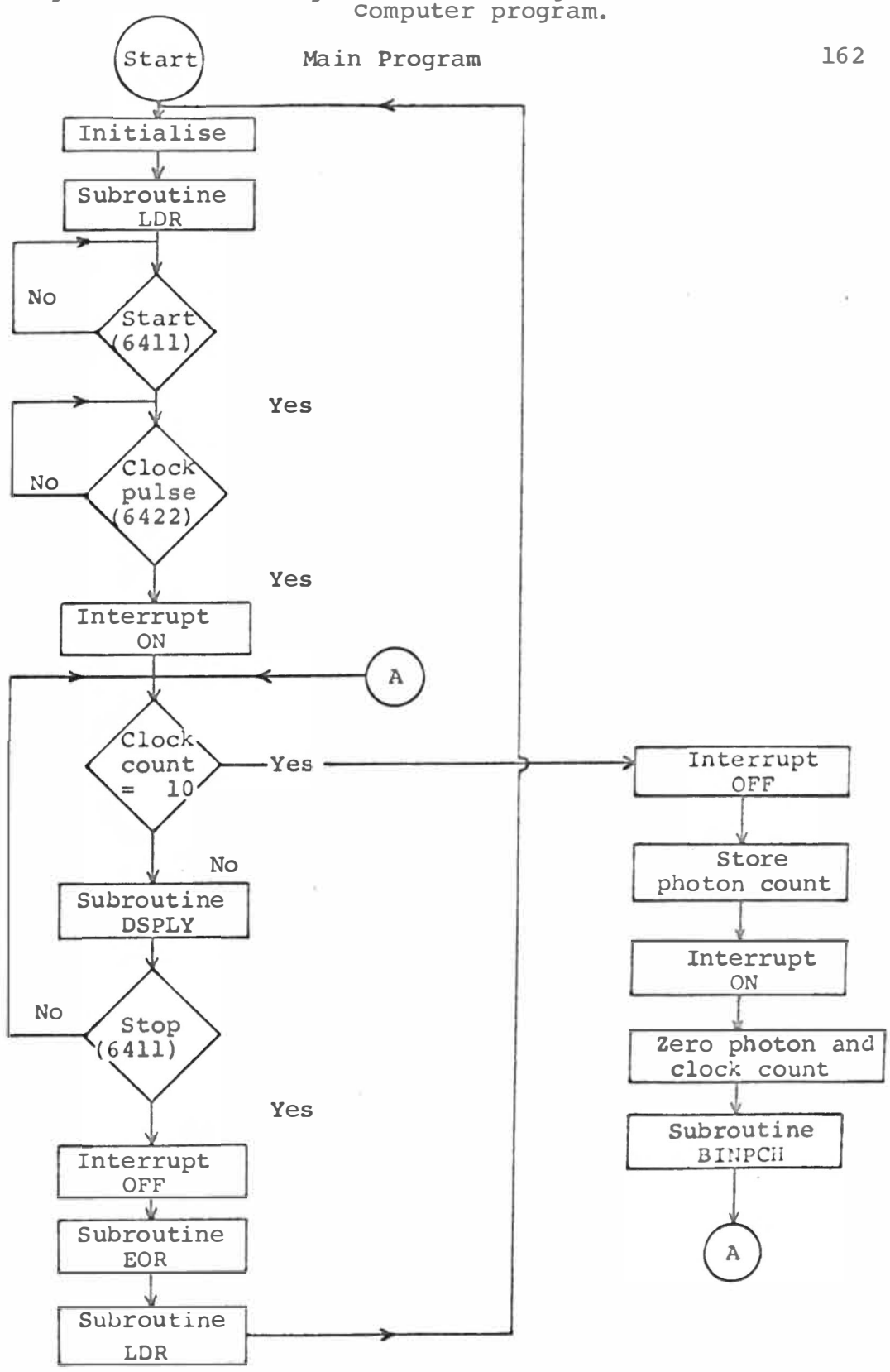

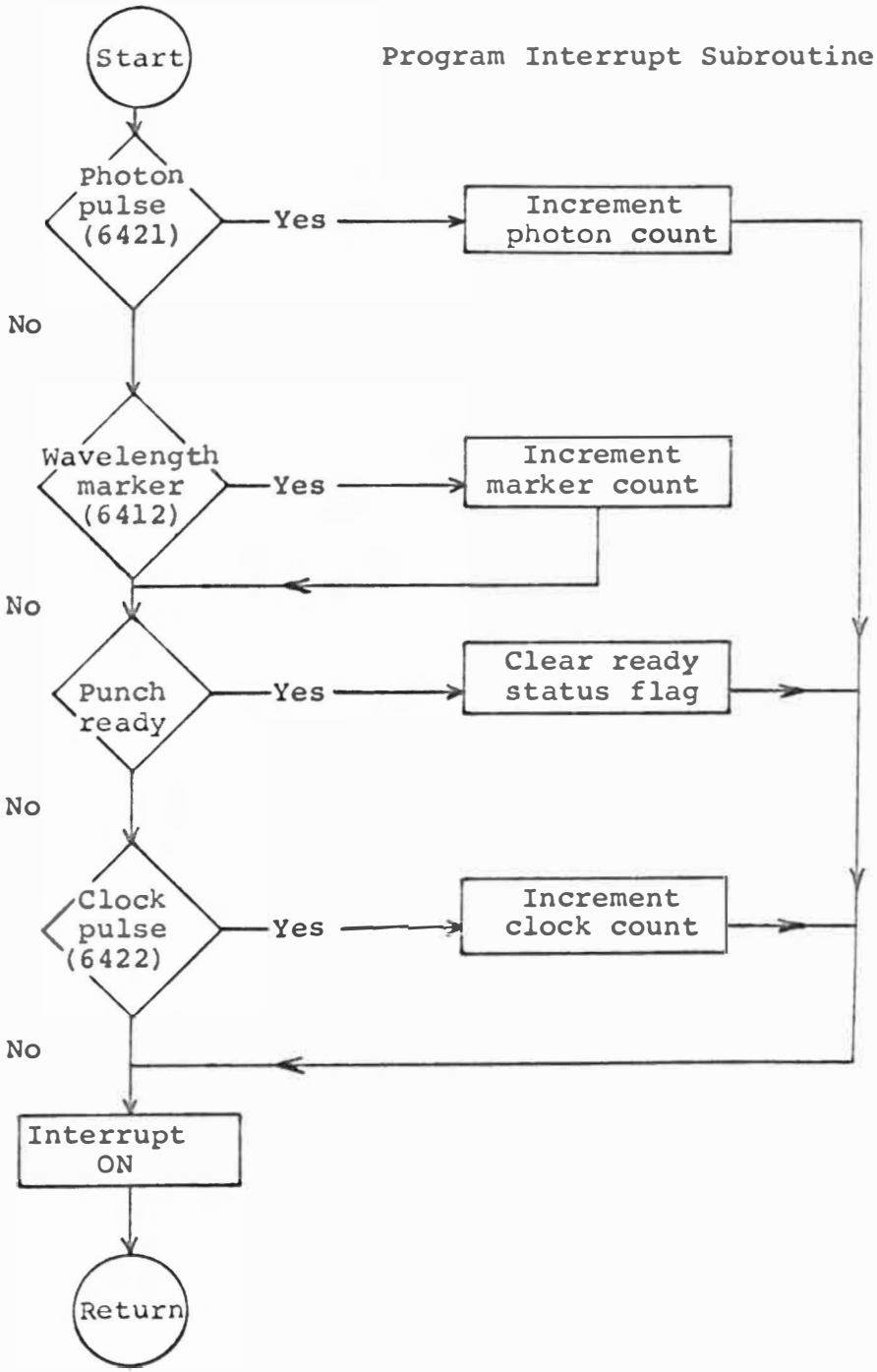
Program Interrupt Subroutine
Start
Photon pulse (6421)
Yes
Increment photon count
No
Wavelength marker (6412)
Yes
Increment marker count
No
Punch ready
Yes
Clear ready status flag
No
Clock pulse (6422)
Yes
Increment clock count
No
Interrupt ON
Return

```
                    /MAIN PROGAM PHOTON COUNT
                    *200
0200  6044            TPC
0201  6061            DCY
0202  6077            DSB
0203  7300      START,CLA CLL
0204  3642            DCA I PHCT
0205  4244            JMS LDR
0206  6411            6411    /SKIP ON START FLAG
0207  5206            JMP.-1
0210  6422            6422    /SKIP ON CLOCK PULSE
0211  5210            JMP.-1
0212  6001            ION
0213  3640            DCA I CLOCK
0214  1640      CONTIN,TAD I CLOCK
0215  1241            TAD CLOCLT
0216  7440            SZA
0217  5230            JMP.+9
0220  6002            IOF
0221  1642            TAD I PHCT
0222  3243            DCA PHCTA
0223  6001            ION
0224  3642            DCA I PHCT
0225  3640            DCA I CLOCK
0226  4260            JMS BINPCH
0227  5214            JMP CONTIN
0230  4347            JMS DSPLY
0231  6411            6411    /SKIP ON START FLAG
0232  7410            SKP
0233  5214            JMP CONTIN
0234  6002            IOF
0235  4356            JMS EOR
0236  4244            JMS LDR
0237  5203            JMP START
0240  0116      CLOCK,CLOCKI
0241  7766      CLOCLT,-12
0242  0115      PHCT,PHCTI
0243  0000      PHCTA,0
                    NUM=PHCTA
                    DCY=6061
                    DSB=6077    /DISPLAY BRIGHTNESS MAX.
                    PAUSE
                    /SUBROUTINE  LDR
                    /PUNCHES BLANK LEADER FOR IBM360-44
0244  0000      LDR,0000
0245  7200            CLA
0246  6041      FREE,TSF
0247  5246            JMP.-1
0250  6046            TLS
0251  2256            ISZ CTR
0252  5246            JMP FREE
0253  1257            TAD CTRA
0254  3256            DCA CTR
0255  5644            JMP I LDR
0256  7704      CTR,-74
0257  7704      CTRA,-74
                    PAUSE
                    /SUBROUTINE  BINPCH
                    /PUNCHES 12-BIT BINARY NUMBERS
                    /6 BITS AT A TIME
                    /A WAVELENGTH MARKER BIT IS PUNCHED
                    /WHEN REQUIRED
0260  0000      BINPCH,0000
0261  7200            CLA
0262  1243            TAD NUM
0263  7110            CLL RAR
0264  7130            STL RAR
0265  7012            RTR
0266  7012            RTR
0267  3323            DCA STORE
0270   724            TAD I PIPMK
0271  7650            SNA CLA
0272  5275            JMP PUNCH1
0273  3724            DCA I PIPMK
0274  1325            TAD PIP1
0275  1323      PUNCH1,TAD STORE
0276  6046            TLS
0277  4327            JMS WAIT
0300  7200            CLA
0301  1243            TAD NUM
0302  7006            RTL
0303  7006            RTL
0304  7006            RTL
0305  7130            STL RAR
0306  7110            CLL RAR
0307  7012            RTR
0310  7012            RTR
0311  3323            DCA STORE
```

```
0312  1724    TAD I PIPMK
0313  7650    SNA CLA
0314  5317    JMP PUNCH2
0315  3724    DCA I PIPMK
0316  1326    TAD PIP2
0317  1323  PUNCH2,TAD STORE
0320  6046    TLS
0321  4327    JMS WAIT
0322  5660    JMP I BINPCH
0323  0000  STORE,0
0324  0117  PIPMK,PIPMKI
0325  0100  PIP1,100
0326  0200  PIP2,200
            PAUSE
            /SUBROUTINE WAIT
            /PRODUCES A DELAY OF
            /APPROXIMATELY 0.1 SEC
            /INCLUDES DSPLY
0327  0000  WAIT,0
0330  7200    CLA
0331  4347    JMS DSPLY
0332  2343    ISZ INR
0333  5331    JMP.-2
0334  1344    TAD INRA
0335  3343    DCA INR
0336  2345    ISZ OUTR
0337  5331    JMP.-6
0340  1346    TAD OUTRA
0341  3345    DCA OUTR
0342  5727    JMP I WAIT
0343  6744  INR,-1034
0344  6744  INRA,-1034
0345  7766  OUTR,-12
0346  7766  OUTRA,-12
            PAUSE
            /SUBROUTINE DSPLY
            /DISPLAYS PHCT VIA THE DAC
0347  0000  DSPLY,0
0350  7200    CLA
0351  1243    TAD PHCTA
0352  7012    RTR
0353  6057    DXS
0354  7200    CLA
0355  5747    JMP I DSPLY
            DXS=6057
            PAUSE
```

SYMBOL TABLE

```
BINPCH  0260
CLOCK   0240
CLOCKI  0116
CLOCLT  0241
CONTIN  0214
CTR     0256
CTRA    0257
DCY     6061
DSB     6077
DSPLY   0347
DXS     6057
EOR     0356
EORMK   0363
FREE    0246
INR     0343
INRA    0344
LDR     0244
NUM     0243
OUTR    0345
OUTRA   0346
PHCT    0242
PHCTA   0243
PHCTI   0115
PIPMK   0324
PIPMKI  0117
PIP1    0325
PIP2    0326
PISUB   0100
PUNCH1  0275
PUNCH2  0317
START   0203
STORE   0323
WAIT    0327
```

```
                    /SUBROUTINE  EOR
                    /PUNCHES END-OF-RECORD MARK (77 OCTAL)
                    /FOR USE WITH THE IBM360-44
0356  0000  EOR,0000
0357  7200    CLA
0360  1363    TAD EORMK
0361  6046    TLS
0362  5756    JMP I EOR
0363  0077  EORMK,77
              PAUSE
                    /"PHOTON COUNT" PROGRAM INTERRUPT SUBROUTINE
                    /VERSION 2
                    /15.0 MICROSEC PHCT CYCLE TIME
                    *1
0001  6421    6421   /SKIP ON PHOTON COUNT
0002  5100    JMP PISUB
0003  2115    ISZ PHCTI
0004  7000    NOP
0005  6001    ION
0006  5400    JMP I 0
                    *100
0100  6412  PISUB,6412   /SKIP ON W/L MARKER PULSE
0101  7410    SKP
0102  2117    ISZ PIPMKI
0103  6041    TSF
0104  5110    JMP.+4
0105  6042    TCF
0106  6001    ION
0107  5400    JMP I 0
0110  6422    6422   /SKIP ON CLOCK PULSE
0111  7410    SKP
0112  2116    ISZ CLOCKI
0113  6001    ION
0114  5400    JMP I 0
0115  0000  PHCTI,0
0116  0000  CLOCKI,0
0117  0000  PIPMKI,0
              PAUSE
```

device is tested sequentially and, depending on its state, appropriate action is taken. In order to shorten the program interrupt cycle time some short cuts are made. Photon pulses occur most frequently and thus are tested first, while the clock pulses are tested last. This arrangement ensures that no clock pulses are missed and gives the lowest possible photon-count dead time.

A.3 Signal-Average

In the signal-average mode of operation data is fed into the computer via the data break facility. A data break occurs independently of the computer program in operation, and needs no program control. Data break only operates while the computer is running. The signal-average program (see Fig. A.3) generates an oscilloscope display from the data fed into the computer, and controls the duration of the run via the remote start-stop switch. At the end of the run the computer halts. When restarted, the data accumulated in the 512 channels is punched on tape by means of subroutine DATPCH.

The data break initial-address switch should be set at 4000_8 to agree with the data storage area used in the program.

Fig. A.3. Flow diagram and listing of the SIGNAL-AVERAGE computer program.

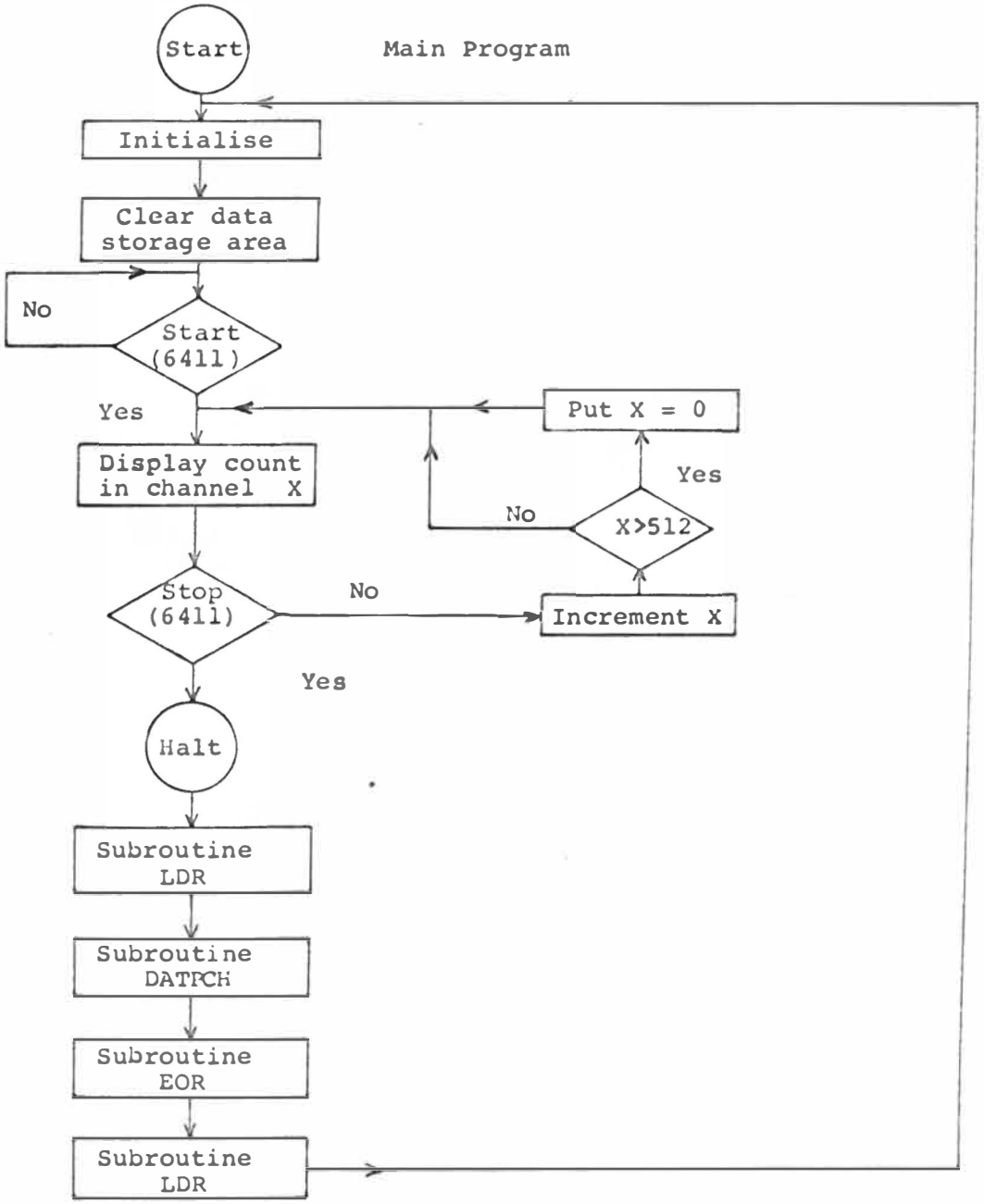

```
                    /MAIN PROGRAM SIGNAL AVERAGE
                    /USES DATA BREAK
                    *200
0200    6077          DSB
                    DSB=6077    /DISPLAY BRIGHTNESS MAX.
0201    7300        START, CLA CLL
0202    3250          DCA X
0203    1245          TAD FIRSTY
0204    3246          DCA Y
0205    3646        CLEAR, DCA I Y
0206    2246          ISZ Y
0207    1246          TAD Y
0210    1247          TAD MMAXY
0211    7640          SZA CLA
0212    5205          JMP CLEAR
0213    6411          6411    /SKIP ON START FLAG
0214    5213          JMP.-1
0215    1250        BEGIN, TAD X
0216    6053          DXL
0217    1245          TAD FIRSTY
0220    3246          DCA Y
0221    1646          TAD I Y
0222    7012          RTR
0223    6067          DYS
0224    7200          CLA
0225    6411          6411    /SKIP ON START FLAG
0226    5236          JMP STOP
0227    2250          ISZ X
0230    1250          TAD X
0231    1251          TAD MXMAX
0232    7640          SZA CLA
0233    5215          JMP BEGIN
0234    3250          DCA X
0235    5215          JMP BEGIN
0236    7402        STOP, HLT    /TURN TELETYPE ON, PRESS "CONT"
0237    6044          TPC
0240    4252          JMS LDR
0241    4266          JMS DATPCH
0242    4335          JMS EOR
0243    4252          JMS LDR
0244    5201          JMP START
0245    4000        FIRSTY, 4000
0246    0000        Y, 0
0247    2000        MMAXY, -6000
0250    0000        X, 0
0251    7000        MXMAX, -1000
                    DXL=6053
                    DYS=6067
                    PAUSE
```

```
                /SUBROUTINE  LDR
                /PUNCHES BLANK LEADER FOR IBM360-44
0252  0000      LDR,0000
0253  7200        CLA
0254  6041      FREE,TSF
0255  5254        JMP.-1
0256  6046        TLS
0257  2264        ISZ CTR
0260  5254        JMP FREE
0261  1265        TAD CTRA
0262  3264        DCA CTR
0263  5652        JMP I LDR
0264  7704      CTR,-74
0265  7704      CTRA,-74
                  PAUSE
                /SUBROUTINE DATPCH
                /PUNCHES STORED DATA
0266  0000      DATPCH,0
0267  7200        CLA
0270  1245        TAD FIRSTY
0271  3246        DCA Y
0272  1646      AGAIN,TAD I Y
0273  3303        DCA NUM
0274  4305        JMS BINPCH
0275  2246        ISZ Y
0276  1246        TAD Y
0277  1304        TAD MMAXYA
0300  7640        SZA CLA
0301  5272        JMP AGAIN
0302  5666        JMP I DATPCH
0303  0000      NUM,0
0304  3000      MMAXYA,-5000
                PAUSE
                /SUBROUTINE  BINPCH
                /PUNCHES 12-BIT BINARY NUMBERS
                /6 BITS AT A TIME
0305  0000      BINPCH,0000
0306  7200        CLA
0307  1303        TAD NUM
0310  7110        CLL RAR
0311  7130        STL RAR
0312  7012        RTR
0313  7012        RTR
0314  6041        TSF
0315  5314        JMP.-1
0316  6046        TLS
0317  7200        CLA
0320  1303        TAD NUM
0321  7006        RTL
0322  7006        RTL
0323  7006        RTL
0324  7130        STL RAR
0325  7110        CLL RAR
0326  7012        RTR
0327  7012        RTR
0330  6041        TSF
0331  5330        JMP.-1
0332  6046        TLS
0333  7200        CLA
0334  5705        JMP I BINPCH
                PAUSE
                /SUBROUTINE  EOR
                /PUNCHES END-OF-RECORD MARK (77 OCTAL)
                /FOR USE WITH THE IBM360-44
0335  0000      EOR,0000
0336  7200        CLA
0337  1344        TAD EORMK
0340  6041        TSF
0341  5340        JMP.-1
0342  6046        TLS
0343  5735        JMP I EOR
0344  0077      EORMK,77
                  PAUSE

   SYMBOL TABLE
AGAIN   0272
BEGIN   0215
BINPCH  0305
CLEAR   0205
CTR     0264
CTRA    0265
DATPCH  0266
DSB     6077
DXL     6053
DYS     6067
EOR     0335
EORMK   0344
FIRSTY  0245
FREE    0254
LDR     0252
MMAXY   0247
MMAXYA  0304
MXMAX   0251
NUM     0303
START   0201
STOP    0236
X       0250
Y       0246
```